A VLBI investigation of the discrepant image flux-density ratio in the gravitational lens JVAS B0218+357

Dissertation

zur

Erlangung des Doktorgrades (Dr. rer. nat.)

der

Mathematisch-Naturwissenschaftlichen Fakultät

der

Rheinischen Friedrich-Wilhelms-Universität Bonn

vorgelegt von

Rupal Mittal

aus

New Delhi (India)

Bonn, 2006

Angefertigt mit Genehmigung der Mathematisch-Naturwissenschaftlichen Fakultät der Rheinischen Friedrich-Wilhelms-Universität Bonn

1. Referent: Prof. Dr. Peter Schneider
2. Referent: Priv. Doz. Dr. Walter Huchtmeier

Tag der Promotion: 27.04.2006

Contents

Introduction

This thesis is a combination of observational radio-astronomy and strong gravitational lensing. The work encompassed the reduction of VLBI (Very Long Baseline Interferometry) phase-reference and multi-frequency data of the double-image gravitational lens JVAS B0218+357. At later stages, the study was pursued by lensing-related analysis to explore the causes of the well-known anomaly associated with this lens system. This anomaly is manifested in the frequency-dependent image flux-density ratio, which violates the achromatic nature of the phenomenon of gravitational lensing. The lensed (background) object is a powerful radio source, which belongs to a class of objects known as Active Galactic Nuclei (AGN) with a standard jet-core morphology, and whose structure changes with radio-frequency.

Gravitational lensing is a powerful and unbiased astrophysical tool for studying both dark and luminous mass distributions at intermediate and high redshifts over intragalactic and galactic scales, clusters of galaxies and large-scale structures. It plays the role of a natural cosmic lens and enables the study of the lensed background object and the lens environment in great detail. Observations of continuum background emission of extended radio-sources, such as B0218+357, provide useful information on the radial distribution of the mass of the deflector and yield independent results on the kinematics, spatial structure and the elemental abundance in the lens galaxies. The basic theory of gravitational lensing is given in chapter 1.

The radio structure of the lens system B0218+357 consists of two compact images, A and B, with the smallest angular separation amongst all known galaxy lenses, and an additional faint Einstein ring of a similar diameter. The lens galaxy is a low-mass late-type spiral. The background AGN has an almost featureless optical spectrum, based on which it is conjectured to be a blazar. It is variable in its emission and an accurate value for the time delay between variations in the images has been measured. The wealth of data coming from numerous radio and optical observations of this system at various frequencies and epochs provides constraints for lens models, which together with the time delay, give the possibility to determine the Hubble constant H_0. The best-fitting lens model derived from the LensClean algorithm is a singular isothermal elliptical potential (SIEP), which is the standard choice of model used in this thesis (or a slightly varied form of it, which includes non-isothermality with a 5 % deviation). Chapter 2 is devoted to B0218+357, which covers the facts known about this system prior to commencing this work.

Most of the lensing characteristics of B0218+357 are well-reproduced by the above lens-model, but there are a few complications. One of them is a steady and systematic decline in the ratio of radio flux-density of image A to image B with decreasing frequency. This observation is not in compliance with the fact that the effect of gravitational lensing is non-dispersive. The change in the ratio with frequency is much greater than the error introduced in a single epoch measurement due to the combined effects of the source variability and the time delay between the images. Understanding this discrepancy is the motivation behind this research project. Several mechanisms are studied to account for this unexpected behaviour, both of gravitational type as well as of non-gravitational type.

Although gravitational lensing of a point source is achromatic, the issue needs attention

for extended sources with a frequency-dependent structure that extends over regions of different relative image-magnifications. One of the primary tasks of this work was to investigate whether frequency-dependent source centroid-positions, combined with a magnification gradient across the image plane, could give rise to the frequency dependence of the relative image-magnification. For this, multi-frequency VLBI observations were made in January 2002 using the Very Large Baseline Array (VLBA) and the Effelsberg radio telescope. Unambiguous registration of the structures of the radio images at different frequencies is performed using the technique of "inverse" phase-referencing. Chapter 3 is an introduction to the techniques of VLBI and phase-referencing. It forms a purview to the data-reduction of the B0218+357 dataset and the phase-referencing analysis, which is described in chapter 4. The results of this chapter are published in Mittal et al. (2006).

The foregoing analysis assumes that the relative magnification at the image centroid-positions, derived from a optimal lens model, gives a good measure of the expected image flux-density ratio of an extended object. However, this is only an approximation, which for complicated source structures involving steep magnification gradients in the image plane, is not valid. A detailed evaluation of the magnification weighted flux-densities integrated over the image areas and the image magnifications ratios are described in chapter 5.

There are numerous galaxy-scale gravitational lens systems with inconsistent image flux ratios. Intermediate-mass substructures along the line-of-sight to the lensed images in the form of galactic satellites can lead the image magnifications to deviate from values dictated by simple macro-lensmodels. Such substructures are predicted by cold dark matter simulations of galaxy formation for a ΛCDM universe. The number of such substructures are over-predicted by almost an order of magnitude to what is observed around the Milky Way Galaxy. The anomalous flux ratios in galaxy scale lens systems are thought to be the first direct evidence of such small-scale power. In the case where the source structure changes with frequency, the effects of substructure on the image-magnifications and the centroid-position of the image brightness distributions will be frequency-dependent, and can be identified with the help of multi-frequency high-resolution observations. Chapter 6 addresses the issue of substructure, which is the current-most accepted solution for the general problem of flux ratio anomalies described above, and whether this could also explain the anomaly seen in B0218+357.

Other suspected mechanisms, which are non-gravitational in nature, are discussed as a function of frequency in chapter 7. First, the process of free-free absorption, which affects the spectra of the lensed images. This process has been observed in other lens systems where the line-of-sight to one (or more) of the lensed images passes through the central regions of the galaxies where the electron column densities are large. The flux density affected by free-free absorption shows a sharp decline over a small frequency range, from 1 GHz to 5 GHz, and can be clearly identified. Second, many gravitationally lensed images are thought to be affected by spatial and temporal scintillations and scatter-broadening due to small-scale inhomogeneities in the ionized component of the interstellar matter. Once again, this propagation effect is frequency dependent. Therefore, multi-frequency observations of B0218+357 are used to test whether either of the above two mechanisms are likely to provide a possible explanation for the flux ratio anomaly in this lens system.

This thesis ends with a synopsis of the work accomplished in this doctoral project. Several astrophysical tools and processes have been used throughout this thesis, which to avoid confusion and maintain clarity in the text of the main chapters, are covered in the appendices.

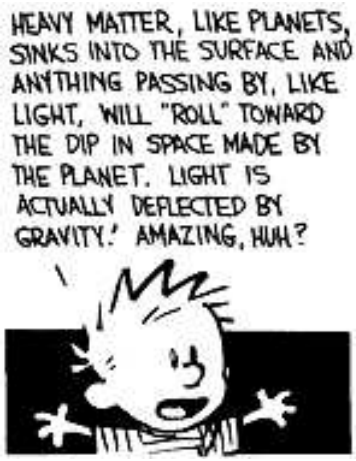

1 Gravitational Lensing

Newton's Query 1 (Opticks, 1704): "Do not Bodies act upon Light at a distance, and by their action bend its Rays, and is not this action (caeteris paribus) strongest at the least distance?"

The 'seed' idea that light could be acted upon by gravity dates back to the early eighteenth century, in the form of the first of a series of 'Queries' that appeared in the book, *Opticks*, 1704 by I. Newton, quoted above. The idea was pursued by J. Michell (1783) and P. Laplace (1796) independently, who showed that light has a finite speed and, hence, is affected by gravity just as much as anything else. Their work led them to conjecture for the first time a hypothetical object similar to what today would be called a black hole. Following the same seed idea, the stage for the phenomenon of gravitational lensing was set by a string of independent events. In 1784, the British scientist H. Cavendish derived the Newtonian-formula for the deflection angle for light as it passes a point-mass, $2GM/(c^2d)$, where M is the mass of the gravitating body, d is the impact parameter of the light ray, G is the gravitational constant, and c is the velocity of light. The same result was separately derived by J. G. Soldner (1801). A century later, using the theory of General Relativity (GR), Einstein (1915) established a more accurate derivation for the deflection angle for light. The result of his calculations predicted a value twice the Newtonian one, the additional term arising due to the curvature in the spatial metric. His result was confirmed to within 20 % to 30 % during the solar eclipse in 1919 by Dyson et al. (1920), whereby they measured the apparent angular shifts in the position of the stars close to the limb of the sun. The deflection of light rays due to gravitational fields of massive objects came to be known as gravitational lensing (GL).

An important aspect of the GL effect put forward by Eddington (1920) was the possibility of producing multiple images of a single background source for special source-lens alignments. In subsequent years, Chwolson (1924), Einstein (1936) and Russell (1937) investigated the

probability of detecting gravitational lens effects due to stars as perturbers and discarded it as being vanishingly small. But it was soon pointed out by Zwicky (1937a,b) that if the stellar masses were replaced with *extragalactic nebulae* of masses $\sim 10^{11}\ M_{\odot}$ as in the Coma and Virgo galaxy clusters, the probability of detection becomes non-negligible. Zwicky went further to express the study of gravitational lenses as especially important in providing a test-bed for GR, facilitating viewing of objects that are at great distances from us, and lastly, a better and more direct mass-estimation of these *extragalactic nebulae*.

One of the most revolutionary consequences of GL was stated by Refsdal (1964), wherein the potential to determine the Hubble constant, H_0 was demonstrated. This requires a background source of varying emission lensed into two or more images. Due to different light propagating times through different parts of the lens (see Sect. 1.1.3), a time-delay, τ, is introduced between the variation in the images. Using τ, the redshifts of the lensed source and the lens, and a model for the lens-mass distribution, the value of H_0 can be estimated. This speculation was made about the same time as the discovery of the first quasar 3C 273 by Schmidt (1963). Quasars are high-redshift objects with a point-like appearance in the optical. Therefore, the probability of their getting lensed by the intervening structures is high. Furthermore, owing to their compact sizes the prospect of identifying well-resolved images of such an object was soon realized to be very promising. The first lensed object discovered by Walsh et al. (1979) was, indeed, a quasar with two images separated by ~ 6 arcsec. Since then, the number of observed GL systems with multiple images has increased to $\gtrsim 100$ [1].

In the following, some aspects of GL are reviewed with the main focus on configurations that result in multiple images.

1.1 Lens-Equation

An important result based on which several properties will be further discussed, is the lens equation. Shown in Fig. 1.2 is an intervening mass-distribution, the lens (L), which deflects the light ray coming from the background source (S) (in the source plane) to the observer (O). The extent of the region within which most deflection occurs is typically much smaller than the distances of extragalactic lenses (the latter being on the order of several hundreds of Megaparsecs to Gigaparsecs). Therefore, the thin-lens approximation can be used wherein the matter distribution is viewed as a thin plane (hereafter the lens plane). By simple geometry

$$\beta = \theta - \hat{\alpha}\frac{D_{\rm ls}}{D_{\rm s}}\ , \tag{1.1}$$

where β is the angular position of the source in the absence of the lens, θ is the observed angular position of the image and $\hat{\alpha}$ is the angle through which the incoming light ray is deflected. $D_{\rm l}$, $D_{\rm s}$ and $D_{\rm ls}$ are the distances to the lens, the source and between the lens and the source, respectively. Eq. 1.1 is the lens equation in one dimension. This form of the lens equation is valid only if the distances applied are the angular diameter distances (see Appendix A.4). The relation between the observed angular sizes and physical distances depends on the cosmological parameters of the universe. The basic equations, which are essential for the understanding of cosmology, and the details of the ΛCDM flat-universe cosmological model, which is used throughout this thesis are given in Appendix A.

[1] see Treu et al. (2006) and the CASTLES website, http://cfa-www.harvard.edu/castles/, C.S. Kochanek, E.E. Falco, C. Impey, J. Lehar, B. McLeod, H.-W. Rix

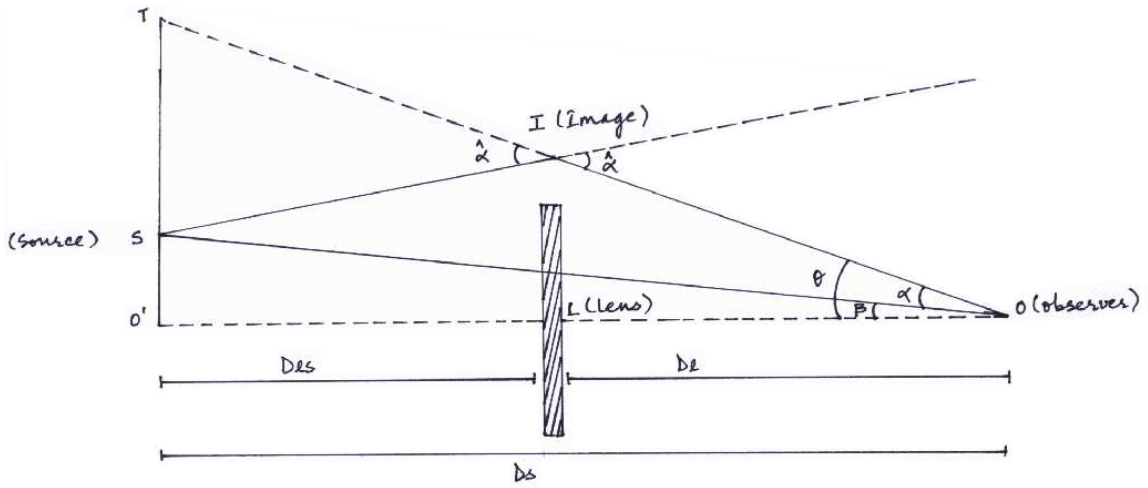

Figure 1.2: The light ray from the source (S) gets deflected by the lens (L) and gets deviated to the observer (O). The light ray suffers a deviation of $\hat{\alpha}$ at the lens plane. The angular diameter distances from the observer to the source, from the observer to the lens, and from the lens to the source are $D_{\rm s}$, $D_{\rm l}$ and $D_{\rm ls}$ respectively.

1.1.1 Deflection angle

The effect of a gravitational field of force on a particle, under two assumptions, can be described by adding a perturbation term to the Minkowski metric, the latter representing a locally-flat space-time (Adler et al. 1965; Weinberg 1972). This perturbation term is related to the Newtonian potential of the lens, $\phi = GM/R$ and is $= 2\phi/c^2$. The assumptions are:

1. The velocity of the lens, v, is much smaller than c. The typical peculiar velocities of galaxies and clusters of galaxies is about a few hundreds to thousand km sec^{-1}.

2. $\phi \ll c^2$, which is a reasonable assumption as galaxies are characterized by mass and size on the order of 10^{11} $M_\odot$ and 20 kpc, respectively. For clusters of galaxies, the mass is proportionately scaled by a factor about 100 to 1000 and size by a factor of 10 to 100. This assumption is also valid for compact objects such as black holes or neutron stars provided that $R \gg 2GM/c^2 = R_{\rm S}$, where $R_{\rm S}$ is the Schwarzschild radius.

The deflection angle, $\hat{\alpha}$, is calculated by integrating the potential gradient perpendicular to the light path along the distance, Δz, within which most of the deflection occurs

$$\vec{\hat{\alpha}} \;=\; \frac{2}{c^2}\int \vec{\nabla}_\perp \phi(d,z)\; dz \;,$$

where d is the impact parameter. Using the above result, the deflection angle for a point mass is found to be $4GM/c^2d$ (twice the value derived by Cavendish).

The thin-lens approximation allows the lens mass distribution to be projected onto the lens plane perpendicular to the line-of-sight. Let $\vec{\xi}$ be the two dimensional coordinate point where a ray of light pierces the lens plane. Then the deflection angle can be conveniently described

in terms of the surface-mass density, Σ, defined as

$$\Sigma(\vec{\xi}) \;=\; \int \rho(\vec{\xi}, z)\, dz \;, \tag{1.2}$$

and

$$\vec{\hat{\alpha}}(\vec{\xi}) \;=\; \frac{4G}{c^2} \int \frac{(\vec{\xi} - \vec{\xi'})\, \Sigma(\vec{\xi'})}{|\vec{\xi} - \vec{\xi'}|^2}\, d^2\xi'. \tag{1.3}$$

In the above, the deflection angle is the sum of the deflections produced by the infinitesimal mass elements constituting the lens plane. For a circular symmetric lens with a constant surface-mass density, the deflection angle is reduced to

$$\vec{\hat{\alpha}} \;=\; \frac{\Sigma}{\Sigma_{\rm cr}} \frac{D_{\rm s}}{D_{\rm ls}}\, \vec{\theta}\,, \tag{1.4}$$

where $\vec{\xi} = D_{\rm l}\vec{\theta}$ and $\Sigma_{\rm cr}$ is the critical surface-mass density and a function of angular diameter distances only,

$$\Sigma_{\rm cr} \;=\; \frac{c^2}{4\pi G} \frac{D_{\rm s}}{D_{\rm l} D_{\rm ls}}. \tag{1.5}$$

1.1.2 Einstein radius

The deflection angle for a circularly symmetric mass distribution is reduced to one dimensional and is given by

$$\hat{\alpha} \;=\; \frac{4GM(\xi)}{c^2 \xi},$$

where $M(\xi)$ is the mass enclosed within a radius ξ. Substituting the above value for the deflection angle, the lens equation becomes

$$\beta \;=\; \theta - \frac{4GM(\xi)}{c^2\theta} \frac{D_{\rm ls}}{D_{\rm s} D_{\rm l}}.$$

If the source is directly behind the lens on the optical axis (with respect to the observer), the light from the source gets imaged into a ring called the Einstein ring. Setting $\beta = 0$, the angular radius of the Einstein ring can be evaluated

$$\theta_E \;=\; \left[\frac{4GM(\theta_E)}{c^2} \frac{D_{\rm ls}}{D_{\rm s} D_{\rm l}} \right]^{\frac{1}{2}}. \tag{1.6}$$

The Einstein radius is an important length-scale in GL and its observation in a lens system provides information on the amount of mass that is encompassed within it. Moreover, by comparing Eqs. 1.5 and 1.6, it is evident that the mean surface-mass density within a radius of $D_{\rm l}\theta_E$ is exactly the critical surface-mass density. It is also a rough measure of the separation between multiple images in the case where the source in not directly behind the lens but within or close to the Einstein radius.

1.1.3 Time-Delay

The light ray deviated by the lens takes a longer time to reach the observer than in the absence of the lens. The time-delay comprises two terms. The first arises due to the increased path length that the light ray traverses due to the diversion. The other is due to the potential drag inflicted upon the photon that causes it to "slow" down, also called the Shapiro delay. In the theory of refraction, the velocity of light in a medium other than vacuum is c/n, where $n > 1$ is the refractive index. Similarly, the effective speed of the light ray is reduced as it passes through the lens by an analogous increase in the refractive index, only that it is due to the gravitational field of force instead of electromagnetic. For a detailed analysis of the time-delay derivation, the reader is referred to Schneider et al. (1992). Herein below, only the result is stated

$$\hat{\tau} \;=\; \frac{(1+z_{\rm l})}{c}\left[\frac{D_{\rm l}D_{\rm s}}{2D_{\rm ls}}(\vec{\theta}-\vec{\beta})^2 - \hat{\psi}(\vec{\xi})\right], \tag{1.7}$$

where $z_{\rm l}$ is the lens redshift and $\hat{\psi}(\xi)$ is the deflection potential (with dimensions of distance) defined as

$$\hat{\psi}(\vec{\xi}) \;=\; \frac{4G}{c^2}\int \Sigma(\vec{\xi}')\,\ln\left(\frac{|\vec{\xi}-\vec{\xi}'|}{\xi_0}\right)\,d^2\xi'. \tag{1.8}$$

From Eq. 1.3, the deflection angle is seen to be the gradient of the deflection potential

$$\hat{\vec{\alpha}} = \vec{\nabla}_{\xi}\hat{\psi}. \tag{1.9}$$

1.1.4 Scaled quantities

For the mathematical ease (and better appearance), dimensionless versions of the quantities defined above are given below. With the help of Fig. 1.2, the lens equation can be rewritten as,

$$\frac{\vec{\eta}}{D_{\rm s}} \;=\; \frac{\vec{\xi}}{D_{\rm l}} - \frac{D_{\rm ls}}{D_{\rm s}}\,\hat{\vec{\alpha}},$$

where $\xi = \mathrm{LI}$ and $\eta = \mathrm{O'S}$. Introducing length scales, ξ_0 and η_0, in the lens and the source planes such that

$$\frac{\xi_0}{D_{\rm s}} \;=\; \frac{\eta_0}{D_{\rm l}},$$

the dimensionless vectors on the lens and the source planes can be written as

$$\vec{x} \;=\; \frac{\vec{\xi}}{\xi_0} \quad ; \quad \vec{y} \;=\; \frac{\vec{\eta}}{\eta_0}.$$

The scaled deflection and scaled potential are defined as

$$\vec{\alpha}(\vec{x}) \;=\; \frac{D_{\rm l}D_{\rm ls}}{D_{\rm s}\xi_0}\,\hat{\vec{\alpha}}(\xi_0\vec{x}) \quad ; \quad \psi(\vec{x}) \;=\; \frac{D_{\rm l}D_{\rm ls}}{D_{\rm s}{\xi_0}^2}\,\hat{\psi}(\xi_0\vec{x}). \tag{1.10}$$

From Eqs. 1.9 and 1.10 and noting that $\vec{\nabla}_{\xi} = (1/\xi_0)\vec{\nabla}_x$,

$$\vec{\alpha} \;=\; \vec{\nabla}_x\psi. \tag{1.11}$$

Similarly, the scaled time-delay is

$$\tau \;=\; \frac{c}{(1+z_{\rm l})}\frac{D_{\rm l}D_{\rm ls}}{D_{\rm s}{\xi_0}^2}\,\hat{\tau} \quad ; \quad \tau(\vec{x},\vec{y}) \;=\; \frac{1}{2}(\vec{x}-\vec{y})^2 - \psi(\vec{x})\,, \tag{1.12}$$

so that using the above terminologies and $\vec{\nabla} = \vec{\nabla}_x$, the lens equation can be written in the following varied forms

$$\vec{y} \;=\; \vec{x} - \vec{\alpha}(\vec{x}) \quad ; \quad \vec{0} \;=\; \nabla\left[\frac{1}{2}(\vec{x}-\vec{y})^2 - \psi(\vec{x})\right]. \tag{1.13}$$

Subsequently, the following relation can be drawn between the lens equation and the scaled time-delay function,

$$\nabla\tau(\vec{x},\vec{y}) \;=\; 0. \tag{1.14}$$

Thus, the lens equation is satisfied for $\vec{x}$ and $\vec{y}$ such the gradient of the scaled time-delay function, also known as *Fermat potential*, vanishes. This is another manifestation of Fermat's principle which states that the optical path length must be extremal. Hence, images are formed at the minima, maxima or points of inflection-saddle points, of the Fermat potential.

1.1.5 Magnification

GL is a powerful tool for studying background objects that are either very distant or intrinsically not luminous enough to be easily visible. The reason is that in many cases it resembles a optical glass lens which has a magnifying effect. In other cases, GL leads to the convergence of the light rays resulting in de-magnification of background sources. The magnification, μ, is determined with the Jacobian matrix defined as, $M(\vec{x}) = \partial\vec{y}/\partial\vec{x}$, and is the inverse of its determinant. From Eq. 1.13,

$$M_{ij} \;=\; \tau_{ij} \;=\; \delta_{ij} - \psi_{ij} \;\equiv\; \begin{pmatrix} 1-\kappa-\gamma_1 & -\gamma_2 \\ -\gamma_2 & 1-\kappa+\gamma_1 \end{pmatrix},$$

where

$$\kappa \;=\; \frac{\Sigma}{\Sigma_{\rm cr}} \;=\; \frac{\psi_{11}+\psi_{22}}{2}\,,$$

$$\gamma^2 \;=\; \gamma_1^2+\gamma_2^2 \quad ; \quad \gamma_1 \;=\; \frac{\psi_{11}-\psi_{22}}{2} \quad ; \quad \gamma_2 \;=\; \psi_{12} \;=\; \psi_{21},$$

where ψ_{ij} is the double derivative of the scaled deflection potential with respect to x_i and x_j. κ is the scaled surface-mass density known as convergence and allows symmetric magnification of background objects. γ, on the other hand is responsible for asymmetric distortion, known as shear. It is important to note that the object becomes brighter because of the increased power received from an infinitesimal source element. The intensity or the surface brightness (Sect. B) and the frequency of the light, on the other hand, remain unaltered. Thus it is the increase in flux due to the increase in image area that results in the source amplification. Therefore,

$$\mu \;=\; \frac{I_\nu d\Omega_{\rm I}}{I_\nu d\Omega_{\rm S}} \;=\; |M_{ij}|^{-1} \;=\; \frac{1}{(1-\kappa)^2-\gamma^2}. \tag{1.15}$$

The magnification can either have a positive or a negative value. Negative magnification has the following implication: the handedness of a displacement vector relative to a reference

vector in the source plane, defined as the sign of the cross product of these two vectors, is reversed in the image plane. Such images are said to have inverse or negative parity.

In terms of κ, the scaled potential and the scaled deflection become

$$\psi(\vec{x}) \;=\; \frac{1}{\pi}\int \kappa(x')\,\ln|\vec{x}-\vec{x}'|\;d^2x', \tag{1.16}$$

$$\vec{\alpha}(\vec{x}) \;=\; \frac{1}{\pi}\int \kappa(x')\,\frac{\vec{x}-\vec{x}'}{|\vec{x}-\vec{x}'|^2}\;d^2x'. \tag{1.17}$$

1.2 Image Properties

Based on the mathematical framework developed so far, some general theorems and image properties are given in this section.

Let the number of images that correspond to the minimum or maximum of the time-delay function be designated as $n_{\rm I}$ and $n_{\rm III}$ [det $M > 0$, $\mu \geq 1$] respectively, and saddle points by $n_{\rm II}$ [det $M < 0$, $\mu \leq 0$]. Then the following theorems hold (Schneider et al. 1992):

1. $n_{\rm I} \geq 1$, $n < \infty$, $n_{\rm I} + n_{\rm III} = 1 + n_{\rm II}$.
   These conditions apply assuming that the surface-mass density of a lens declines faster than $1/x^2$ for $x \to \infty$, is smooth and consequently the deflection angle is continuous. Objects with extreme mass concentrations at their centre, such as black holes or stars are excluded from this generalization as they do not fulfill the above assumptions.

2. Images of type II have inverse parity as opposed to images of type I and III which have positive parity. In the double-image lens system B0218+357described in chapter 2, image A has a positive parity and image B has a negative parity.

3. A lens may or may not be strong enough to produce more than one image of a source. A necessary condition to have multiple images is that there exists at least one point $\vec{x}$ such that $\kappa(\vec{x}) > \frac{1}{2}$. A sufficient condition is $\kappa > 1$, which shows the relevance of the critical density $\Sigma_{\rm cr}$.

The first set of conditions embeds the well-known "odd number theorem", which states that the number of images in any gravitational-lens system is odd, with one image which is formed close to the centre of the lens galaxy. However, of all the multiple-image lens systems discovered to-date, there is only lens system where a central image has been observed (Winn et al. 2002), and two others with odd number of images but non-standard lens geometries (Kochanek et al. 2004, Sect. B.2). This interesting observational fact indicates that either the lens potential is singular at the centre or the central surface density is sufficiently high that the centre image is highly de-magnified. In the case of the latter, due to limited sensitivities, the central images are subject to be missed. This can be used to put constraints on the central surface mass density, and consequently, an upper limit to the core-radius defined as the scale within which the potential is shallower than if the core-radius $\to 0$.

1.2.1 Caustics and critical curves

From Eq. 1.15 it is clear that as the denominator $\to 0$, $\mu \to \pm\infty$. The loci of points at which the magnification becomes infinitely high constitute critical curves in the lens plane. The

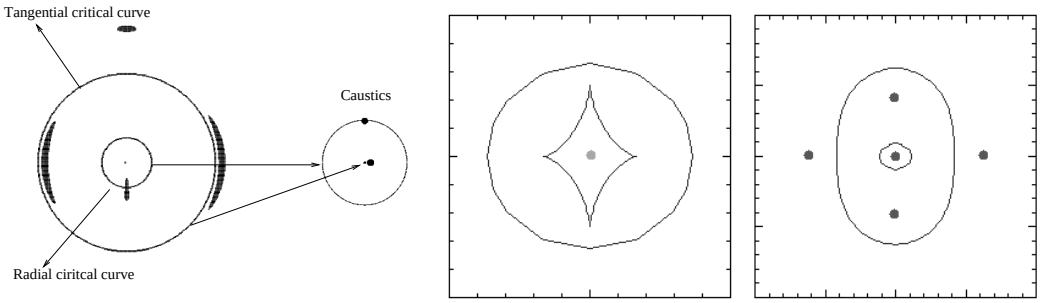

Figure 1.3: (a) Critical curves (left) and caustics (right) produced by a non-singular circularly symmetric lens model. The tangentially stretched images and a faint image at the centre are produced with a source location near the point caustic. A source on the outer caustic gives rise to a radial image on the inner critical curve and a tangential image outside the tangential critical curve (adapted from Narayan & Bartelmann 1999). (b) For non-circular lens models, the inner point caustic (left) converts in to an astroid structure with folds and cusps and the circularity of the critical curves (right) is destroyed.

projected counterparts of the critical curves in the source plane are known as caustics. The number of lensed images, n, changes as a function of the source position, y, relative to the caustics. For $y \gg 1$, there is only one image that appears. As the source approaches the lens and crosses the caustic, there appear two additional images. Consequently the number of images either increases or decreases by two as the source jumps a caustic.

1.2.2 Lens symmetry

For non-singular and circularly symmetric lens models, there are two critical curves about the lens-centre which are circular in shape. The caustic corresponding to the outer critical curve maps onto a degenerate point and the caustic corresponding to the inner critical curve maps onto a circle of a finite size. The images close to the two critical curves have very distinct morphologies. The outer critical curve is characterized by tangentially stretched images close and relative to it, hence called a tangential critical curve. Furthermore, the outer critical curve for a spherically symmetric mass distribution is the same as the Einstein ring. The inner critical curve is radial in nature in that the images close to it are radially aligned relative to it. Fig. 1.3a shows the critical curves in the lens plane and the corresponding caustics in the source plane for a non-singular circularly symmetric lens. For a point source close to the lens centre, there are two tangentially stretched images close to the tangential critical curve and one faint image near the lens centre.

In reality, the mass distributions are expected to have a non-zero degree of angular structure in them. Breaking of the circular symmetry leads to the following qualitative changes:

1. Asymmetry results in the images, the source and the lens centre no longer lying on a straight line.

2. The inner point-like caustic expands into an astroid shaped structure made of cusps and folds. A source-crossing at one of its cusps results in three images either merging into or springing up from one bright image. If a source crosses over a fold, two new bright

images either appear or merge to disappear. The critical curves and the caustics for an asymmetric lens are displayed in Fig. 1.3b.

1.2.3 Relative time-delay

The time-delay equation Eq. 1.7 is a measure of the difference between the times at which the diverted and the undiverted light rays reach the observer. Since the unperturbed light ray is never observed itself, this equation does not have much use in this form. Instead, observations of light arrival times *from different images* of the same source remove the need for any information about the undiverted ray and yield useful estimates of the cosmological parameters. Using Eq. 1.12, the relative time-delay for two images at $\vec{x_1}$ and $\vec{x_2}$ is:

$$\hat{\tau} \;=\; \frac{(1+z_{\rm l})}{c}\,\frac{D_{\rm s}D_{\rm l}}{D_{\rm ls}}\,[\tau(\vec{x_1},\vec{y}) - \tau(\vec{x_2},\vec{y})], \tag{1.18}$$

where the length scale, ξ_0, is chosen to be $D_{\rm l}$. Now, the combination of the angular diameter distances can be expressed in terms of the Hubble constant, H_0, as

$$\frac{(1+z_{\rm l})}{c}\,\frac{D_{\rm s}D_{\rm l}}{D_{\rm ls}} \;\propto\; H_0^{-1}\,. \tag{1.19}$$

Therefore, the present value of the Hubble constant can be estimated if the redshifts of the lens and the source, and the lens model, which provides $\tau(\vec{x_1},\vec{y})$ and $\tau(\vec{x_2},\vec{y})$, are known. This way of estimating H_0 is more direct and robust than using standard distance ladder methods, which introduces sources of uncertainties at each step. GL is independent of astrophysical processes such as galactic dynamics, evolution of stars and galaxies and dust formation and a deep understanding of these processes is not needed, unlike in cases where the classical methods are used. On the other hand, the determination of lens mass-models is the most crucial step in that, presently, the errors in the estimation of the Hubble constant are dominated mostly by uncertainties in the lens models.

1.3 Lens modeling

1.3.1 Circularly symmetric lens models

A simple and illustrative lens model for galaxies is one with a circular-symmetric surface mass density, $\Sigma(\vec{\xi}) = \Sigma(\xi)$. Even though these models are very unrealistic in that real galaxies and clusters of galaxies are never perfectly or even near-circular, the underlying principle of most lens-models is similar to that presented here.

To avoid singular or discontinuous surface-mass density distributions, models such as softened isothermal spheres (see below) or ellipsoids (Sect. 1.3.2) and the Plummer model (Blandford & Kochanek 1987) have been greatly in use until recently. The Hubble Space Telescope (HST) observations of early-type galaxies have revealed galaxy cores to be quite cuspy in nature (Kochanek et al. 2004; Evans & Wilkinson 1998; Faber et al. 1997). Also, the fraction of systems with an even number of visible images is large whereas the general lens theorem predicts an odd number of images (Sect. 1.2). Hence there is a strong motivation to investigate lens models that provide cuspy cores and naturally provide an even number of images for

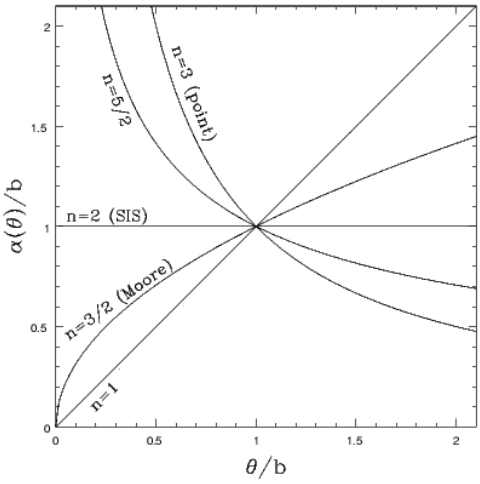

Figure 1.4: The power law models with $n > 2$ produce deflection angles (in units of the Einstein angle) that diverge at the lens centre. For the singular isothermal sphere (SIS), $n = 2$, the deflection angle is a constant and is equal to the Einstein radius (Kochanek et al. 2004, and references therein).

certain cases. The current family of circularly symmetric lens models focuses on a power-law profile[2] given by,

$$\rho \propto r^{-n} \quad ; \quad \alpha = b\left(\frac{\theta}{b}\right)^{2-n}, \tag{1.20}$$

$$\kappa = \frac{3-n}{2}\left(\frac{\theta}{b}\right)^{1-n} \quad ; \quad \gamma = \frac{n-1}{2}\left(\frac{\theta}{b}\right)^{1-n}, \tag{1.21}$$

where b is the Einstein radius given by Eq. 1.6. In this formalism, for $n \geq 2$, certain source-lens-observer configurations result in an even number of images. A particularly simple case, variants of which are universally used in lens-modelling, is one with $n = 2$ known as a singular isothermal sphere (SIS). Before going into the details of the SIS model, a few general remarks for circular power-law family of lens models are listed below:

1. The two eigenvectors of the inverse magnification matrix (M^{-1}) point in the radial and tangential directions with eigenvalues $(1 - \kappa + \gamma)$ and $(1 - \kappa - \gamma)$ respectively.

2. $n \rightarrow 1$ corresponds to a sheet of constant surface mass density and resembles the Navarro, Frenk & White (NFW, 1996) halo model profile, halo model and Schechter formalism. but has a constant projected cusp surface density, $\kappa = 1$. For this model $\gamma = 0$ and $\alpha = \theta$.

3. For $n = 2$ (SIS), the deflection is a constant and equal to the Einstein radius, b. Also, $\kappa = \gamma = b/(2\theta)$. Isothermal models suffer from disadvantages of having infinite total mass and a divergent surface-mass density as x approaches the lens centre.

4. $n = 3$ is a point-mass with $\alpha = b^2/\theta$, $\kappa = 0$ and $\gamma = b^2/r^2$.

The deflection angle for different n as a function of distance from the lens centre is shown in Fig. 1.4. For $n > 2$, the deflection angle diverges. This has a qualitative implication that the line $x - y$ intersects the $\alpha(\theta)$ curve at exactly two points giving rise to two images.

[2]The vector notation can be dropped due to circular symmetry.

Singular isothermal sphere

This model is based on the assumption that the dark matter halos behave as particles of an idealized gas in thermal equilibrium, i.e. with Maxwellian velocity distribution, and which are bound to their gravitational potential well. The volume mass density has the following form,

$$\rho \;=\; \frac{\sigma_v^2}{2\pi G}\,\frac{1}{r^2}, \tag{1.22}$$

where σ_v is the one-dimensional dispersion velocity of the constituents of the lens and is independent of the radius. The circular velocity of the particles is also a constant and this property is exploited to explain the observed flat rotational curves of spiral galaxies. From Eq. 1.2, the projected surface mass density can be calculated,

$$\Sigma(\xi) \;=\; \frac{\sigma_v^2}{2G}\,\frac{1}{\xi}. \tag{1.23}$$

Using the above result to calculate the mass within the Einstein radius, ξ_0, and Eq. 1.6, the Einstein radius in terms of the observables (the one-dimensional velocity dispersion) and the angular diameter distances is,

$$\xi_0 \;=\; 4\pi\,\frac{\sigma^2}{c^2}\frac{D_{\rm l}D_{\rm ls}}{D_{\rm s}}. \tag{1.24}$$

The value of the Einstein radius defines the length scale for the dimensionless vectors $\vec{x}$ and $\vec{y}$ in Sect. 1.1.4. Therefore $|\vec{x}| = 1$ corresponds to the Einstein ring. Switching to dimensionless units, the lens attributes are

$$\kappa \;=\; \gamma \;=\; \frac{1}{2x} \quad ; \quad \alpha(x) = \frac{x}{|x|}\,, \tag{1.25}$$

$$y \;=\; x - \frac{x}{|x|} \quad ; \quad \mu = \frac{|x|}{|x|-1}\,. \tag{1.26}$$

Multiple images occur only for $|y| \leq 1$, i.e. the source is inside the Einstein ring, and there are two images produced. They are diametrically opposite to each other, with one at $y+1$ and the other at $y-1$. The $|y| = 1$ curve in the source plane is called the pseudo-caustic as the number of images changes from two to one as the source jumps over it outward. Its corresponding pseudo radial critical curve is at the origin. From Eq. 1.26, the magnification of the image inside the Einstein ring is negative and in turn the image at $|y|-1$ has inverse parity[3]. Using Eq. 1.12 (retaining its form in terms of ξ_0) and Eq. 1.24, the time-delay between the two images is

$$\Delta\hat{\tau} \;=\; \frac{(1+z_{\rm l})}{c}\left[4\pi\,\left(\frac{\sigma_v}{c}\right)^2\right]^2 \frac{D_{\rm l}D_{\rm ls}}{D_{\rm s}}\,2y. \tag{1.27}$$

1.3.2 Elliptical lens models

Observed galaxies are by no means circular in appearance. They appear to have, assuming that mass follows light, quasi-elliptical isophotes. Moreover, the lens galaxies in most doublets are misaligned with the images, which from the last section clearly does not conform

[3] An observational fact: In all double image lenses, the image closer to the lens has its parity flipped.

with axially symmetric lens models. Therefore, aspherical lens models are more realistic in describing deflector mass distributions.

Whereas lens models with elliptical *iso-densities* are a better representation of real galaxies, they have complicated analytic solutions for the deflection angle and the lens equation is not easily solvable (Kassiola & Kovner 1993; Kormann et al. 1994). Consequently, they are replaced with quasi-elliptical lens models, such as quadrupole lenses (a symmetric model + an external shear component) or lens models with elliptical *iso-potentials*, which are easier to investigate and analytically more tractable. The latter family of models has one major drawback. Lenses with elliptical iso-potentials are not always physically meaningful when translated into mass distributions. If the ellipticity exceeds a certain limit, the iso-density contours become dumbbell-shaped and can even develop negative values in some regions (Kovner 1989).

Although including asymmetry in lens models is inevitable, the inner parts of galaxies can be well described by isothermal-like models. In this thesis, therefore, the choice of model is the singular isothermal elliptical potential (SIEP). But in chapter 5, the effect of including non-isothermality on the magnification of the lensed images of an extended background source is investigated. Hence, it is convenient to start with general elliptical potentials and later restrict consideration to isothermal profiles. The forms and notations of the lens equation and other lens attributes which are used in this thesis in the context of the lens system B0218+357, particularly for the work described in chapter 5 and chapter 7, are given below.

Let x_1 and x_2 be the two dimensionless Cartesian coordinates in the lens plane. In a coordinate frame where the origin coincides with the centre of the lens and the orthogonal axes are aligned with the major and the minor axes of the ellipse, the form of an elliptical iso-potential is

$$\psi \;=\; \frac{\xi_0^{2-\beta}}{\beta}\, u^{\beta}, \tag{1.28}$$

where

$$u \;=\; \sqrt{\frac{x_1^2}{(1+\epsilon)^2} + \frac{x_2^2}{(1-\epsilon)^2}}. \tag{1.29}$$

β represents the slope of the radial profile and lies in the range $(0-2)$. $\beta = 1$ corresponds to an isothermal profile. ξ_0 is the Einstein radius. If the ellipticity of the potential is described in terms of the ratio, q, of the minor axis to the major axis of the ellipse as $\epsilon' = 1 - q$, then the relation between ϵ, ϵ' and q for the above form of the potential is

$$q \;=\; \frac{b}{a} \;=\; \frac{(1-\epsilon)}{(1+\epsilon)} \;\approx\; 1 - 2\epsilon \;=\; 1 - \epsilon', \tag{1.30}$$

where the penultimate step is obtained assuming small ϵ. The convergence, κ, can be determined from the Laplacian of the potential and is given by

$$\kappa \;=\; E_0\, u^{\beta-2} \left[\frac{(1-\epsilon^2)}{(1+\epsilon)^2(1-\epsilon)^2} + \frac{\beta-2}{2}\,\left(\frac{v}{u^2}\right)\right], \tag{1.31}$$

where $E_0 = \xi_0^{2-\beta}$ and

$$v \;=\; \frac{x_1^2}{(1+\epsilon)^4} + \frac{x_2^2}{(1-\epsilon)^4}\,. \tag{1.32}$$

The iso-density contours defined by constant κ in Eq. 1.31 retain elliptical forms only for small ellipticities. Assuming that to be the case, the axis ratio of the corresponding iso-density contour is

$$\left(\frac{b}{a}\right)_\kappa = \left(\frac{1-\epsilon}{1+\epsilon}\right)\left[\frac{1+(\beta-2)(1-2\epsilon)/2}{1+(\beta-2)(1-2\epsilon)/2}\right]^{\frac{1}{\beta-2}},$$

$$\left(\frac{b}{a}\right)_\kappa = 1-2\epsilon\left(\frac{\beta+2}{\beta}\right). \tag{1.33}$$

Thus for isothermal profiles ($\beta = 1$), the axis ratio of the iso-density curves is $1-6\epsilon$ and the ellipticity is three times that of the iso-potential curves. Since ϵ and the ellipticity ϵ' are closely related and in what follows the main usage is of ϵ rather than ϵ', hereafter ϵ will be called the ellipticity unless specified. The orthogonal components of the deflection angle are,

$$\alpha_1 = E_0\,\frac{x_1}{(1+\epsilon)^2}\,u^{\beta-2} \quad ; \quad \alpha_2 = E_0\,\frac{x_2}{(1-\epsilon)^2}\,u^{\beta-2}. \tag{1.34}$$

Therefore, the two component lens equation reads,

$$y_1 = x_1 - \alpha_1 \quad ; \quad y_2 = x_2 - \alpha_2\,, \tag{1.35}$$

and the components of the Jacobian or the inverse magnification matrix are

$$M_{11} = 1 - \frac{E_0}{(1+\epsilon)^2}\,u^{\beta-2} - \frac{E_0(\beta-2)}{(1+\epsilon)^4}\,x_1^2\,u^{\beta-4},$$

$$M_{22} = 1 - \frac{E_0}{(1-\epsilon)^2}\,u^{\beta-2} - \frac{E_0(\beta-2)}{(1-\epsilon)^4}\,x_2^2\,u^{\beta-4},$$

$$M_{12} = M_{21} = -\frac{E_0(\beta-2)}{(1+\epsilon^2)(1-\epsilon^2)}\,x_1x_2\,u^{\beta-4}. \tag{1.36}$$

2 The gravitational lens JVAS B0218+357

The prime goal of this thesis is the investigation of the flux ratio anomaly found for the double-imaged quasar JVAS B0218+357. Before discussing the general characteristics of this lens system, one should note that there exist already two theses dedicated to B0218+357: "Investigations of the gravitational lens system B0218+357" by Andrew Biggs (2000) and "Lens models for compact and extended sources" by Olaf Wucknitz (2002). Both studies have contributed to our understanding of this gravitational lens system. One of the most important results of the first study is a value for the time-delay between flux variations of the two lensed images of B0218+357, measured with an accuracy of $\lesssim 2$ % at the 1 σ confidence level, which is a factor three to four better than other time-delay measurements for this system (Cohen et al. 2000; Corbett et al. 1996). The second study succeeded in constraining the position of the lens (which cannot be reliably determined in the optical due to the small image separation) using detailed observations of the radio structure of the lensed source (two compact images and an Einstein ring), by applying a modified version of the LensClean algorithm. This was then used to determine the value for the Hubble constant from the time-delay measurements of Biggs et al. (1999), which is in quite good agreement with the results from the WMAP project (Spergel et al. 2003) and the HST key project (Mould et al. 2000).

This work concentrates on a puzzling feature associated with B0218+357, which has not been investigated in detail before. It is related to the non-dispersive nature of gravitational lensing which entails frequency-independent magnification of lensed images (Sect. 1.1.5). Independent, multi-epoch and multi-frequency observations of B0218+357 indicate a chromatic and systematic change in the flux-density ratio of its images. This curious and unexpected behavior has drawn attention many times prior to this work. Before attacking the problem, it is essential to probe the characteristics of this lens system, which are known from both previous and contemporary studies, and which shed light upon the mechanisms responsible for introducing chromaticity. The focus of this chapter is mostly on these features, which ultimately will lead to defining the problem more concretely.

2.1 History of the discovery

The first appearance of B0218+357 was in the S3 radio survey, which was the third in a series to investigate the properties of radio sources at 5 GHz, made using the 140 ft telescope at Green Bank, National Radio Astronomy Observatory (NRAO) (Pauliny-Toth & Kellermann 1972). Its identification was made on the basis of the Royal Radar Establishment (RRE) interferometric position by Adgie (1974), measured at an observing frequency of 2695 MHz, yielding a position accuracy of 0.5 arcsec. The measured source flux-density was 1 Jy. From this and optical positions measured on the Palomar Sky Survey plates, the first target optical observation of 0218+35 (as it was catalogued then) was made by Johnson (1974) using a two-coordinate Grant measuring engine at Kitt Peak National Observatory. Johnson listed 0218+35 as a neutral or red object with a R–band magnitude of $m_R \approx 20$, which could be

a high-redshift QSO or an object similar to BL Lac. Thus, there was no knowledge of its double nature due to the limited resolution.

B0218+357 was identified as a gravitational lens nearly two decades later in the Jodrell-Bank VLA[1] Astrometric Survey (JVAS) of radio sources (Patnaik et al. 1992c; King et al. 1997; Browne et al. 1998; Wilkinson et al. 1998) using the VLA in A–configuration at 8.4 GHz. The sources were selected on the criteria of flat-spectral indices ($\alpha \leq 0.5$) between 1.4 GHz and 5 GHz and $F_{5\ \mathrm{GHz}} \geq 200$ mJy, where the flux-density $F \propto \nu^{-\alpha}$ (See Appendix B.2). The prime objective of the survey was to select phase-calibrator sources for the Multi-Element Radio-Linked Interferometer Network (MERLIN, Jodrell Bank) and VLBI networks also. The second objective was the search for gravitational lenses, which was achieved by selecting those sources which showed more than one compact flat-spectrum component. Of $\sim$ 2000 sources from the first survey, 14 gravitational lens candidates, including B0218+357, were marked for further investigations with the VLA at three frequencies (8.4, 15 and 22 GHz), followed by MERLIN observations at 5 GHz (Patnaik et al. 1992a). The MERLIN map of B0218+357 clearly showed two compact components separated by $\sim$ 335 mas, together with an Einstein ring of the same diameter, and the composition was similar to the 5 GHz MERLIN map obtained by Zensus & Porcas (1985). The two components were found to have similar spectral indices ($\alpha \sim 0.2$) and the same fractional linear polarization ($\sim$ 10 %) at different frequencies. Hence, the high-degree of similarity between the two nearby components was regarded as a proof that B0218+357 is a gravitationally lensed system (Patnaik et al. 1993), in which a background radio source is lensed by a foreground galaxy into two images. The angular separation between the images is the smallest amongst the known galactic-type lenses.

2.2 Nature of the lens and the lensed object

A crucial test to confirm gravitational lens candidates is provided by redshift measurements. Multiple emission lines at two different redshifts in the spectrum of the targeted galaxy are strongly in favour of gravitational lensing. Further, the redshifts of the lensed and lens objects, together with the lens model, are essential for the determination of the Hubble constant (see Sect. 1.2.3).

The first estimate of the redshift of the lens galaxy in JVAS B0218+357 was made by O'Dea et al. (1992) on the basis of tentative detections of the 4000 Å break of the stellar population of a galaxy and the G–band absorption feature, suggesting a redshift of 0.68. Although up to this point it was not clear if the redshift was that of the lens or the lensed object, as the optical resolution included both, this put the lensed radio source at a redshift of $z \geq 0.68$. Browne et al. (1993) re-observed this system spectroscopically and even though they did not detect any of the features that were observed by O'Dea et al. (1992), based on detections of other spectral lines they obtained the same value for the redshift, $z = 0.68466 \pm 0.00004$. Further, a large differential Faraday rotation ($\sim$ 900 rad m^{-2}) between the images had already been established by Patnaik et al. (1992a), which could arise only due to different path lengths or properties in the medium of the lens galaxy (along the lines of sight to the images) and not the background source. From this, Browne et al. (1993) concluded that the lens galaxy is rich in ionized gas and, therefore, is the origin of the observed absorption and emission features. They also suggested its morphology-type to be spiral on the same grounds. Detections of Hβ and [OIII] 5007 Å emission lines shown in Fig. 2.1, common to late-type spirals, supplied

[1] Very Large Array, an array of 27 telescopes in New Mexico, NRAO

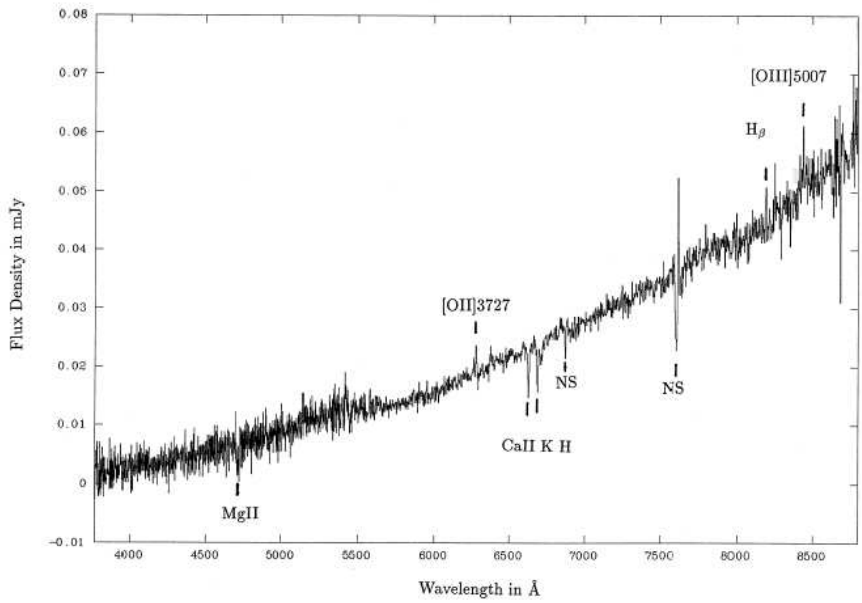

Figure 2.1: Spectral lines of B0218+357 obtained with the William Herschel Telescope (WHT) (Browne et al. 1993) giving a mean redshift of 0.6847 for the lens galaxy. [OIII] 5007 Å and Hβ emission lines are indicative of a late-type spiral. 'NS' denotes a night sky feature.

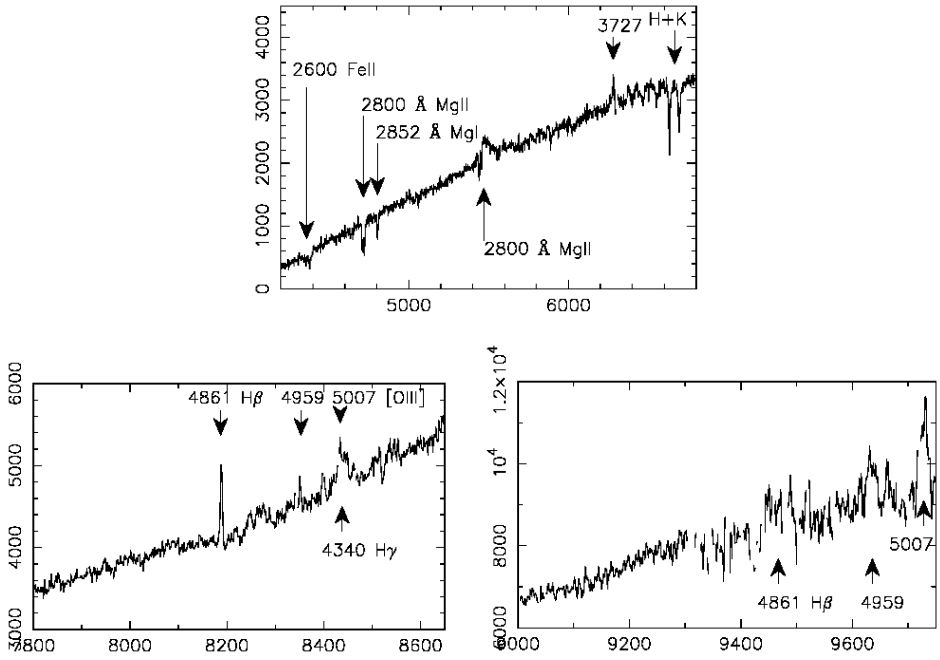

Figure 2.2: Spectra of B0218+357 from 4200 Å to 9750 Å split into three regimes (Cohen et al. 2003). Plotted on the y–axis is the Analog Digital Unit (ADU) per pixel. The five broad emission lines labelled below the spectrum are from the lensed object giving a redshift of 0.944.

further support to this view. The same value for the lens redshift has been independently established based on optical measurements by Stickel & Kuhr (1993) and the detection of neutral hydrogen 21 cm absorption by Carilli et al. (1993). Additionally, firm molecular line detections of CO, HCO^+ and HCN (Wiklind & Combes 1995) at the redshift of the lens galaxy enable a consistent picture of the lens-screen to be developed. The H I absorption lines, the small separation between the images, the high rotation measure and the red-optical spectrum ($\alpha \sim 3.5$) of the background object is naturally explained by a spiral lensing galaxy which is low-mass and gas-rich.

The lensed object has properties of a powerful radio source and lacks in strong emission lines, which indicate a BL Lac–type object. Apart from the absence of any strong spectroscopic lines, BL Lacs are active galaxies (Kembhavi & Narlikar 1999; Robson 1996) which are very similar to flat-spectrum ($\alpha < 0.5$) radio-loud quasars. They have a non-thermal continuum emission with large amplitude flux variations in the radio, optical and X-ray bands. Further, they exhibit strong linear polarization with rapid variability. BL Lacs and another similar class of active galaxies, which are extremely variable in the radio and optical, known as OVVs (Optically Violently Variable quasars), are collectively grouped into the category known as blazars.

Browne et al. (1993) recognized some additional distinct features in the spectrum of B0218+357, which they hypothesized to be associated with the background object. This led them to suggest a value of $z \approx 0.94$ for its redshift. Although Cohen (1996) and Lawrence (1996) obtained nearly the same redshift value for the lensed object, the final determination proved to be much more difficult since its blazar-like spectrum was devoid of strong emission lines. The confirmation was finally made by Cohen et al. (2003) through detection of five broad emission lines, shown in Fig. 2.2, giving $z = 0.944 \pm 0.002$.

2.3 Structure of B0218+357

B0218+357 is well-studied GL system with observations at several radio-wavelengths and optical bands. At radio wavelengths only the background object is seen, which is an active galaxy, and which shows a rich and extended structure. Before discussing various observed features of this lens system, it will be beneficial to review the basic properties, the radio morphology in particular, of an active galaxy.

2.3.1 Active galaxies

An active galaxy is a galaxy with a total luminosity (over all wavelengths) a thousand-fold larger than normal galaxies. The emission originates from the very centre of the galaxy, which contains a supermassive black hole. The class of galaxies which display signs of such energetic activity is called Active Galactic Nuclei (AGN). They have continuum emission over the entire electromagnetic spectrum, extending from the gamma-ray to the radio.

An important feature in the emission of most AGN, whose spectra are dominated by radio emission, is a compact region called the core, which coincides with the optical nucleus of the galaxy. In addition to this bright nucleus of emission in AGN, there exist well-collimated outflows extending from the compact core emission to several tens of parsec to hundreds of kiloparsec. Such elongated features are termed jets. Using the technique of VLBI and angular resolutions better than 1 milliarcsecond, the cores of numerous radio galaxies have been studied in detail (e.g. Kellermann et al. 1998). They exhibit jets emanating from an

unresolved and flat spectrum component. In the jargon of VLBI, it is this component, which at a given frequency remains unresolved, that is called the "core". The jets are often resolved into smaller components, which through multi-epoch observations have been ascertained to be in motion with respect to a stationary core (e.g. Unwin et al. 1989; Hummel et al. 1992), with apparent speeds greater than the speed of light. This peculiar phenomenon can be explained by a geometrical effect and referred to as superluminal motion (see Appendix C.1)

The radio emission of AGN is due to synchrotron emission from a power-law distribution of electrons in the jet plasma. The resulting spectra have a typical power-law dependence on frequency, $F_\nu \propto \nu^{-\alpha}$. Further, the spectra can be characterized by two power-law indices depending on whether the frequency of observation is higher or lower than the turnover frequency due to synchrotron self-absorption, ν_a. If $\nu > \nu_a$ the spectral index is $\alpha > 0$, which is characteristic of synchrotron emission and if $\nu < \nu_a$, the spectral index is $\alpha < 0$ (see Appendix B).

The synchrotron self-absorption process becomes enhanced at low frequencies and at decreasing distances from the central engine (due to high optical depth at a given frequency). Therefore, the jet-subcomponents seen using high-resolution VLBI observations peak at different frequencies and at varying distances from the central engine. The superposition of their spectra, when observed with low resolutions such that they remain unresolved, results in the spectrum of the radio-jet appearing flat. This has the following natural consequence. As the radio AGN are observed at higher and higher frequencies, the flux from the extended components, due to their steeper spectra and a smaller beam-size ($\sim \lambda/D$) drops out. Thus, the most compact subcomponent that is detected, which forms the base of the jet, moves closer to the central engine with increasing frequency of observation. This effect is known as core-shift and has been studied in detail by several groups including Lobanov (1998), Blandford & Konigl (1979) and Marcaide et al. (1985). The study of core shift as a function of frequency can reveal interesting physical properties about the radio sources, such as the jet luminosity, and the geometrical properties of the jets and the core magnetic fields (Lobanov 1998). This property might be important in the context of the image flux ratio anomaly associated with B0218+357, which is discussed in Sect. 2.6, and its effect will be measured in chapter 3.

2.3.2 Radio

Shown in Fig. 2.3 is a 15 GHz VLA map of B0218+357 with a resolution of 120 mas. The two compact flat-spectrum components, A (right) and B (left)[2], are the lensed images of the same background radio source. The image separation is $\sim$ 334 mas and is the smallest known angular separation for a multiply imaged system[3]. The images are embedded in the steep-spectrum ($\alpha \sim 0.6$) radio emission from the Einstein ring of a similar diameter with an amorphous morphology. Fig. 2.3 also shows jet-like emission extending $\sim$ 2 arcsec south-east of image A. This extended emission is identified with the jet of the lensed radio source, which due to its large separation from the lens galaxy is not affected by the lens galaxy. Lower-resolution VLA maps at $\sim$ 1.4 GHz (Patnaik et al. 1993; O'Dea et al. 1992) show the entire extent of the radio structure to be of the order of $\sim$ 30 arcsec. This is shown in Fig. 2.4 where

[2]Due to the observed order, the images are positioned in the same format throughout this thesis, i.e. image A on the right and image B on the left

[3]Of the known multiply imaged systems, the angular separation is on subarcsec scales in about $\sim$ 20 % and < 0.5 arcsec in $< 5\%$ of them.

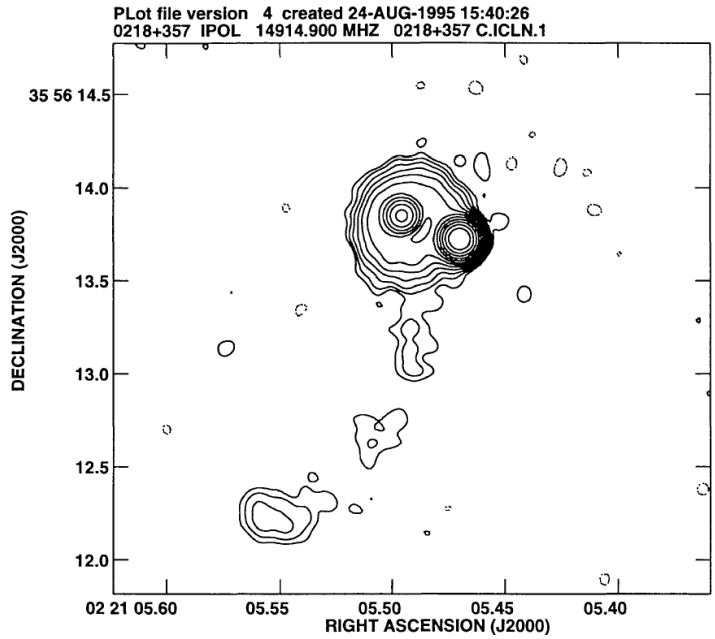

Figure 2.3: Map of B0218+357 obtained with the VLA at 15 GHz (Corbett et al. 1996). The two compact images A (right) and B (left) and the Einstein ring are clearly discernable. Also visible is additional emission extending southeast from image A at distance ~ 2 arcsec which is not multiply imaged. The resolution of the VLA at 15 GHz is 120 mas.

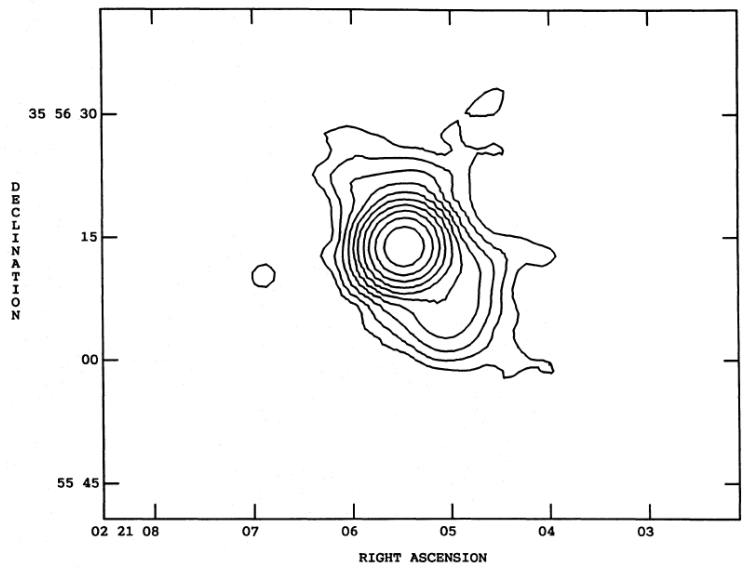

Figure 2.4: A low-resolution VLA map of B0218+357 at 1.465 GHz with a resolution of 4.9 arcsec (Patnaik et al. 1993). The high-sensitivity of the VLA allows the extended low-brightness emission which extends out to ~ 30 arcsec from A+B to be clearly detected. The contour levels are at $(1.5, 3, 6, 12, \ldots, 768)$ mJy beam^{-1}.

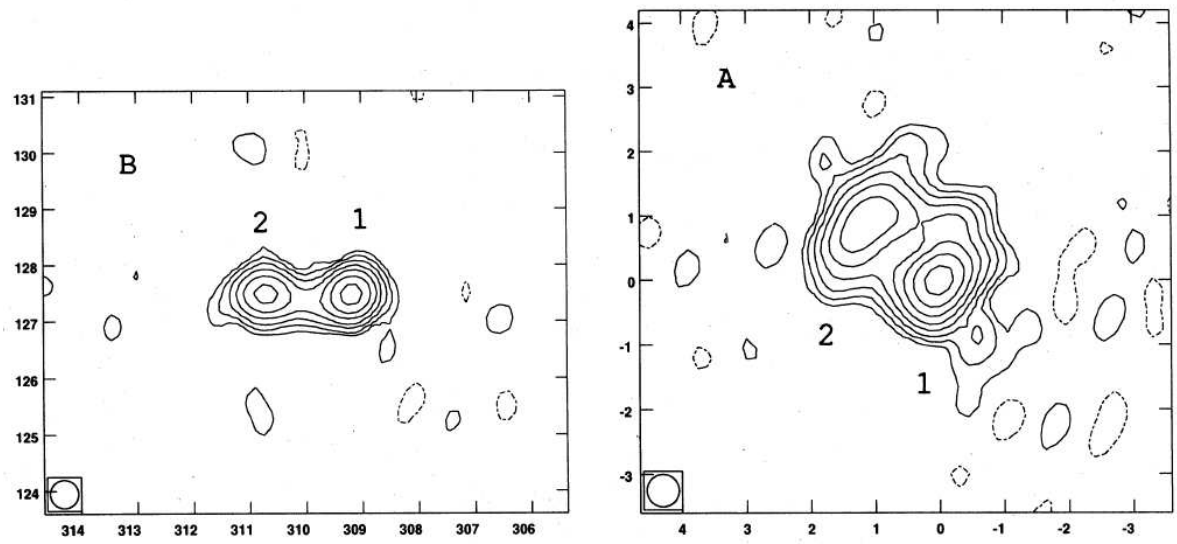

Figure 2.5: VLBA maps of B0218+357 made at 15 GHz with 0.5 mas resolution (Patnaik et al. 1995). The contour levels for image B are 1.5 mJy beam$^{-1}\times$(-1, 1, 2, 4, 8, 16, 32, 64, 128) and the peak flux density is 130.8 mJy beam^{-1}. The contour levels for image A are 2 mJy beam$^{-1}\times$(-1, 1, 2, 4, 8, 16, 32, 64, 128, 256) and the peak flux density is 381.4 mJy beam^{-1}. The tick interval is 1 mas.

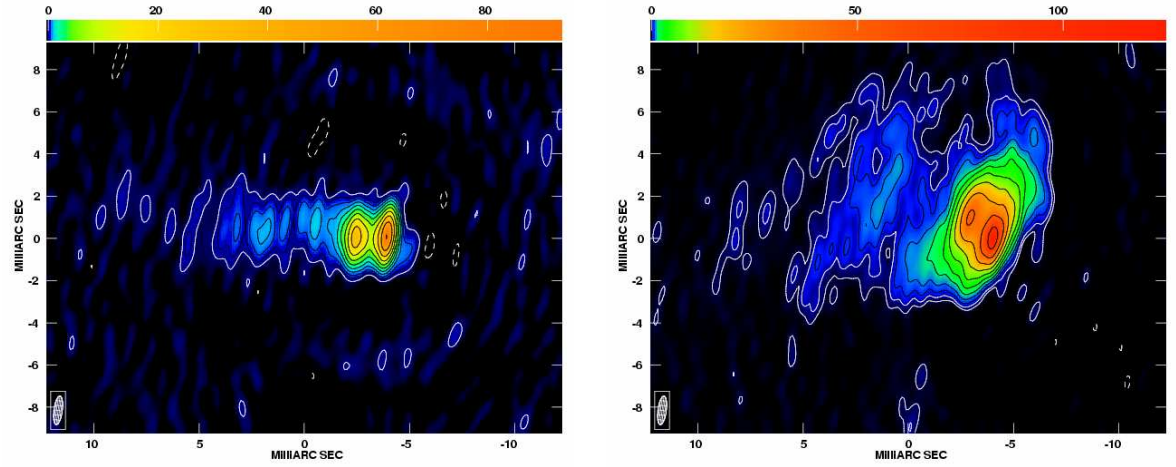

Figure 2.6: Global VLBI maps of B0218+357 at 8.4 GHz with an elliptical restoring beam of FWHM 1.36 $\times$ 0.41 mas^2 and position angle $-7°.5$ (Biggs et al. 2003). The contour levels are 90 μJy beam$^{-1}\times$(-1, 1, 2, 4, 8, 16, etc).

the images A and B are encompassed by a steep spectrum asymmetrical bed of emission of along the NE–SW elongation.

High-resolution maps of B0218+357 using long baseline interferometers, such as the VLBA and the VLBI networks, reveal A and B to consist of two distinct components with similar separations ($\gtrsim$ 1 milliarcsecond) but with different relative shapes and orientations. The 15 GHz VLBA maps shown in Fig. 2.5 distinctly reveal the subcomponents in each image. The more compact and stronger of the two components (western) is labeled in the images as A1 and B1, and the weaker as A2 and B2. The double features are identified with the core-jet

morphology of a flat-spectrum radio source (Sect. 2.3.1), with component 1, based on its high turn-over frequency, as the core or the jet-base, and component 2 as a jet-component. This phenotypical core-jet picture of the background source is more pronounced in the 8.4 GHz global VLBI maps by Biggs et al. (2003) shown is Fig. 2.6. Here, component 1 is the most westerly peak in each image recognized as the core and component 2 is the second brightest feature, east of component 1. The low-brightness emission constituting the jet is seen to extend out to $\sim$ 15 mas to 20 mas from the core in both the images. Note that the entire structure of image A, including the subcomponents, is stretched out in a direction orthogonal to the A and B separation. No such elongation is visible in image B. Even though the lensed radio source has properties similar to those of BL Lac objects, which in the framework of unification schemes of AGN have no counter-jet, there have been suggestions of one by Biggs et al. (2003) based on the narrow elongated feature seen poking out of the edge, west of component 1, in both A and B images of Fig. 2.6.

The spiral lens galaxy, on the other hand, has not been detected to have any radio emission to date. The absence of radio emission at the expected position of the lens galaxy in the global VLBI maps obtained by Biggs et al. (2003) with a rms sensitivity of $\sigma = 30$ μJy beam^{-1}, led the authors to conclude that the peak surface brightness of the lensing galaxy is less than 180 μJy beam^{-1} assuming a confident detection at a noise level of 6 σ.

2.3.3 Optical

The optical emission of B0218+357 can be decomposed into contributions by the lensed images, A and B, and the spiral lens galaxy. The system has been detected in the I and V bands using the ground-based Nordic Optical Telescope (Grundahl & Hjorth 1995) and the H, I and V bands using the Near Infrared Camera and Multi-Object Spectrometer (NICMOS, NIC1 and NIC2), the Wide Field Planetary Camera 2 (WFPC2) and the Advanced Camera for Surveys (ACS) mounted on the HST (Lehár et al. 2000; Jackson et al. 2000; York et al. 2005).

These observations throw light upon several characteristics associated with this system. Shown in Fig 2.7 is an ACS image of B0218+357 in which A and B are seen resolved from each other. Firstly, it is apparent that image B dominates the overall optical emission and is brighter than image A, the reverse of which is true at all radio wavelengths. The relatively weak emission from the lens blends with that of image B. However, the spiral arms of the lens galaxy are visible, and face-on in appearance. While this is in agreement with the previous observations and conclusions (Grundahl & Hjorth 1995; Wiklind & Combes 1995), the off-axis alignment of the lens center and the lensed images demands the mass distribution to be aspherical (Grundahl & Hjorth 1995; Patnaik et al. 1995) (see Sect. 1.2.2). This discrepancy can be resolved by introducing a bar or bulge component into the spiral geometry of the lens.

Secondly, due to the extreme smallness of the image separation, the lens galaxy is not easily separated from the bright images which makes the determination of the lens position relative to A and B very difficult at the milliarcsecond level. The estimation is made especially difficult by the humongous peak surface brightness of image B which is 30 to 50 times greater than that of the lens (York et al. 2005). Nevertheless, vigorous efforts have been made to register the position of the lens galaxy with respect to the lensed images. The lens position obtained by various groups using optical techniques and their details are given in Table 2.1. The lens positions obtained from the HST/NIC1 and HST/NIC2 observations at infrared wavelengths by Lehár et al. (2000) are discordant with each other by 46 mas and the average

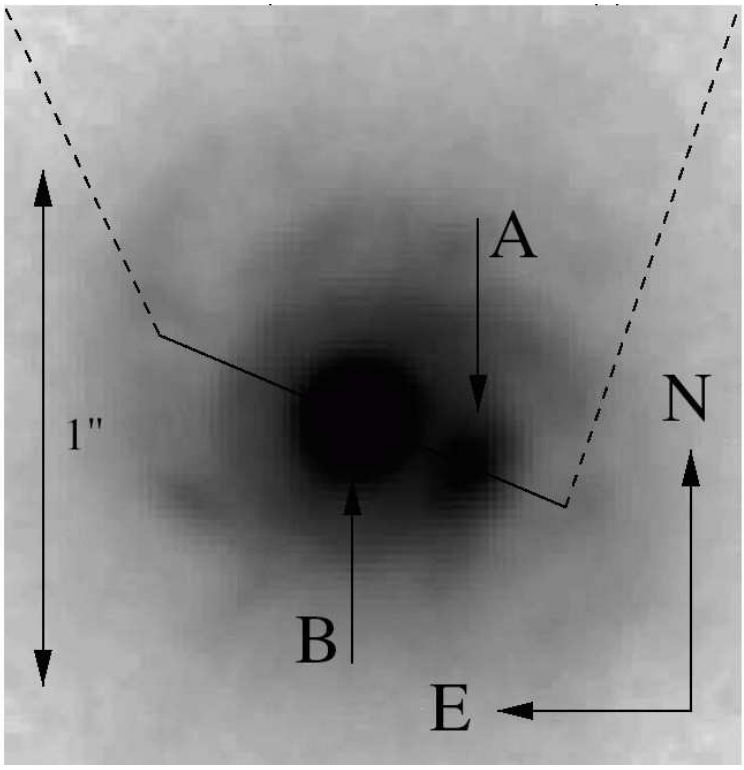

Figure 2.7: This image of B0218+357 produced by York et al. (2005) using the Advance Camera for Surveys on HST, best illustrates the optical features of the system. The optical emissions of image A and image B are distinguishable. The lens galaxy blends completely with image B but its spiral arms are beautifully displayed.

value is accurate only to within $\sim$ 10 % of the A to B separation. The analysis of recent ACS observations by York et al. (2005) found that a parametric galaxy model and two point sources does not result in a sufficiently constrained lens position. On combining their data with the VLBI constraints, the lens position is altered by about 13 mas. The disagreement between the values of the lens position has a detrimental impact on the determination of the Hubble constant. This can be realized by going back to Eq. 1.18 which relates the observed time delay between the images and the image positions. For the case of an isothermal profile, the scale-free potential (obtained by substituting $\beta = 1$ in Eq. 1.28) is

$$\psi \propto u = \sqrt{\frac{x_1^2}{(1+\epsilon)^2} + \frac{x_2^2}{(1-\epsilon)^2}}, \tag{2.1}$$

such that

$$\psi = x_1\vec{\nabla}_1\psi + x_2\vec{\nabla}_2\psi = \vec{x}.\vec{\nabla}\psi\,, \tag{2.2}$$

where $\vec{\nabla}_k$ denotes the vector derivative with respect to the k^{th} Cartesian coordinate and $\vec{\nabla}_{k(=1,2)}\psi$ can be readily identified as the orthogonal components of the deflection angle defined in Eq. 1.34. Using this result and the lens equation, the relative scale-free time delay between two lensed images can be simplified from

$$\tau_i - \tau_j = \frac{1}{2}\left[(\vec{x}_i - \vec{y})^2 - (\vec{x}_j - \vec{y})^2\right] - \psi(\vec{x}_i) + \psi(\vec{x}_j) \tag{2.3}$$

Table 2.1: The galaxy separation, image separation and the image flux-density ratio (B/A) obtained from optical observations are given below. For the data from to York et al. (2005), the two values for the galaxy position relative to image B correspond to analysis without and with masking of the spiral arms respectively, and the three values for the image separation are for different functional forms of the point spread function (PSF) used for the fitting: field star PSFs, Gaussian PSFs and Airy function PSFs respectively. The V, I and H bands correspond to 555 nm, 814 nm and 1.6 μm filters, respectively. The galaxy positions are decomposed into two components corresponding to RA (east as positive) and Dec. (north as positive)

.

Author	Details	Gal. pos. (mas)	B−A sep. (mas)	B/A
1	I (WFPC2)		299±10	6.85
	V (WFPC2)		296±10	5.85
		With respect to A		
2	H (NIC1)	178,46	332±3	
	H (NIC2)	184,92	330±3	
	Avg.	(181,69)±30		
3	V (WFCP2)		308±10	6.5±1.7
	I (WFCP2)		311±11	9.5±2.6
	H (NIC1)		318±5	1.58±0.16
		With respect to B		
4	I (ACS)	57±4,1±6	317±2	
		75±6,-6±13	315±4	
			311±10	

[1] from Hjorth (1997)
[2] from Lehár et al. (2000)
[3] from Jackson et al. (2000)
[4] from York et al. (2005)

to

$$\tau_i - \tau_j \;=\; \frac{1}{2}\left[\vec{x}_i^{\,2} - \vec{x}_j^{\,2}\right] - \vec{x}_i^{\,2} + \vec{x}_j^{\,2} \;=\; \frac{\vec{x}_j^{\,2} - \vec{x}_i^{\,2}}{2}. \tag{2.4}$$

Therefore, from Eqs. 1.18 and 1.19, the observed time delay between the images is

$$\Delta\hat{\tau} \;\propto\; H_0^{-1}\left[\frac{\vec{x}_j^{\,2} - \vec{x}_i^{\,2}}{2}\right] \tag{2.5}$$

Hence, the time delay between two lensed images for an isothermal potential is simply related to the Hubble constant and the image positions *relative* to the lens centre (Witt et al. 2000). Even though the radio positions of A and B relative to each other are known to an accuracy of a few tens of microarcseconds, it is crucial to have an accurate position for the lens galaxy for determining the value of the Hubble constant. The Hubble constant as a function of lens position (x_0, y_0) for isothermal models is shown in Fig. 2.8, which is taken from Wucknitz et al. (2004), and obtained from the time-delay measured by Biggs et al. (1999) and for the

concordance ΛCDM model with $\Omega_m = 0.3$ and $\Omega_\Lambda = 0.7$. Also shown in the same figure are the lens positions estimated from the different optical datasets. For simple isothermal profiles it can be concluded that for every milliarcsecond shift in the position of the lens centre, a change of about 0.7 km s^{-1} Mpc^{-1} in the value of H_0 is induced. For the sake of completeness, the lens position estimated by York et al. (2005) in comparison with that obtained from the LensClean algorithm (Wucknitz et al. 2004, discussed in chapter 4) is also presented in Fig. 2.9.

Finally, what adds to the list of confusions is a consistent mismatch between the A to B separation observed in the radio and in the optical. The optical image separation is listed in Table 2.1 in the fourth column. The values obtained by Hjorth (1997), Jackson et al. (2000) and York et al. (2005) are considerably lower than the well-defined radio image separation of 334 mas, although the difference is much larger from Hjorth (1997) ($\sim$ 37 mas) than the combined average of the positions ($\sim$ 21 mas) determined by Jackson et al. (2000) and York et al. (2005). The average separation measured by Lehár et al. (2000), on the other hand, matches the radio separation to an accuracy of two milliarcseconds.

The difference in the optical-radio separation is thought to be due to image A being partially or completely covered by a molecular cloud at the lens plane. Such a cloud is known to exist from spectral line observations. This would lead to the obscuration of a major fraction of the A emission at optical wavelengths, resulting in image B being brighter than its counterpart. York et al. (2005) argue that the shorter image separation in the optical compared to the radio is the result of extinction caused by the star formation region associated with the molecular cloud. This causes a shift in the centroid of A emission such that it is no longer coincident with the lensed radio source seen as image A at radio wavelengths. But this interpretation is

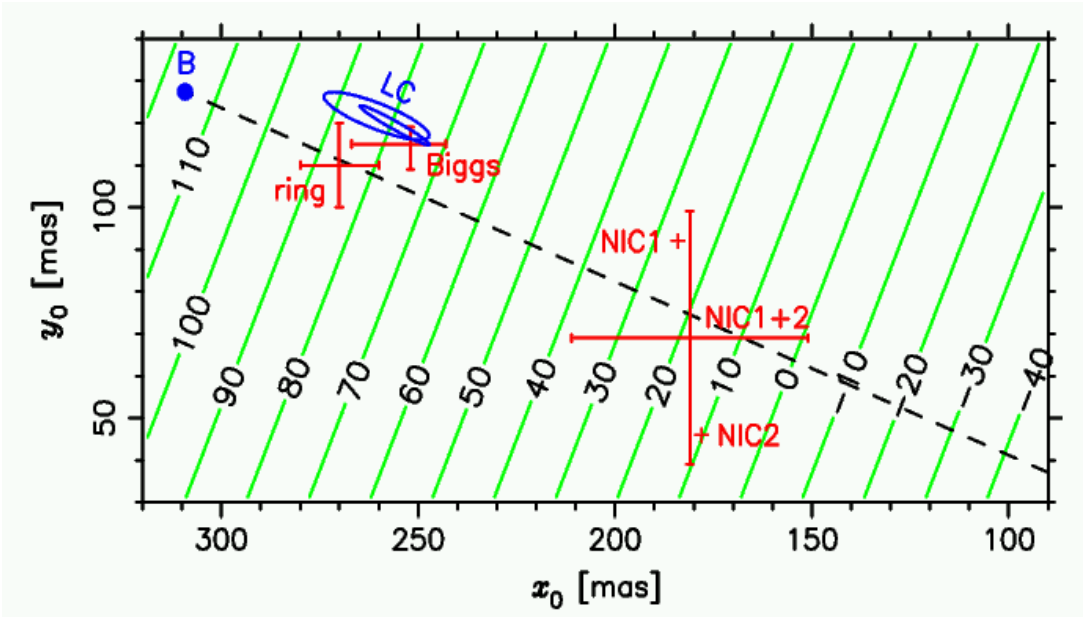

Figure 2.8: This figure exhibits the functional dependence of the Hubble constant (green lines) on the position of the lens galaxy for an isothermal profile (Wucknitz et al. 2004). Marked in the figure are the lens positions derived from the LensClean ("LC") algorithm (Wucknitz et al. 2004), NIC1 and NIC2 observations (Lehár et al. 2000), the results from Biggs et al. (1999) and assuming the centre of the Einstein ring ("ring") as the lens centre (Patnaik et al. 1993).

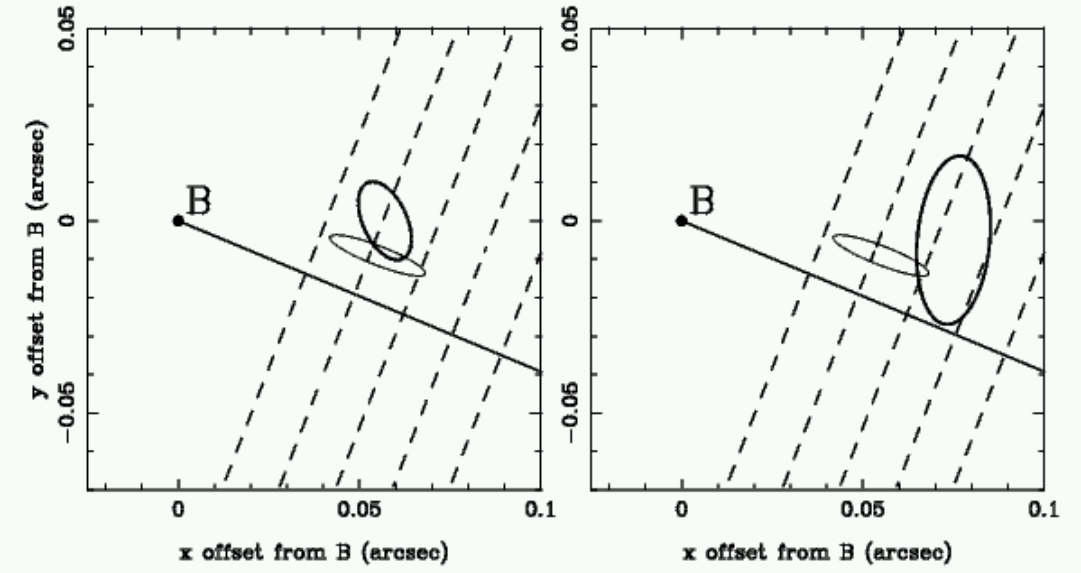

Figure 2.9: The optical lens position obtained by York et al. (2005) (thin ellipses) in comparison with that determined by Wucknitz et al. (2004) (bold ellipses) using an advance version of LensClean. To guard against the displacement of the lens position due to the possible asymmetry in the spiral arms about the lens centre, the left-hand plot was produced from masking off the spiral arms by using an annular mask. The right-hand plot did not employ any masking. Also shown are the dashed contours of H_0 for an isothermal profile, and correspond to (90, 80, 70, 60, 50) km s^{-1} Mpc^{-1}, from left to right.

not very convincing, as pointed out by Jackson et al. (2000), considering the point-like optical appearance of image A. One other possibility which can emerge is that the bright centre of emission is the core of the lensing galaxy instead of image B. This can be ruled out as such a bright galaxy is not compatible with the assumed low mass of the system.

2.4 Time Variability

The blazar-type lensed radio source is variable in its emission and the variability is reflected in the total and the polarized flux-densities of the images A and B. Due to the different geometrical and Shapiro delays at the image positions (see Sect. 1.1.3), the variations are seen at different times in the images, first appearing in image A and after a time-delay, in image B. The first-order prediction of the time-delay was made by Patnaik et al. (1993) ($\sim$ 6 days) from comparing it with B0957+561, also a double-image gravitationally-lensed quasar, and scaling the time-delay with respect to its image-separation and the image flux-density ratio. Shortly after, Corbett et al. (1996) obtained a more precise value, (12 ± 3 days), from the cross-correlation of radio image light curves and polarization curves. Due to the explicit dependence of H_0 on the time-delay as described in the previous section, the measurement of the time-delay is extremely desirable. The uncertainty in the determined value of H_0 includes a contribution from uncertainties in the lens model and the measured time-delay. The uncertainty in the time-delay measurement by Corbett et al. (1996) is very large (25 %) in comparison with the current level of uncertainties in the lens models, and dominate the net error in the estimation of H_0. Meanwhile, Biggs et al. (1999) have measured a more

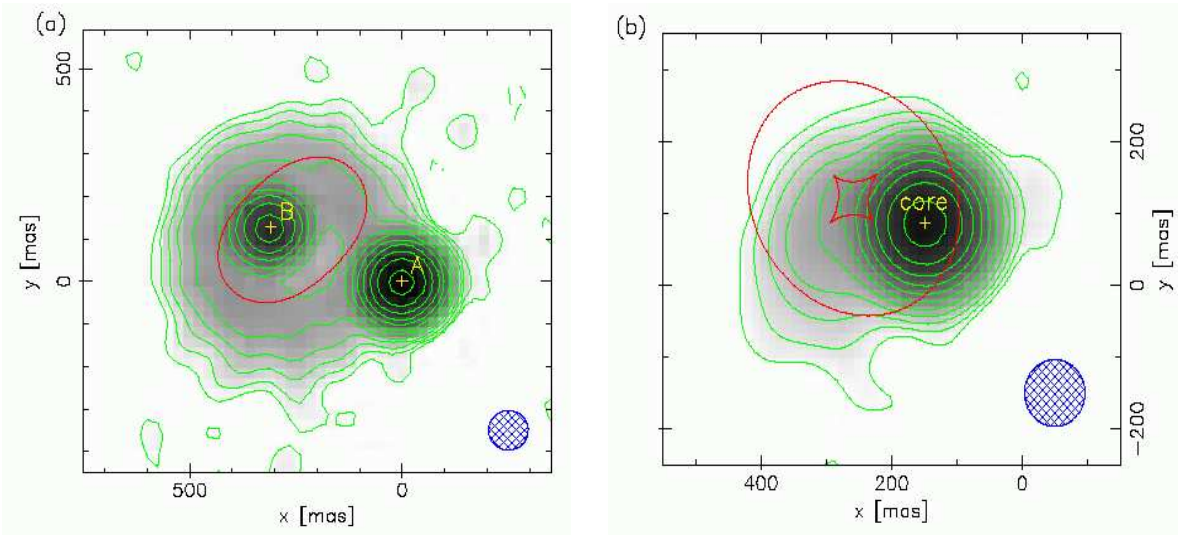

Figure 2.10: The brightness distribution maps of B0218+357 derived from an advanced version of the LensClean algorithm by fitting the model parameters to the radio interferometric data (Wucknitz et al. 2004). The contour levels are at $(1, 2, 4, 8, \ldots) \times 2\sigma$, where $\sigma = 0.28$ mJy beam^{-1}. (a) The lens plane map at the nominal resolution of 15 GHz VLA observations. The tangential critical curve is shown as a red ellipse. (b) The source plane map restored with a circular source plane CLEAN beam. Also shown are the astroid caustic (the inner one) and pseudo caustic (the outer one).

precise value, (10.5±0.4) days, which has an uncertainty reduced from 25 % to 2 %. They derived the result from monitoring data taken from October 1996 to January 1997 with the VLA at 15 GHz and 8.4 GHz. The time-delay was established by applying different delays between the polarization light curves as well as the flux density light curves for A and B. Independent VLA measurements at the same time and at the same frequencies were made by Cohen et al. (2000) who reported a time delay of $(10.1^{+1.5}_{-1.6})$ days. Their value has bigger error bars associated with it as they adopted a more general model for the source variability consisting of two components, a constant part and a varying part, with different magnification ratios. Yet the two results are consistent with each other and indicate the robustness of the time-delay measurements.

2.5 Lens geometry

From numerous observations of B0218+357 at different frequencies and epochs, the general picture of the lens geometry which has emerged consists of a radio source at a redshift of 0.94, lensed by a spiral galaxy[4] at a redshift of 0.68 into two images and an Einstein ring. The lens mass distribution is evidently not circularly symmetric as the core images A and B, and the centre of the Einstein ring do not lie on a straight line. Assuming a singular isothermal ellipsoid (SIE) as the model for either the lens mass distribution or the lens potential, the outer (tangential) critical curve is elliptical and the corresponding inner (tangential) caustic is astroid shaped as shown in Fig. 2.10 (Wucknitz et al. 2004). The source brightness distribution

[4] There are only five late-type spiral lens galaxies known based on morphology, color or molecular content, B0218+357, B1600+434, PMNJ2004−1349, Q2237−0305, and PKS1830−211 (Falco et al. 1999; Kochanek et al. 2004). Four of them are double-image systems while one is a four-image system.

in the lens and the source planes, shown in the left and right panels of Fig. 2.10 respectively, has been derived by fitting the lens model parameters to the radio observations of the core images and the details of the Einstein ring using the LensClean algorithm (described in chapter 4). Also shown in the right panel is the pseudo radial-caustic (Sect. 1.3.1), signifying the multiple image region. The 'core' marked in the source plane is lensed into the A and B images, and the jet emanating eastwards gets lensed into the Einstein ring when crossing the caustic.

2.6 Image flux-density ratio (A/B)

Even though the basic lensing characteristics of B0218+357 are well-understood and well-reproduced by the current lens models, there are a few complications. One of them is concerning the image flux-density ratio, A/B, which exhibits a consistent and systematic decline with decreasing frequency. As was pointed out in Sect. 1.1.5, the gravitational lensing effect produces only achromatic magnification of source flux densities and thereby achromatic image flux-density ratios. To understand this strange behaviour, firstly it is necessary to establish the authenticity of the chromatic trend observed and rule out the possibility of it being an instrumental artifact or due to an incomplete understanding of the flux distribution in the images. Table 2.2 lists the total image flux densities, the flux densities of components 1 and 2 (where available), and the ratios [(A/B), (A1/B1) and (A2/B2)], measured from previous observations.

To prove that the ratio of the total image flux-densities increases with increasing frequency is rather difficult. At first glance it appears as though the change in the ratio is arbitrary and does not follow any particular trend. To investigate the case, three important aspects related to the B0218+357 lensed images and interferometric measurements have to be considered :

- Source variability and time-delay between the images: At frequencies where the source is variable, the ratio measured at a single epoch will be in error if the time-scale for significant variations is comparable with the time delay. The three-month VLA monitoring of B0218+357 at 15 GHz and 8.4 GHz by Biggs et al. (1999) has revealed variations in the image flux-densities on a time-scale of 70 days to 100 days. This, along with the measured time-delay between the images, can induce variations in the image flux ratio at the level of 10 % to 11 %. This is in good agreement with the 15 GHz image flux ratios measured at the same epoch, with the mean value of 3.74 and an rms of 0.02. At 8.4 GHz, the level of the observed variation in the ratio reduces to 7 % to 8 % and the rms reduces to 0.01. It is indeed expected that the variability amplitude of the background radio source reduces with frequency as the contribution from non-variable radio components becomes larger. Hence, although the time-variability in the background source emission along with the time-delay between the lensed images results in the estimated image flux-density ratios exhibiting a spread at any given frequency, it is clearly not the cause of the observed chromaticity in the flux-density ratio.

- The effect of resolution: Gravitational lensing magnifies the images, A and B, by different factors. Since the surface brightness of the background source is a conserved parameter, the surface-brightness contours which are detectable in one image should be detected in the other as well. However, this is strictly true only for source areas (or components) of constant surface brightness that are completely resolved in both of the

Table 2.2: The tables list the image flux-density ratios obtained from previous observations of B0218+357. The dagger (†), corresponds to those interferometric configurations which included the observations of the Einstein ring as well. The second table shows the flux-densities of the subcomponents and the corresponding ratios of A1 to B1 and A2 to B2. (see text)

Author	Epoch	Interferometer	Frequency (GHz)	Beam (mas^2)	Flux density A (mJy)	Flux density B (mJy)	Flux-density ratio (A/B)
4	19 Jun. 1992	VLBI	1.7	5×5	445±23	170±9	2.62±0.19
1	9 Feb. 1990	VLA	4.84	400×400	880±80	370±20	2.38±0.25†
2	13 Jan. 1992	MERLIN	5	50×50	694±14	215±5	3.23±0.10†
2	27 Mar. 1992	MERLIN	5	50×50	736	220	3.35†
2	19 Nov. 1990	VLBI	5	5×5	660	210	3.14
2	26 Aug. 1991	MERLIN	5	50×50	728±15	245±5	2.97±0.09†
4	27 Mar. 1992	VLBI	5	1×1	515±26	196±10	2.62±0.19
1	9 Feb. 1990	VLA	8.4	220×220	807±40	271±15	2.98±0.22†
2	1 Aug. 1991	VLA	8.4	200×200	767	236	3.25†
6	Oct. 1996 to Jan.1997	VLA	8.4	200×200	–	–	3.57±0.01†
7	11 Nov. 2000	VLA	8.4	186×174	744	253	2.94†
7	11 Nov. 2000	VLBI	8.4	1.36×0.41	602	191	3.15
2	1 Aug. 1991	VLA	15	120×120	698	189	3.69†
6	Oct. 1996 to Jan.1997	VLA	15	120×120	–	–	3.73±0.01†
1	9 Feb. 1990	VLA	22.4	96×76	833±160	253±50	3.29±0.90†
2	1 Aug. 1991	VLA	22	96×76	654	180	3.63†

Author	Epoch	Interferometer	Frequency (GHz)	Beam (mas^2)	A (mJy)		B (mJy)		Ratio	
					A1	A2	B1	B2	A1/B1	A2/B2
4	9 May 1995	VLBI	8.4	1×1	472±24	218±11	139±7	63±3	3.39±0.24	3.46±0.24
5	9 May 1995	VLBI	8.4	–	544±25	223±5	171±5	60±3	3.18±0.17	3.72±0.20
7	11 Nov. 2000	VLBI	8.4	1.36×0.41	270±5	280±5	114±3	68±3	2.37±0.08	4.12±0.20
3	3 Oct. 1994	VLBA	15	0.5×0.5	477±7	291±5	132±3	80±3	3.61±0.10	3.64±0.15
4	17 Jul. 1995	VLBI	15	0.5×0.5	450±23	121±6	295±15	66±4	1.53±0.11	1.83±0.14
4	17 Jul. 1995	VLBI	22	0.3×0.3	328±17	100±5	140±7	81±4	2.34±0.17	2.43±0.17
4	17 Jul. 1995	VLBI	43	0.2×0.2	270±14	75±4	60±3	22±1	4.5±0.32	3.41±0.24

1 O'Dea et al. (1992) ; 2 Patnaik et al. (1993) ; 3 Patnaik et al. (1995)(corrected by factor 0.77) ; 4 Patnaik & Porcas (1999) ; 5 Kemball et al. (2001) ; 6 Biggs et al. (1999) ; 7 Biggs et al. (2003)

lensed images. The structure of a radio source is such that the surface brightness varies as a function of distance from the central engine, with the spectra of components at varying radii peaking at different frequencies (see Sect. 2.3.1), and the brightness profile of the integrated spectrum is no longer simple. This has a consequence that a 'feature' which is resolved in one image but unresolved in the other (due to different magnifications) may not correspond to the same component or a superposition of components in the background source.

Further, the surface-brightness sensitivity of an interferometer is a multi-valued function with the resolution as one of the parameters, which is directly proportional to the observing wavelength and inversely to the longest projected baseline[5]. Too high a resolution[6] results in a lower surface-brightness sensitivity and increases the noise per unit beam in the final (clean) maps of the images. Consequently, for certain interferometric configurations (or equivalently, *uv*–coverages) the deconvolution algorithms, which are used to obtain a model for the image brightness distribution (such as CLEAN, described in Sect. 3.5.1), cannot always register all the low surface-brightness emission in the images. This procedure is less difficult for relatively more magnified images. For B0218+357, image B is de-magnified, and the above effect might result in an underestimation of the image B flux density and a higher A to B ratio. This holds for source components partially or completely unresolved in one of the images.

If a part of the source with low and varying surface-brightness is partially resolved in both the images, the amount of undetected flux in either image is directly proportional to the area of the undetected parts of the component, which, *in general*, is proportional to the component magnification. Hence, the ratio of the undetected flux in the images is the ratio of their magnifications, thereby the ratio of their total flux-densities remains unaffected. But there could arise another complication related to the Fourier components of the brightness distribution that an interferometer actually measures and is sensitive to. It may be that the lowest spatial frequency which an interferometer is sensitive to, and which is determined by the shortest baseline, is not sufficient to detect the diffuse low surface-brightness the images are embedded in. The probability of missing out flux due to this is higher for relatively more magnified images. Thus, this will have an effect of lowering the A to B ratio.

The above considerations apply to circularly symmetric beams and with no directional preferences for flux detection. Assessing the effect of different magnifications in different images on the flux-density ratio becomes a more complicated issue, when the distortion of the images due to lensing is combined with the asymmetric beam of the interferometer.

- Contamination due to the Einstein ring: The Einstein ring emission is associated with that part of the radio jet which lies directly behind the astroid shaped radial caustic. Due to its steep spectral-index and diffuse emission, typical of radio jets, it is stronger at lower frequencies like 1.65 GHz to 5 GHz and is resolved. However, the ring is still detectable using the VLA (O'Dea et al. 1992; Patnaik et al. 1993), at higher frequencies like 15 GHz and 22 GHz. Fig. 2.11 shows the amorphous morphology of the Einstein ring

[5]The baseline is defined as the spacing between the antennas of an interferometer.

[6]In optics, the resolving power of an instrument is the inverse of its resolution. In radioastronomy, the term "high resolution" is equivalent to "high resolving power", however, in terms of the beam-size "high resolution" implies a small number.

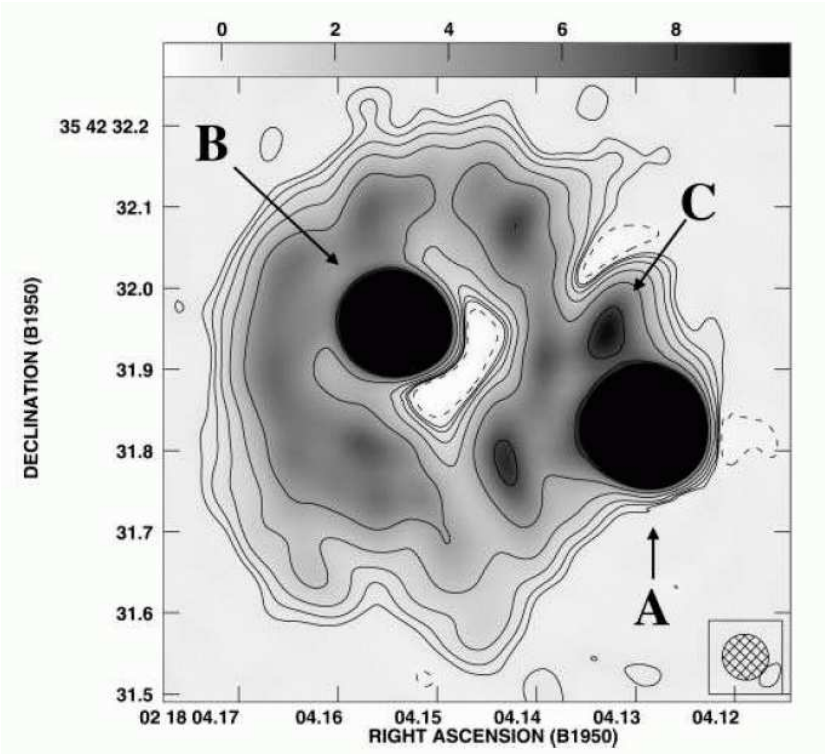

Figure 2.11: A MERLIN/VLA map at 5 GHz with a resolution of 58×56 mas^2 showing the amorphous morphology of the Einstein ring (Biggs et al. 2001). The grey-scale represents a brightness range of (-1 to 10) mJy beam^{-1}. The component C marked north-east of image A is the third brightest feature in the map, its origin and nature remains unidentified.

at 5 GHz using combined data from the VLA and MERLIN. It emphasizes the blending of emission from the images with that of the ring. It is exactly this blending and the fact that the ring diameter is small (equal to the image separation) that makes the flux-density estimation of individual components (A, B and the ring) questionable. With long baseline interferometry and resolution on the order of a few milliarcseconds (even up to 20 mas or 30 mas), the ring emission is completely resolved out and the danger of mixing of the emissions arising from different components is reduced.

Due to the above ambiguities, the numbers in Table 2.2 should be viewed with caution. The subcomponent ratios, A1/B1 and A2/B2, should in principle, be closer to the truth as they correspond to the same features of the background source. Unfortunately, the subcomponents are resolvable only at frequencies 8.4 GHz and higher, thereby providing an incomplete list of flux-density ratios. Moreover, different flux-density estimation techniques employed by different individuals and groups add to the scatter in the flux-ratios, especially as there are many methods for determining the total flux-density for extended regions of emission. The VLBI subcomponent ratios at 15 GHz, 22 GHz, 43 GHz (Patnaik & Porcas 1999) are suspicious and might have been affected by poor estimation techniques (Porcas, private communication). Similarly, the ratios obtained with the simultaneous detection of the Einstein ring should be regarded with caution. Despite the above reservations, there is a clear and evident change of image flux-density ratios from a value of around 2.6 at 1.7 GHz to 3.7 at 15 GHz.

2.7 Aim of the thesis

The goal of this thesis is to investigate the frequency dependence of the image A to image B flux-density ratio in the gravitational lens B0218+357. Although gravitational lens imaging of a point source is intrinsically achromatic, frequency dependent variations in the image flux-density ratio of an extended source are possible, provided its structure changes as a function of frequency and extends over regions of different relative magnifications. It seems quite possible that this occurs in B0218+357 since both conditions exist. Firstly, the small image separation leads to relatively large changes in the magnification across the extent of the images. For simple isothermal ellipsoid models of the lens potential, a shift of 15 mas in the position of a point-source image can produce a change in relative magnification from 4 to 2.5.

Secondly, the frequency-dependence of the B0218+357 image structure is strong, with previous VLBI observations showing a marked increase of the image sizes with decreasing frequency. Furthermore, it is common for the radio spectra of one-sided AGN jets such as that seen in B0218+357 to steepen with distance from the nucleus, providing a natural mechanism for producing a frequency-dependent position for the centroid of brightness distribution (see Sect. 2.3.1). The centroid position of the radio peak at the base of the jet is also expected to move away from the nucleus at lower frequencies–the "core-shift".

However, instrumental limitations prevent these effects from being seen easily. One is the change with frequency of the resolution available from VLBI observations. Another is the loss of absolute position information when phase self-calibration is used to make VLBI maps (chapter 3), which prevents robust registration of maps at different frequencies. frequency-dependent position shifts should, in general, show up as a change with frequency of the separation between different images. All the same, such differential shifts are hard to measure in some cases, especially when the shift is in the same direction in both images. Furthermore, any "feature" (e.g. the core) used to define the positions of the lensed images may, in fact, include different fractions of emission from the background source, since the images have different magnifications.

The main aim of this thesis is to investigate whether frequency dependent image positions, combined with a magnification gradient across the image plane, could give rise to the frequency dependence of the relative image-magnification. To establish an unambiguous registration of the radio structures of the lensed images at different frequencies, phase-referenced VLBI observations of the lens B0218+357 were conducted and are described in chapter 4. Although the core shifts observed in radio sources are relatively small (on the order of a milliarcsecond) the positions of the centroids of the image flux-density distributions may change with frequency by larger amounts, and these are more representative of the position of the emission. Therefore, it is important to quantify their changes with frequency when investigating the origin of the frequency-dependent image flux-density ratios.

Alternate mechanisms, such as perturbations due to small-scale mass-substructure, free-free absorption and refractive scattering, are considered in chapters 6 and 7.

3 VLBI and the technique of phase-referencing

The technique of Very Long Baseline Interferometry (VLBI) can achieve high angular resolution (at the milliarcsecond level) and has earned itself a special status in the field of gravitational lensing (Biggs 2005). The JVAS/CLASS (Cosmic Lens All-Sky Survey, Myers et al. 2003; Browne et al. 2003) survey, which has been the most extensive lens survey to date, discovered a total of 22 GL systems using the VLA ($0.2''$ resolution), wherein the final confirmations could be made only using the longer-baseline MERLIN array and very long baseline interferometers such as the VLBA.

Apart from providing confirmations of lens candidates by revealing similar morphologies of the lensed images of the same background object, VLBI observations yield a multitude of other lens observables. High-redshift radio sources often show variability in emission and structure, and systematic monitoring of lensed images of such background sources can provide time-delay measurements (Narasimha 2004; Barkana 1997; Campbell et al. 1995). Observations of lensed image-structures on varying scales provide constraints for lens modelling which together with the time-delay measurements render estimates for the Hubble constant (e.g. Koopmans et al. 2000; Keeton & Kochanek 1997). Details of multiply lensed radio jets, when oriented in the radial direction relative to the lens centre, provide stringent constraints on the mass-radius profile (Wucknitz et al. 2004) and indicate whether the lens galaxies have an isothermal profile or shallower, such as the NFW profile (Navarro et al. 1996).

Lastly, multi-frequency and high-resolution observations of a lens system can be used for studying the ISM of the lens galaxy. This can be achieved by means of comparing the observed properties of the lensed images to those which are predicted from the theory and investigating various propagation effects which are likely to occur along the lines of sight to the images (Winn et al. 2003; Marlow et al. 1999b, see also chapter 7). This allows the intrinsic properties of the background lensed object to be separated from extrinsic effects such as scattering, free-free absorption, and Faraday rotation. Such studies can also be used to test the CDM predictions on the existence of compact galactic satellites or substructures in the mass range $10^5\ M_\odot$ to $10^7\ M_\odot$ in the lens galaxy (Metcalf 2002, see also chapter 6).

3.1 The origin of VLBI

The initial need to use interferometry in radioastronomy, using spaced telescopes with physical connections, arose due to the poor resolution in comparison with that at optical wavebands. Using Rayleigh's criterion where the theoretical upper limit to the resolving power is set by the diffraction pattern, the minimum angular resolution for a telescope is $\approx \lambda/D$, where λ is the observing wavelength and D is the diameter of the telescope aperture. Therefore, in going from the optical to the radio regimes the resolving power or the resolution decreases by a factor of $\sim 10^3$ to 10^6. But the ground-based optical resolution until recently was limited to

only about an arcsecond due to scintillation caused by atmospheric turbulence[1] (on time scales of milliseconds, and spatial scales smaller than the antenna). As a result, radio observations with telescope spacings of a few tens of kilometers can bring the radio and optical resolutions on a par. But soon after the completion of the third and the fourth Cambridge catalogues (3C and 4C, respectively), and other large surveys of radio objects in the late sixties and seventies, there arose a further need to extend the telescope spacings to scales of continental separations. It became desirable to pin-point the position of these radio sources with higher precision, to resolve ambiguities due to source confusion, and to examine their structure on sub arcsecond scales.

The first prototype of a radio interferometer, based on the same principles as the Michelson interferometer, was constructed in 1946 by Ryle and Vonberg using an array of dipole antennas at 175 MHz. Over the next decades, several radio interferometers came into existence, such as the Westerbork synthesis radio telescope in the Netherlands, the Very Large Array (VLA) in New Mexico, the Five-Kilometer radio telescope at Cambridge, England etc. However, all shared a common aspect in that the source signals at different telescopes were correlated in real-time using coaxial cables, waveguides or some other form of radio transmission lines. These were the conventional type of arrays and the technique was called connected-element or linked-element interferometry. VLBI, which was introduced in the late 60's (Cohen et al. 1968), is different as, in this technique, the signals at individual telescopes are independently recorded on either magnetic tapes (or now hard disc drives) and correlated with each other at a later time. This leads to more than two orders of magnitude increase in the resolution as the restriction of the telescopes being physically linked to each other is lifted. Using high-precision local oscillators, the coherence of the signals can be preserved which allows successful detection of interference fringes. The data, after being recorded at different sites, are shipped to a central unit called the correlator where the data are correlated and further processed. A major drawback of using the VLBI technique is that it usually includes a long waiting period between the times when the data are actually recorded and when they are correlated. In this regard, a recent development is the initiation of several e-VLBI projects which attempt to link the telescopes electronically in real-time.

The VLBI technique has been the state of the art in the mapping of high-resolution radio sources for nearly four decades now. The theory involves complexities at every stage, such as choosing an optimum configuration of the interferometer array, having an appropriate observing schedule to fulfill the science goals, the correct encoding and decoding of the signal to and from the mode of storage used, detection of fringes, and finally (and perhaps most importantly) the reduction and analysis of the data. For a step-by-step review of the details of this process, the reader is referred to texts of radio-interferometry such as Felli & Spencer (1989), Taylor et al. (1999) or Thompson et al. (2001). In this chapter, the fundamental elements of radio interferometry relevant to this thesis (Sect. 3.2) and the calibration techniques (Sections 3.3 and 3.4) that were used for the data reduction of B0218+357, described in the next chapter, will be outlined.

[1] With the advent of the techniques of Adaptive Optics (AO) and the Hubble Space Telescope, the optical resolution has now become comparable to the diffraction limit of the telescope.

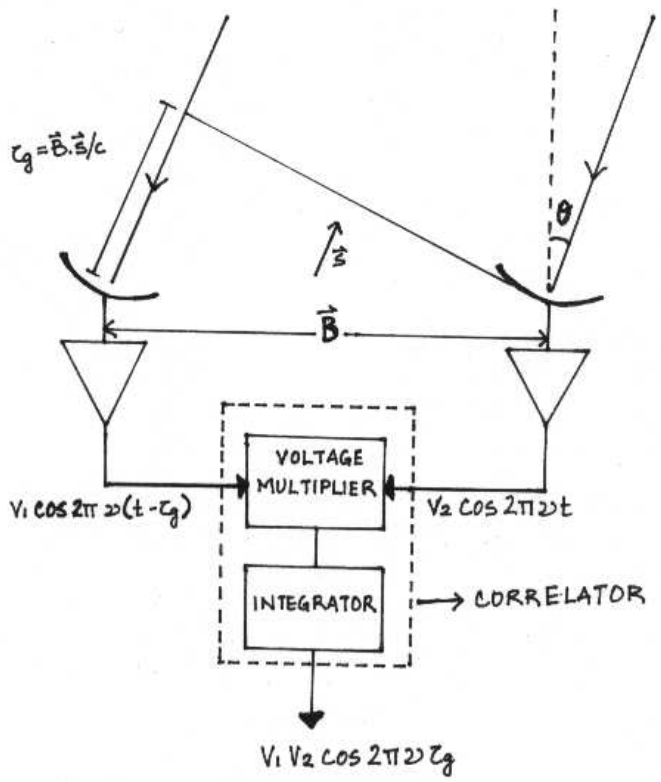

Figure 3.1: Block diagram of a two-element interferometer with baseline B (adapted from Thompson 1999).

3.2 Basic principles

3.2.1 Image synthesis

Fig. 3.1 depicts a two-element interferometer, where B is the distance between the antennas or the baseline. Since the source is at a distance much greater than the separation of the antennas, the rays arriving at the different antenna sites are parallel to each other but arrive at one antenna a time τ_g before the other. τ_g is the geometrical time-delay equal to $\vec{B}.\vec{s}/c$, where $\vec{s}$ is the source direction. If θ is the zenith angle, then $\tau_g = B\sin\theta/c$. Thereafter, the signals go through amplifiers which have identical bandpass characteristics and a finite bandwidth $\Delta\nu$ (shown as inverted triangles in Fig. 3.1). To compensate for the geometric time-delay, an instrumental time-delay τ_i is inserted to one of the arms calculated for a nominal source position, θ_0, called the phase-center. However, τ_g changes with time as the Earth rotates (due to the changing θ) and in VLBI the frequency of the fringe oscillations can exceed 100 kHz. Therefore, there is a device called the 'tracking delay', which tracks the source as it moves through the interference fringes. However, since the incoming radio frequency signal is usually mixed down to a lower Intermediate-Frequency (IF) before operation of the tracking delay, there is a further correction applied, called 'fringe rotation', to compensate for the fact that τ_i is not inserted at the received signal frequency. The signal voltages are then multiplied and integrated for time $2T$, such that the output is

$$r(\tau) \;=\; \frac{1}{2T}\int_{-T}^{T} V_1(t)\, V_2(t-\tau)\, dt\,, \tag{3.1}$$

where $\tau = \tau_g - \tau_i$. Thus, such an instrument measures the cross-correlation of the electric field measured at the two antennas and the electronic unit that performs multiplication and integration is called a correlator. The inserted time-delay should be accurate to within the inverse of the bandwidth, or else due to different phase-delays ($\propto B/\lambda$) suffered by the individual monochromatic components within the bandwidth, the resultant signal is caused to become incoherent. The typical integration time is on the order of a few seconds, thus $T \gg \Delta\nu^{-1}$. Using the Wiener-Khinchin relation for a continuous random process, $r(\tau) \rightleftharpoons |H(\nu)|^2$, according to which the Fourier transform of the auto-correlation function is equal to the square of the frequency spectrum, also known as the amplitude or voltage response $H(\nu)$,

$$r(\tau) \;=\; \exp\left[-2\left(\frac{\pi B\sigma}{c}\sin\theta\right)^2\right]\cos\left(\frac{2\pi\nu_0 B}{c}\sin\theta\right)$$

or

$$r(\tau) \;=\; \frac{\sin(\pi\tau B)}{\pi\tau B}\cos\left(\frac{2\pi\nu_0 B}{c}\sin\theta\right), \tag{3.2}$$

where Gaussian and rectangular amplifier passbands centered at ν_0 are assumed, respectively.

The correlator response for a given baseline (at an instant of time) can also be visualized as one Fourier component of the source brightness distribution given by,

$$V(u,v,w) \;=\; \int_{-\infty}^{\infty}\int_{-\infty}^{\infty} A_N(x,y)\frac{I(x,y)}{\sqrt{1-x^2-y^2}}\, e^{2\pi i[ux+vy+w(\sqrt{1-x^2-y^2}-1)]}\, dx\, dy, \tag{3.3}$$

where A_N is the geometric mean of the beam patterns of the two antennas, I is the source brightness distribution and V is the visibility. (u,v,w) are the baseline components in wavelength where u and v are in a plane perpendicular to the direction of the phase-centre with u toward the east and v toward the north, and w is in the direction of the phase-centre. x and y are the coordinates in the sky plane, and are the Fourier conjugates of u and v, with the origin at the field centre and x pointing to the east. Assuming that the synthesized field is small $(x^2+y^2) \ll 1$, so that w can be neglected, leads to the following simplification,

$$V(u,v) \;=\; \int_{-\infty}^{\infty}\int_{-\infty}^{\infty} A_N(x,y)I(x,y)\, e^{2\pi i(ux+vy)}\, dx\, dy\,. \tag{3.4}$$

The source brightness distribution is obtained from inverting the above expression,

$$A_N(x,y)I(x,y) \;=\; \int_{-\infty}^{\infty}\int_{-\infty}^{\infty} V(u,v)\, e^{-2\pi i(ux+vy)}\, du\, dv\,. \tag{3.5}$$

In other words, the image of an observed source in synthesized using the observed Fourier components of its brightness distribution.

3.2.2 Field of view

The foregoing analysis is based on two assumptions that limit the applicability of the results. Firstly, it is assumed that the source is distant enough that the wavefront can be treated as planar over the extent of the entire interferometer. If the source is not sufficiently far away, then the rays will make different angles at different antennas sites. The lower limit on the distance to the source is set by the minimum phase variation that can be measured. For a given source at distance z in the direction normal to the baseline of length B, and a phase-variation sensitivity of the instrument, $\Delta\phi$, this limit is derived as

$$\delta\tau_g \simeq \frac{B^2}{2z} \ll \frac{\Delta\phi}{2\pi\nu},$$

or

$$z \gg \frac{\pi B^2}{\lambda\Delta\phi},$$

where $\delta\tau_g$ is the change in the geometrical time-delay due to non-planarity of the wavefront. For $\Delta\phi$ on the order of a few degrees (comparable to current instrumental capabilities), this condition can be safely assumed to be true for sources external to the solar system.

Secondly, the neglecting of the w–term sets a limit on the maximum field of view, θ_f. The synthesized field is related to the field of view by $(x^2 + y^2) = (\theta_f/2)^2$. For baselines other than on an east-west line, w for sources at low elevations can be as much as the maximum baseline and therefore inversely proportional to the full width at half maximum (FWHM) of the synthesized beam, θ_b^{-1}. The phase error due to ignoring w is

$$\delta\phi \simeq \pi(x^2 + y^2)w \;=\; \frac{\pi}{\theta_b}\left(\frac{\theta_f}{2}\right)^2.$$

Thus,

$$\theta_f \ll \left(\frac{4\theta_b}{\pi}\Delta\phi\right)^{\frac{1}{2}}.$$

The synthesized beam for a typical VLBI observation at 5 GHz is ~ 2 mas. Restricting the phase error to be less than 0.1 radians limits the field of view to be less than ~ 7 arcsecond.

Apart from the above limitations, other factors that restrict the field of view are the integration time and the delay response. This can be understood by means of Eq. 3.2. Whereas averaging in time and frequency is advantageous (Sect. 3.3.3), it results in a smearing in the map which is proportional to the distance from the phase-centre. Depending upon the time interval and the frequency interval over which the data is averaged, the effect of bandwidth-smearing and time-smearing can dominate over the effect from neglecting of the w–term.

This is a serious drawback in VLBI mapping of gravitational lenses. The typical angular separation between lensed images in galactic GL systems is $0.5''$ to $2''$, which gives rise to a need for having a relatively wide field of view. The nominal field of view due to averaging the data in frequency over a width $\Delta\nu$ is $\sim \theta_b \times (\nu/\Delta\nu)$, where ν is the observing frequency. As an example, averaging the data over 8 MHz in frequency at an observing frequency of 15 GHz (with the synthesized beam $\theta_b \approx 0.5$ mas) limits the field of view to about an arcsecond. The image separation in the lens system B0218+357 is the smallest amongst the known galactic type lenses ~ 330 mas, and averaging the data over a 8 MHz frequency channel does not cause a severe problem. On the contrary, for wide-field GL systems such

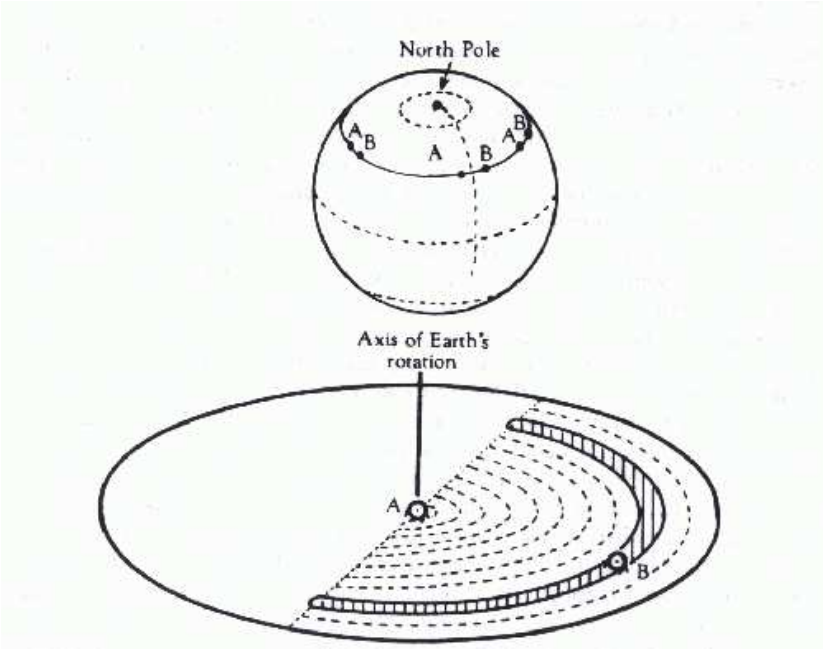

Figure 3.2: Earth rotation used to advantage in interferometry (Ryle 1962). This figure shows two antennas A and B spaced on an east-west line tracking a high-declination source for 12 hr at several configurations obtained by varying their separation.

as MG2016+112 (Lawrence et al. 1984), where the maximum image separation is over $3.5''$, frequency-averaging under the same conditions must be restricted to within 1 MHz. However, averaging the data over entire bandwidths (typically 32 MHz/64 MHz in width) can cause a substantial bandwidth-smearing even for systems such as B0218+357.

3.2.3 Earth's rotation

One way to understand the working of an interferometer is shown in Fig. 3.2. Assume a pair of antennas A and B, a certain distance apart and observing a high-declination source. At any given instant of time, the antenna baseline can be projected onto a plane perpendicular to the source direction (or the centre of the field of view), called the *uv*–plane. The baseline vector can be decomposed into two orthogonal components, u and v, as introduced in Sect. 3.2.1, the values of which depend upon the latitude, elevation and azimuth of the baseline, the hour angle and the declination of the source. The locus of u and v as a function of the hour angle traces an ellipse centered on the v axis. Since the quality of an image depends upon the amount of *uv*–data, the goal is to maximize the *uv*–coverage. This is achieved using the Earth rotation as shown in the figure. From varying the antenna separation (not possible with VLBI, however) and carrying out 12 hr observations at every configuration, the 'telescope aperture' or the *uv*–plane is encompassed more and more.

Shown in Fig. 3.3 are the *uv*–visibilities of B0218+357 at 5 GHz recorded using the VLBA and the Effelsberg telescope. The (u,v) coverages in the left and the right panels are obtained from data recorded over 2 s and the entire observation run, respectively. The effect of Earth rotation during the observation period on the coverage is seen clearly as more and more regions in the *uv* plane get filled with the *uv* data. As seen by the source, the array of fixed

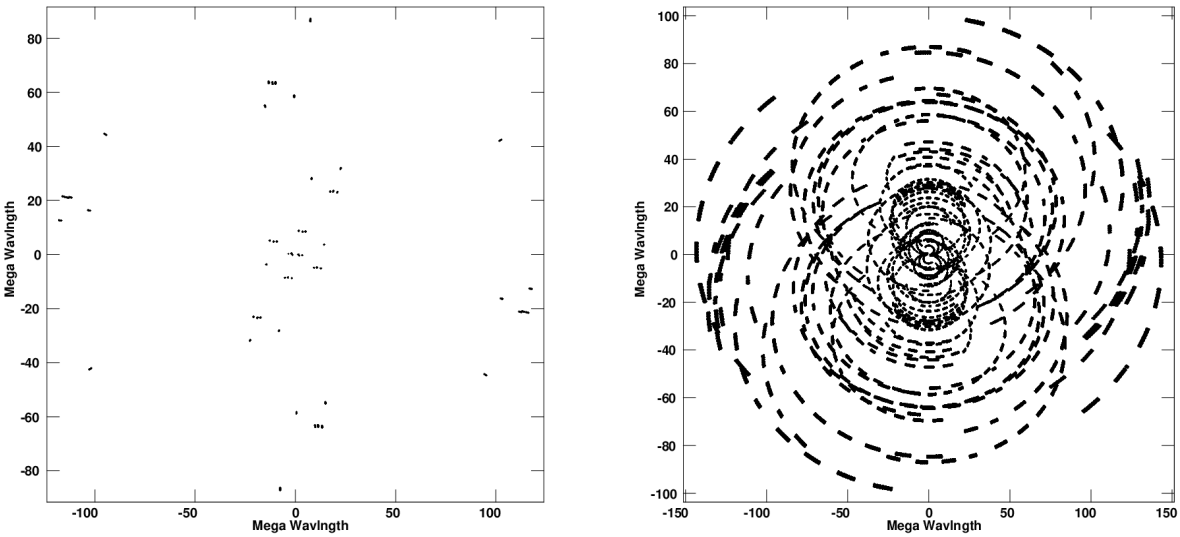

Figure 3.3: The effect of Earth rotation in filling of the *uv* plane. Shown are the (u,v) coverages provided with the VLBA and the Effelsberg telescope. The observations were of B0218+357 at a wavelength of 6 cm. The averaging time of the data is 2 s. Plotted in the left panel are data points spanning only 2 s in time and plotted in the right panel are data points from the entire observation run spanning 13 hrs to 14 hrs.

antennas seems to sweep through space as the Earth rotates, leading to the creation of an artificial aperture.

3.3 Data calibration

The output of the correlator (Eq. 3.1) is a complex function, called a visibility. For a given baseline formed between the i^{th} and j^{th} antennas ($i-j$ baseline), at time t and observing frequency ν, the visibility is described as

$$V_{ij} \;=\; S_{ij}\, e^{i\theta_{ij}}, \tag{3.6}$$

which comprises two factors of importance, the visibility amplitude, S_{ij}, and the visibility phase, θ_{ij}. The complex term arises due to asymmetries in the source brightness distribution; the correlator output for a source symmetric about its phase-centre under ideal conditions (in the absence of phase errors) will be devoid of the phase-term. In reality, the observed and true visibilities are different from each other for a multitude of reasons and related as

$$\tilde{V}_{ij}(t,\nu) \;=\; G_i(t,\nu)G_j^*(t,\nu)V_{ij}(t,\nu) + \epsilon_{ij}(t), \tag{3.7}$$

where $\tilde{V}_{ij}(t,\nu)$ and $V_{ij}(t,\nu)$ are the observed and true visibilities, respectively, and ϵ_{ij} is the random error due to receiver noise (see Appendix D.2). G_i and G_j are the antenna dependent complex gains defined as $G_i(t,\nu) = a_i(t,\nu)e^{i\phi_i(t,\nu)}$, where a_i is an antenna-based amplitude correction factor. ϕ_i is an antenna-based phase error which arises due to imprecise clocks, incorrect models for the source and interferometry geometry, and propagation effects due to the atmosphere (ionospheric and tropospheric, see Appendix E). Here, any baseline

dependent errors are ignored as they are usually negligible. Substituting Eq. 3.6 into Eq. 3.7 and putting aside the error term ϵ_{ij} for the time being,

$$\tilde{S}_{ij}\, e^{i\tilde{\theta}_{ij}} = a_i\, a_j\, S_{ij}\, e^{i(\phi_i - \phi_j + \theta_{ij})}. \tag{3.8}$$

The aim of calibration is to determine the contaminating phase errors, ϕ_i's, and the amplitude gains, a_i's, that hinder estimation of the true source brightness distribution.

3.3.1 Closure phase and amplitude

A lead to the solution to the problem stated above was presented by Jennison (1958), whereby he described a method of determining the interferometric phases and amplitudes using groups of three antennas. The simple idea consists of summing the observed visibility phases on three baselines formed by a closed loop of three antennas. If the antennas are labeled, i j and k, the sum of the visibility phases from Eq. 3.8 is

$$C_{ijk} \;=\; \tilde{\theta}_{ij} + \tilde{\theta}_{jk} + \tilde{\theta}_{ki} \;=\; (\phi_i - \phi_j + \theta_{ij}) + (\phi_j - \phi_k + \theta_{jk}) + (\phi_k - \phi_i + \theta_{ki}) \;=\; \theta_{ij} + \theta_{jk} + \theta_{ki}\,. \tag{3.9}$$

Thus, the sum of their observed phases, C_{ijk}, is free from antenna related phase-errors, and only depends upon the intrinsic source structure. Similarly, the closure amplitude (Twiss et al. 1960) is defined as the following which needs a minimum of four antennas in the loop,

$$A_{ijkl} \;=\; \frac{|\tilde{S}_{ij}||\tilde{S}_{kl}|}{|\tilde{S}_{ik}||\tilde{S}_{jl}|} \;=\; \frac{S_{ij}S_{kl}}{S_{ik}S_{jl}}. \tag{3.10}$$

Thus, the closure amplitudes are free from antenna amplitude-miscalibrations.

3.3.2 Self-calibration

The visibility amplitudes and phases are corrupted by unknown errors. These errors result in incoherent scattering of the emission and also introduce artifacts in the maps. This is one of the many well-known 'imaging problems'. Given N antennas, the number of observed, but erroneous, visibilities is equal to the number of baselines, $N_b = N(N-1)/2$. However, the number of true observables, the closure phases, is $N_c = (N-1)(N-2)/2$. Since the absolute value of an antenna phase is meaningless, the above calculations have been simplified by assuming that the phase-error of one of the antennas in the array (reference antenna) is zero. The phase-errors of the remaining antennas are, subsequently, determined with respect to the reference antenna. Thus, the number of unknown visibilities (N_b) exceeds the number of known quantities (N_c) by $(N-1)$ or in other words there is missing information on $(N-1)$ baselines and the true visibilities cannot be determined uniquely. The way to get around the problem is to assume a 'trial' model (constructed from making plausible assumptions on the source structure) for the source brightness distribution. The complex antenna gains are assumed as free parameters and the model visibilities are optimized by minimizing,

$$S = \sum w_{ij} \left| \tilde{S}_{ij} - G_i G_j^*\, \hat{S}_{ij} \right|^2, \tag{3.11}$$

where $\hat{S}_{ij}$ are the trial visibilities, $\tilde{S}_{ij}$ are the observed visibilities and w_{ij} are the weights given to the visibilities, which in the simplest case are reciprocals of the variance of the noise

attributed to the data points. This method of deriving a source model is called self-calibration, also known as Hybrid Mapping. The efficacy of this method in providing reliable modelled visibilities increases as the number of antennas in the array becomes larger. This can be visualized by considering the ratio of the number of known parameters (closure phases) to the total number of visibilities, $(N-2)/N$. For an array with 11 elements (as is the case with the observations of B0218+357 described in chapter 4), this ratio is ~ 82 %.

3.3.3 Fringe-fitting

The visibilities from the correlator are usually time and frequency averaged. But due to limited coherence in the data and to preserve a wide field of view, the averaging time is restricted to within a few seconds and frequency interval to within a megahertz. Averaging of data is essential for two reasons. Firstly, to have a manageable size of data file and secondly, to increase the the signal-to-noise ratio (SNR). The SNR without averaging the data is not sufficiently high for the detection of weak sources, and hence prohibits application of the self-calibration technique to get a reliable source brightness distribution.

The coherence is limited due to various factors, such as imperfect delay and fringe-rate compensations, which give rise to phase-errors but which in addition introduce phase slopes in time and frequency domains across the bandwidth. Examination of the phase part of Eq. 3.8 gives,

$$e^{i\tilde{\theta}_{ij}}(t,\nu) \;=\; e^{i[\phi_i(t_0,\nu_0)-\phi_j(t_0,\nu_0)+\theta_{ij}(t,\nu)+\Delta r_{ij}(t-t_0)+\Delta\tau_{ij}(\nu-\nu_0)]}, \tag{3.12}$$

where $\Delta r_{ij} = (r_i - r_j)$ and $\Delta\tau_{ij} = (\tau_i - \tau_j)$ and

$$r_i = \frac{d\phi_i(t_0,\nu_0)}{dt}$$

$$\tau_i = \frac{d\phi_i(t_0,\nu_0)}{d\nu}$$

are the phase-rate and phase-delay respectively. The phase slopes are assumed to be constant for a wider range of time-interval and frequency range, so that the delay and rate offsets need to be removed only once to allow integration of the visibilities for a few minutes and over the entire bandwidth. The offsets are removed by performing a two-dimensional search in the residual rate and delay domain which is the Fourier transform of the time and frequency domain. The rate and delay solutions are found for each antenna separately and this process is called global fringe-fitting. As in the self-calibration scheme, there is a model for the source brightness distribution assumed (a point source in most cases) and Eq. 3.11 is used to evaluate the delay and rate residuals, and eventually the antenna gains. It is to be noted that both self-calibration and fringe-fitting embody the observed closure phases implicitly by assuming that the visibility phase-errors (hence the rates and delays too) are antenna-dependent, permitting the antenna-gains to be treated as antenna based free parameters.

3.3.4 Amplitude calibration

The true visibility amplitudes are estimated by equating the amplitude factors appearing in Eq. 3.8,

$$S_{ij} \;=\; \frac{\tilde{S}_{ij}}{a_i a_j}, \tag{3.13}$$

where S_{ij} is the true correlated flux-density of the source and $\tilde{S}_{ij}$ is the measured visibility and, in reality, is just a raw correlation coefficient from the correlator. It is instructive to write the product of the antenna gains in measurable quantities,

$$\begin{aligned} a_i a_j &= \frac{1}{b}\sqrt{\frac{K_i K_j}{t_{sys_i} t_{sys_j}}}, \\ S_{ij} &= b\tilde{S}_{ij}\sqrt{\frac{t_{sys_i} t_{sys_j}}{K_i K_j}}, \end{aligned} \tag{3.14}$$

where K_i and K_j are the sensitivities, t_{sys_i} and t_{sys_j} are the on-source system temperatures of antennas i and j, respectively, and b is the digital processing factor. The antenna sensitivity, $K = \eta A/(2k) = T_a/S$, depends upon the antenna aperture efficiency (η) and the true geometric area of the antenna (A). k is the Boltzmann constant, T_a is the antenna temperature and S is the source flux-density (see Eq. D.11). The effective collecting area (ηA) is a function of the elevation angle, hence the antenna sensitivity or the gain curve changes as the antenna tracks the source. It can be determined through regular observations of a strong calibrator, for which $K_i = T_{a_i}/S_i$ is obtainable, and regular system temperature measurements, typically once every source scan. The true correlated flux-density can then be recovered.

3.4 Phase-referencing

After the data are correlated, they are subjected to numerous calibration procedures, the goal of most of which is to improve the coherence in the data to allow time and frequency averaging for a high signal-to-noise ratio. For some experiments, especially those related to geodesy or astrometry, it is the errors eliminated by the above procedures that are the desired quantities. As mentioned in Sect. 2.7, in the investigation of the image flux-density ratio anomaly seen in B0218+357, the physical quantities of interest are the relative image-positions at different frequencies, so that their frequency dependence can be measured.

VLBI observations suffer from the corrupting influence of the troposphere, ionosphere and instrumental uncertainties on the interferometer visibility phase. For observations of strong sources, the technique of phase self-calibration (Sect. 3.3.2) can be used by determining the corrupting phases (the complex antenna gains) which are treated as antenna-based free parameters. However, this is only possible if the signal-to-noise ratio is high when averaging over periods for which these parameters are constant. For weak sources, this is usually not the case; fringe-fitting fails to provide solutions for the phase-delays and the phase-rates. Furthermore, the geometrical phases which contain information regarding the source position relative to the antennas, are absorbed in these parameters, resulting in the loss of any information on the source position in the sky.

To overcome these hurdles, the technique of phase-referencing can be used. In this process, an attempt is made to determine the corrupting phase errors indirectly, using observations of a reference source. This source should ideally be point-like, sufficiently strong that phase self-calibration is possible, and close enough to the target source for their tropospheric and ionospheric phase corruptions to be similar. Observations of the target and reference sources are alternated frequently and the phase errors determined from the reference are then interpolated to times at which the (usually weaker) target source is observed. Under the assumption of equal tropospheric, ionospheric and instrumental phase errors for the target and reference

sources, these errors can be subtracted from the target, allowing mapping of the target and determination of its position with respect to the reference. When the technique was first devised, due to the role played by the reference source in determination of the phases of the target source, the former came to be known as a 'phase-reference'. But there are experiments, wherein the phases of the target source are transferred to obtain a map of the reference source, and the latter only serves to provide a positional reference of the target. This process is called 'inverse phase-referencing'. The reference source, in this case, is appropriately called a 'position-reference'. It is this technique which is used for B0218+357, as it is strong enough to use self-calibration.

Using subscripts, 'T' and 'P', for the target source and the phase (or position) reference respectively, the observed and true visibility phases on baseline $i - j$ are related by the following equations,

$$\theta_{\rm T}^{\rm obs} - \theta_{\rm T}^{\rm true} = \phi_{\rm T}\,, \tag{3.15}$$

$$\theta_{\rm P}^{\rm obs} - \theta_{\rm P}^{\rm true} = \phi_{\rm P}\,, \tag{3.16}$$

where $\phi = \phi_i - \phi_j$ is the visibility phase-error on the given baseline and contains four independent sources of errors. Thus,

$$\phi = \phi^{\rm inst} + \phi^{\rm ion} + \phi^{\rm trop} + \phi^{\rm geo}\,, \tag{3.17}$$

where the superscripts 'inst', 'ion', 'trop' indicate instrumental, ionospheric and tropospheric phase-errors, which are assumed to be similar for the target and the reference sources. The superscript 'geo' indicates an astrometric phase-error in the position of either the source or the reference or both. Therefore, subtracting Eq. 3.16 from Eq. 3.15 results in

$$\theta_{\rm T}^{\rm obs} - \theta_{\rm T}^{\rm true} = (\theta_{\rm P}^{\rm obs} - \theta_{\rm P}^{\rm true}) + (\phi_{\rm T} - \phi_{\rm P})^{\rm geo}\,, \tag{3.18}$$

as the first three terms on the right hand side of Eq. 3.17 are canceled. The structure of either the reference source, $\theta_{\rm P}^{\rm true}$ (phase-referencing) or the target source, $\theta_{\rm T}^{\rm true}$ (inverse phase-referencing) is pre-determined from the self-calibration routine. Hence, what remains is the intrinsic structure of the other, and the last term represents the difference between the position errors of the target source and the reference; it is constant with frequency only if both sources have achromatic positions.

3.5 Imaging

Assuming A_N, the geometric mean of the antenna beam-patterns, to be constant over the field of the source[2], Eq. 3.3 can be reduced to,

$$I(x,y) \;=\; \int_{-\infty}^{\infty}\int_{-\infty}^{\infty} V(u,v)\, e^{-2\pi i(ux+vy)}\, du\, dv\,. \tag{3.19}$$

where the visibility function and the source brightness distribution are Fourier conjugates of each other, $V(u,v) \rightleftharpoons I(x,y)$, and the integral is taken over the entire uv–plane. In reality, the measurements exist only at a discrete set of points in the $uv-$plane, (u_k,v_k), $k = 1, 2 \ldots, M$,

[2]In VLBI this assumption is reasonably good since the source size is very small in comparison with the primary beam of the individual telescopes.

which is governed by the interferometer-geometry. Therefore, in the end what results is a dirty representation of the true source brightness distribution,

$$I^{\rm d}(x,y) \;=\; \int_{-\infty}^{\infty}\int_{-\infty}^{\infty} \tilde{V}(u,v)\, e^{-2\pi i(ux+vy)}\, du\, dv\,, \tag{3.20}$$

where $I^{\rm d}(x,y)$ is called the *dirty map*. The observed visibility function can also be written as

$$\tilde{V}(u,v) \;=\; W(u,v)[\hat{V}(u,v) + \epsilon(u,v)]\,, \tag{3.21}$$

where

$$\hat{V}(u,v) = \sum_{m,n=1}^{N} \hat{I}(m\Delta x, n\Delta y)\, e^{2\pi i(mu\Delta x + nv\Delta y)} \tag{3.22}$$

is the visibility function of a discrete model of the source brightness distribution, $\hat{I}$ (true or which is capable of reproducing the observed visibilities). Thus $\hat{V}(u,v) \rightleftharpoons \hat{I}(x,y)$. $\epsilon(u,v)$ is the thermal noise from the receiver amplifier. Also,

$$W(u,v) = \sum_{k=1}^{M} w_k\, \delta(u-u_k, v-v_k) \tag{3.23}$$

is the weighted sampling function described by the measured points in the visibility plane. The Fourier transform of the weighted sampling function, $W(u,v) \rightleftharpoons B(x,y)$, is the *dirty beam (or synthesized beam)*,

$$B(x,y) = \sum_{k=1}^{M} W(u_k,v_k)\, e^{-2\pi i(xu_k+yv_k)}\,. \tag{3.24}$$

Applying the convolution theorem to Eq. 3.21, the Fourier transform (FT) of the observed visibility function $V(u,v)$ is the convolution of the FT of the dirty beam with the sum of the FT of the true source brightness and the FT of the noise,

$$I^d(x,y) = B(x,y) * [\hat{I}(x,y) + E(x,y)], \tag{3.25}$$

where $E(x,y)$ is the noise in the image.

The implementation of Eq. 3.22 can be carried out by either using the method of direct Fourier transform (DFT) or the method of fast Fourier transform (FFT). In both methods, $\hat{V}(u,v)$ and $\hat{I}(x,y)$ are represented on rectangular grids with data sampled at uniform increments. But since the observed visibilities seldom lie on grid points, some form of interpolation technique, such as using convolution functions, has to be employed. While the number of operations required by DFT is $O(N^4)$, for FFT it is reduced to $N^2\log_2(N)$ where N is a power-of-two.

The coefficient appearing in the weighting sampling function in Eq. 3.23 for the (u_k, v_k) visibility point is more generally written as, $w_k = R_k T_k D_k$, (see Taylor et al. 1999). Here, R_k is the data weight equal to the inverse variance of the noise that is defined by virtue of the integration time used to obtain the corresponding data point, the system temperatures and gains of the antennas and the sample bandwidth. T_k is the tapering function, usually Gaussian, used to downweight the high spatial-frequency visibilities, and thus to suppress

the sidelobes of the dirty beam. D_k is the density weighting function used to attain an optimal balance between high and low spatial frequencies depending upon the goal of the experiment. The distribution of the data visibilities in the uv–plane is usually such that the interior region corresponding to the short baselines has a higher number density than the outer regions corresponding to the long baselines. If $D_k = 1$, it is called the *natural weighting* scheme which results in a large beamwidth and is used to optimize the signal-to-noise ratio. Alternatively, if $D_k = 1/N_k$, where N_k is the number of the visibilities contributing to the $k^{\rm th}$ cell of the grid, it is called the *uniform weighting* scheme as a unit weight ($D_k \times N_k = 1$) is assigned to each gridcell. This scenario is equivalent to the downweighting of small spatial-frequencies resulting in a higher-resolution image.

The problem in the imaging process can be realized by inspection of Eq. 3.25, where the dirty beam $B(x, y)$ is obtained from the Fourier transformation of the sampling function (Eq. 3.24) which does not cover the uv–plane in its entirety. The sampling function has a finite extent, which causes $B(x, y)$ to have a finite width (ideally it would be a delta function) and to have negative features. Furthermore, the sampling function has zeroes (or holes) which forbids a unique solution for the source brightness distribution. If the visibilities are represented by zeros at those points in the uv–plane where there are no measurements, the resultant source brightness distribution in the image plane is the dirty image, also known as the *principal solution*, which is confused by the effects of extended, negative sidelobes. To this solution, there could be added any visibility distribution with arbitrary values at the non-measured visibility points, giving rise to an infinite number of distributions in the image plane which still comply with the observed visibilities. The technique employed to determine the optimal solution is the one that is able to generate new spatial frequencies based on *a priori* information on the source brightness distribution and improve the quality of the map, thereby non-linear in nature. There are two such algorithms, CLEAN and MEM (Maximum Entropy Method), of which the first method has been used to obtain the maps of the lensed images in B0218+357 and is, therefore, discussed in further detail in the following subsection.

3.5.1 CLEAN

This algorithm was devised by Högbom (1974) and works in the image plane (xy–plane). The philosophy behind its working is the following: convolution of a point-source with the dirty beam results in the dirty beam itself. Thus, on subtracting the dirty beam from the point of maximum deflection, in a map of a point source, there should only be noise left in the residual map. The method comprises the following steps. First, the image plane is searched for the pixel with peak intensity. The peak intensity is compared with the average absolute value and if the difference is greater than a user-specified threshold, the algorithm proceeds to the next step. Second, the dirty beam with a modified peak strength, γI_0, where γ is the *loop gain*, is centred at the position of the peak and subtracted over the whole map. γI_0 and the peak location are stored as a list of "delta components". Third, the resulting map is searched for the next pixel with peak intensity and the process is repeated until the peak fails to satisfy the condition mentioned in step one. Fourth, all the delta components removed in previous iterations, which are called the *clean components*, are convolved with a *clean or restoring beam* (typically with a FWHM comparable to the central lobe of the dirty beam) at their respective positions and amplitudes, and added to the residual map.

This procedure contains numerous parameters that can be varied to allow detection of source emission with relative ease, and some of which help in reducing the computation time

also. For instance, instead of searching the entire map for the pixel with peak intensity where the dirty beam should be next subtracted, the search can be restricted to within *clean windows* where the source emission is suspected to be distributed. The gain loop, γ, is usually set to a small value ~ 0.1 for better numerical stability but can be varied through the iterations.

Lastly, it should be pointed out that the CLEAN algorithm in non-linear in that the location and flux density of the component to be subtracted in the next iteration is judged based on a criterion. This criterion can be understood by defining the residual function, R^2 (Wucknitz 2002), in the uv–plane after subtracting a component at $\vec{x}_0$

$$R^2 \;=\; \sum_k w_k \left| \tilde{I}_k - S e^{2\pi i \vec{u}_k . \vec{x}_0} \right|^2 , \tag{3.26}$$

where $\tilde{I}_k$ are the residual visibilities, S and $\vec{x}_0$[3] represent the strength and the position, respectively, of the last component which was subtracted. This can also be written as

$$\begin{aligned} R^2 \;&=\; \sum_k w_k \left[|\tilde{I}_k|^2 + S^2 - 2S \sum_j (\tilde{I}_j e^{2\pi i \vec{u}_j . \vec{x}_0}) \right] , \\ &=\; \sum_k w_k \left[|\tilde{I}_k|^2 + S^2 - 2S I^d(\vec{x}_0) \right] , \\ &=\; R_0^2 - \sum_k w_k \, \Delta R^2 , \end{aligned} \tag{3.27}$$

where

$$\begin{aligned} R_0^2 \;&=\; \sum_k w_k \, |\tilde{I}_k|^2 , \\ \Delta R^2 \;&=\; 2 S I_D(x_0) - S^2 , \end{aligned} \tag{3.28}$$

and I_D is the dirty map,

$$\begin{aligned} I_D(\vec{x}) \;&=\; \frac{1}{\sum_k w_k} \sum_k w_k \, \tilde{I}_k \, e^{-2\pi i \vec{u}_k . \vec{x}} , \\ B(\vec{x}) \;&=\; \frac{1}{\sum_k w_k} \sum_k w_k \, e^{-2\pi i \vec{u}_k . \vec{x}} . \end{aligned} \tag{3.29}$$

$B(\vec{x})$ is the synthesized beam [see Eq. 3.24] normalized with the sum of the weights to have the units of flux-density. The optimal position of the pixel to be subtracted next (in retrospect) is found from minimizing R^2 in Eq. 3.27 with respect to S. The solution is found to satisfy $S = I_D(\vec{x}_0)$, indicating that the optimal position coincides with $\vec{x}_0$. It is necessary to consider this foundation when describing the LensClean algorithm (Sect. 3.5.2).

In practice, the data are alternately processed through imaging tasks, such as CLEAN, and the self-calibration routine as shown in Fig. 3.4. The left part of the flowchart (image- or map-plane) consists of a trial model on which CLEAN is applied. This map is then Fourier transformed into the uv–plane (right part of the flowchart) and the visibilities are adjusted to comply with the observed closure phases. This is done by varying the antenna-based gains to minimize the least square difference between the trial and the observed visibilities, with the

[3] $\vec{u}_k \equiv (u_k, v_k)$, $\vec{x}_0 \equiv (x_0, y_0)$ and $\tilde{I}_k \equiv \tilde{V}(u_k, v_k)$.

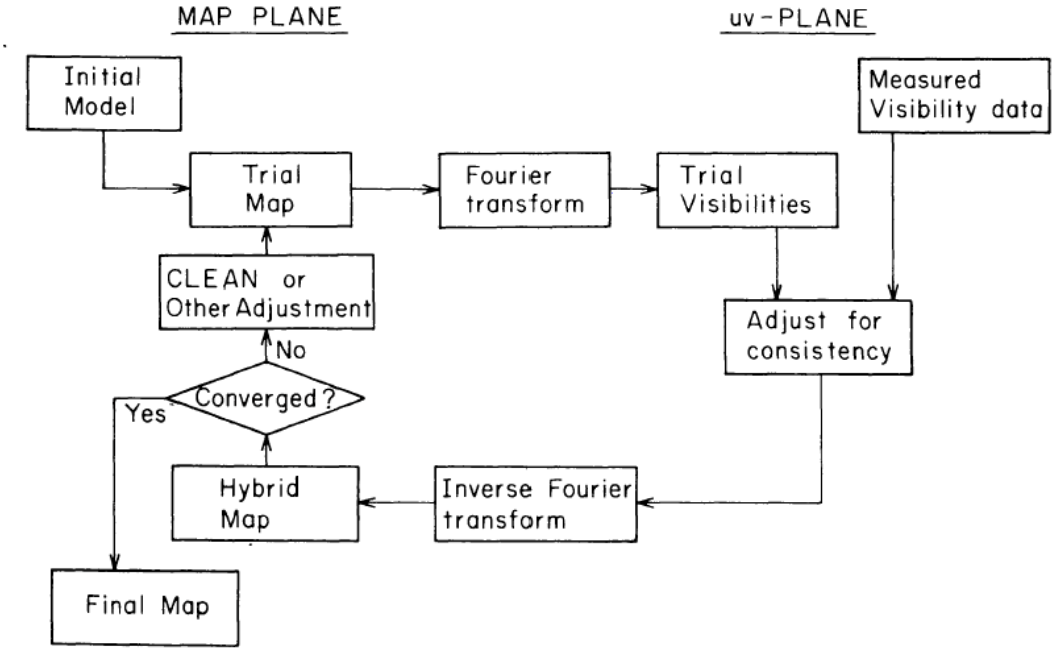

Figure 3.4: Iterative procedures including CLEAN and self-calibration used for hybrid-mapping (Pearson & Readhead 1984)

choice of increasing the weights of the visibilities [preferably $(N-1)$ in number] that best fit the data (self-calibration). The resulting best-fitting visibilities are Fourier inverted to make a new map and the procedure is repeated until the rms noise in the map can be reduced no further. This process of making a map is called *hybrid mapping*.

To minimize the computational power needed, Clark (1980) modified the CLEAN algorithm by accumulating many CLEAN components in a single step (minor loop). These are subtracted collectively from the visibilities and re-Fourier-transformed to obtain a new 'dirty-map' of the image (major loop). In the minor loop, the clean components are selected such that their intensities as a fraction of the maximum are more than the highest exterior side-lobe. These components are transformed back and forth between the image-plane and the *uv*–plane using FFT. This is called the Clark CLEAN algorithm. A yet further development was made by Schwab (1984) to avoid gridding errors by subtracting the visibilities from the ungridded visibility data. This method has a second advantage in that multiple fields can be simultaneously and independently 'cleaned' within the minor loop and then subtracted in the major loop at the same time. This routine is commonly called the Cotton-Schwab algorithm.

In VLBI observations of gravitational lenses, such as B0218+357where the flux is known to be confined to discrete and separated regions of the image plane, the Cotton-Schwab method is particularly useful as it allows mapping of separate image subfields.

3.5.2 LensClean

LensClean (LC) (Kochanek & Narayan 1992) derives motivation from the success of the CLEAN algorithm, discussed in the previous section. Its working principle is similar but

is adapted to be more appropriate for the 'cleaning' of gravitationally lensed images. The main purpose of LC is to derive a model for the brightness distribution of the background lensed source and, simultaneously, a model for the lens mass distribution, that together fit the observed visibilities of lensed images the best.

The LC algorithm has undergone several stages of modifications, primarily by Ellithorpe et al. (1996) and Wucknitz (2004). Since the lens model used for the investigation of B0218+357 image flux-density ratios, described in chapter 5, is derived from the LC version introduced by Wucknitz (2004), in the following the main points of this version of the algorithm are described. As in normal CLEAN, the data are Fourier transformed back and forth between the uv–plane, where the visibilities corresponding to the brightness distribution of the lensed images are determined, and the xy–plane or image (lens) plane, where the 'dirty' lensed images are 'cleaned'. In addition, there is a source plane, also defined in the xy–plane, that corresponds to the unlensed object. All the planes are gridded and the data are regularly spaced in pixels. Consider a source pixel $\vec{y}_s$ which is lensed into n images at position $\vec{x}_j$ with magnification given by μ_j, where $j = 1 \ldots n$. The lens model used to evaluate the image positions and the magnifications for a given source pixel is the best available one at this point. Then, the emission contributed by all these image components are subtracted from the measured visibilities in a single step resulting in a residual function, analogous to Eq. 3.26,

$$\begin{aligned} R^2 &= \sum_k w_k \left| \tilde{I}_k - S \sum_j \mu_j e^{2\pi i \vec{u}_k . \vec{x}_j} \right|^2 , \\ &= R_0^2 - \sum_k w_k \, \Delta R^2 , \end{aligned} \tag{3.30}$$

where the contraction made in the last step is analogous to Eq. 3.27 but with a modified definition of ΔR^2 (the variant):

$$\Delta R^2 = 2S \sum_j \mu_j \, I_j - S^2 \sum_{jj'} \mu_j \mu'_j B_{jj'} , \tag{3.31}$$

where $I_j = I_D(\vec{x}_j)$ and $B_{jj'} = B(\vec{x}_j - \vec{x}'_j)$ [see Eq. 3.29]. One of the main differences between the original version of LC and the succeeding ones is that in the original one the residual function is described in the image plane instead of in the visibility (source) plane. Once again, demanding steepest decline in the residual function, the optimal position of the component to be subtracted next is determined by locating the maximum in the residual function. This component has the flux-density,

$$S = \frac{\sum_j \mu_j \, I_j}{\sum_{jj'} \mu_j \mu'_j B_{jj'}} \tag{3.32}$$

As in CLEAN, the flux-density subtracted at the image positions is only a fraction of S in Eq. 3.32 and is specified by the loop gain γ. On substituting γS into Eq. 3.31 gives

$$\Delta R^2 = \gamma(2-\gamma) \, \frac{\left(\sum_j \mu_j \, I_j \right)^2}{\sum_{jj'} \mu_j \, \mu'_j B_{jj'}} . \tag{3.33}$$

To avoid any kind of biasing in making comparisons between different lens models, which are equivalent in terms of ability to reproduce the observed visibilities, Wucknitz (2004) modified

the variant to be independent of the number of images predicted by a lens model for a given source position. A lens model reproducing a greater number of images will otherwise be given a higher weight since it will lead to subtraction of a larger amount and, consequently, decrease the residuals faster and introduce a bias. The modified ΔR^2 is given by

$$\Delta R'^2 \;=\; g\,\frac{\sum_{jj'}\,\mu_j\,\mu'_j B_{jj'}}{\sum_j\;\mu_j\,I_j}\,\Delta R^2\,, \tag{3.34}$$

where g is similar to the loop gain factor in Eq. 3.33, and the next component is searched for by locating the maximum of $\Delta R'^2$. This is accompanied by a commensurate change in the value of the flux-density removed at this position,

$$S' \;=\; \left(1-\sqrt{1-g\frac{\sum_{jj'}\,\mu_j\mu_\prime B_{jj'}}{(\sum_j\,\mu_j)^2}}\right)\,S\,. \tag{3.35}$$

Having described the mathematical elements of the LC algorithm, the actual steps involved in building the source-plane emission model and determining the optimal lens model parameters for B0218+357 are as follows: There is a major and a minor loop, the major loop is initiated by fixing the lens centre and obtaining the five parameters of a classical lens model, a Singular Isothermal Elliptical Potential (SIEP), from the observed radio constraints.

This calls for a digression into examining the available radio constraints for determination of the lens model in the lens system B0218+357. As a reminder, the position of the lens galaxy in B0218+357 is not well-known relative to the lensed images because of weak optical emission associated with it (see Sect. 2.3.3) and it is completely invisible at radio wavelengths. Therefore, if only the VLBI core-components are taken into account, their relative separation and flux-density ratio amounts to three constraints. If the subcomponents (component 2) are also taken into account, then the number of constraints, in principle, increases to five. But one of the most important goals of using LC on the radio observations of B0218+357is to estimate the position of the lens galaxy relative to the images accurately enough to determine the Hubble constant with the help of the time-delay. From this point of view, the two additional constraints do not give any further valuable information. This is because while one of the components of the separation vector is in a direction almost radial with respect to the mass centre (and for isothermal profiles, there is no radial magnification), the other (perpendicular component) is in a direction along which the Hubble constant does not vary. The number of parameters for a SIEP model, on the other hand, is five: the lens mass strength, ξ_0, the ellipticity, ϵ_x and ϵ_y, and the lens galaxy position, x_{01} and x_{02} (see Sect. 1.3.2). Three of these can be fitted quite well using the constraints contributed by the core-components only. To fit all five parameters, the lens position can be varied over the suspected regions in the lens plane and for each fixed position, the remaining three parameters are fitted.

The algorithm then enters the minor loop. Using the classical lens model determined in the major loop, for every pixel of the primary image in the lens plane, the corresponding pixel in the source plane is calculated. The next step is to locate all the other image positions and their magnifications. This requires analytic inversion of the lens equation which results in a quartic equation to solve. Since one of the image positions is known (the primary image), the equation can be reduced to a cubic one. After this, using the modified variant and the flux-density, the source-pixel to be subtracted for the next iteration is located. After completion of a few iterations, the collected components are subtracted from the ungridded visibilities

and, in this aspect, the LC algorithm resembles the Cotton-Schwab algorithm mentioned at the end of Sect. 3.5.1. This process continues until a fixed pre-defined number of iterations is completed. The final lens-model within the minor loop is selected from minimization of the residual function.

The algorithm jumps to the major loop once again and the residual function determined in the minor loop is tested for convergence. In a non-satisfactory case, the lens model parameters are slightly varied and the minor loop is re-activated. This entire process is only for a single lens-position, and is repeated until all suspected lens-positions are scanned and convergence attained. The outer-most shell of the LC algorithm is the self-calibration loop, which provides further stability and robustness to the procedure. The advantage of using the modified version of LC appears as a vast reduction of the computational effort as the number of iterations needed to obtain a satisfactory model is decreased by a factor of more than 50. Whereas both the methods provide similar results in the limit of large iterations, the residual function is significantly improved on using the new variant.

4 Multi-frequency and phase-referenced VLBI observations of B0218+357

Although the technique of phase-referencing (see Sect. 3.4) is most often used for mapping faint radio sources, the target in this study, B0218+357, is sufficiently strong ($\sim$ 1 Jy) that inverse phase-referencing can be used. Here, that target is used as the phase-reference for determining the corrupting phases, and phase-reference maps of a point-like, achromatic position-reference source are made. One advantage is that relatively faint sources can be used as position-references, permitting the choice of sources closer to the target, which minimizes telescope drive times and reduces any difference between the tropospheric and ionospheric phase corruptions of the target and reference. Another advantage is that multiple astrometric reference sources can be used to guard against the possibility that any single one may have chromatic structure.

4.1 Observations

VLBI observations of B0218+357 were made at five frequencies, 15.35 GHz, 8.40 GHz, 4.96 GHz, 2.25 GHz and 1.65 GHz, using the NRAO Very Long Baseline Array (VLBA) and Effelsberg radio telescope (Eb). Two 14 h source tracks were used (13^{th} to 14^{th} and 14^{th} to 15^{th} January, 2002) and for each track (19 h to 03 h UT for Eb, 19 h to 09 h UT for the VLBA) the observations were switched between two receivers every 22 min. For the first track, observations were alternated between 4.96 GHz and 2.25 GHz/8.40 GHz (S and X dual band), and for the second track between 1.65 GHz and 15.35 GHz. Other observational details are given in Table 4.1

Apart from observing B0218+357, three compact reference sources were observed (see Table 4.2) along with a fringe finder, B0234+285. Scans on B0218+357 of 2 min duration were

Table 4.1: The technical details of the phase-referenced observations. The second column gives the antennas that contributed to the data (Br: Brewster, Fd: Fort Davis, Hn: Hancock, Kp: Kitt Peak, La: Los Alamos, Nl: North Liberty, Ov: Owens Valley, Pt: Pie Town, Sc: St. Croix, Mk: Mauna Kea and Eb: Effelsberg) at the observing frequency given in the first column. The third column is the number of 8 MHz baseband channels and the fourth column is the polarization mode (left or right hand circular polarization). 'w.o.' denotes without.

ν (GHz)	Antennas	# of IF channels	Sampling type	Polz. mode
1.65	VLBA (w.o. Pt and Mk)	4	2-bit	LHC
	Eb	2		
2.25	VLBA (w.o. Kp)	4	1-bit	RHC
4.96	VLBA and Eb	8	1-bit	LHC
8.40	VLBA and Eb	4	1-bit	RHC
15.35	VLBA (w.o. Hn)	4	2-bit	LHC

Table 4.2: The position-references, their separations from B0218+357, the correlated flux-density on the short EVN baselines (S–EVN) and on the long EVN baselines (L–EVN) at 5 GHz. The ratio L/S is a measure of source-compactness

Source name	Separation (degrees)	S–EVN (mJy)	L–EVN (mJy)	L/S
NVSS B0210+366	2.03	127	85	0.66
NVSS B0215+364	1.03	140	86	0.61
NVSS B0222+369	1.30	151	91	0.61

interleaved by scans of 1 min 20 s duration on each of the calibrators in succession. The position-references were selected from the NRAO VLA Sky Survey (NVSS) catalogue. From an initial sample of candidate sources, these three were found to exhibit flat spectra and the most point-like structure on the basis of EVN and MERLIN 5 GHz observations (Porcas 2001). They all lie within two degrees of B0218+357 and are stronger than 25 mJy at both 1.4 GHz and 5 GHz, with spectral indices flatter than 0.47 ($F \propto \nu^{-\alpha}$).

The data were correlated at the VLBA correlator, with an output averaging time of 2.1 s and a frequency resolution of 0.5 MHz, and further processed in AIPS, the Astronomical Image Processing Software package provided by NRAO.

4.2 AIPS data analysis and maps

The experiment was designed to give information on the total intensity only, and not on any of the polarization properties of the source; therefore the data were observed in single polarization mode. The various calibrations made before global fringe-fitting are described in the following subsections.

4.2.1 Pulse calibration

This step is needed to determine and remove the phase-offsets and slopes between different basebands (or intermediate-frequency channels, IFs) and across the basebands, respectively. Such phase inaccuracies may be due to instabilities in electronics or different cables lengths that connect the antennas to the recording system. These can be solved by injecting pulse tones at the antenna receivers at two or more frequencies within each baseband. By measuring the cross-correlation of the pulses, the phase-ambiguities can be resolved. There may still be a further ambiguity due to the unknown number of phase-turns (2πN) between the pulse tones. For this, visibilities of a calibrator source scan are used and the phase-delays for the rest of the scans are assumed to be the same. Shown in Fig. 4.1 are the visibility phases and amplitudes for the calibrator source (the fringe-finder) B0234+285 before (top panel) and after (lower panel) pulse-calibration is applied and the differences are clearly noticeable. The visibilities are obtained from three baselines to the reference antenna (La), and on applying the pulse-calibration, the phases line up well within each IF for two of the baselines (Br and Fd) and the phase-offsets between the IFs also disappear. For Eb, there were no pulse tones available for the scan chosen to resolve the phase-ambiguities, hence the phase-slopes and offsets remain.

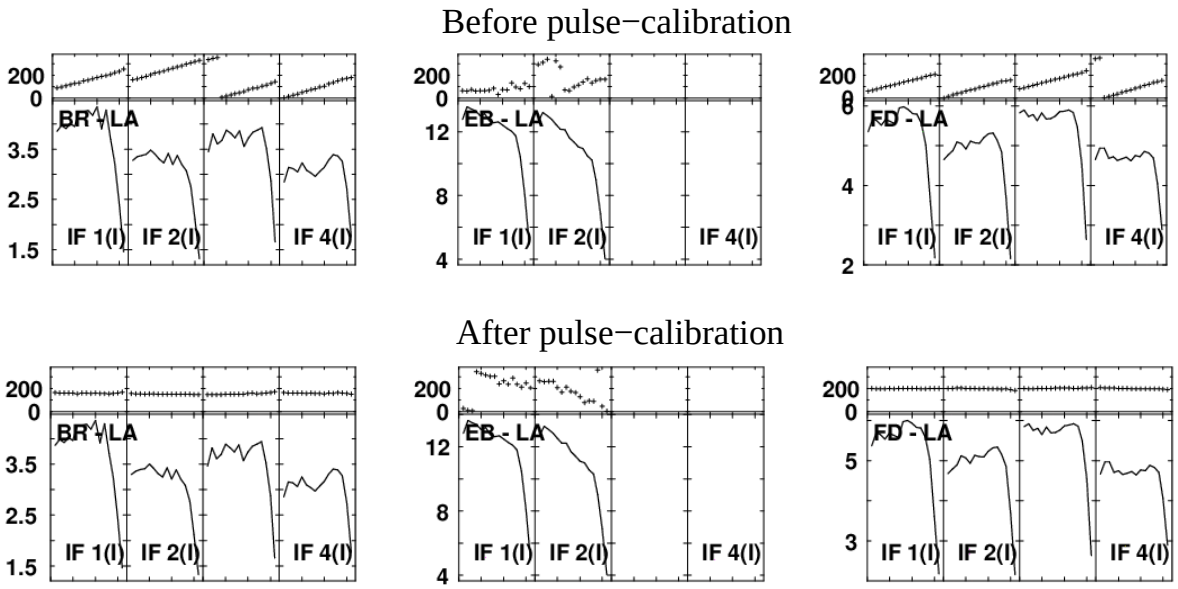

Figure 4.1: The phase (in degrees, top frame of each panel) and amplitude (in units of $1/1000^{\text{th}}$ of the correlation coefficient, lower frame of each panel) of the fringe-finder B0234+285, before applying the pulse-calibration (top panel) and after (lower panel). The baselines are mentioned at the top left corner and the observing frequency is 1.65 GHz. For Eb, no pulse-calibration was available for the duration of the scan chosen to calibrate the data.

4.2.2 Ionospheric calibration

For hybrid-mapping, most of the a-priori calibration steps are unnecessary. Although their application makes the task of fringe-fitting to solve for the phase-rates and phase-delays easier, in most cases where the target source is strong the solutions are found even without applying any. But for phase-reference observations, it is essential to apply the a-priori ionospheric calibrations. The need arises due to the assumption of similar tropospheric and ionospheric phase errors for the reference and the target source [see Eq. 3.18]. For VLBI observations the extra paths through the troposphere and ionosphere (see Appendix E) are very different for different antennas due to differences in atmospheric conditions above the antennas along their respective lines of sight to the source, primarily because the source is seen at different elevations. The mean phase errors due to the troposphere, which scale as ν, can be estimated approximately for each antenna, and are taken into account in the model used for correlation. The mean phase errors due to the ionosphere, which scale as ν^{-1}, are highly unpredictable, however, and thereby prohibit the use of any model at the time of correlation. Since the errors become pronounced at long wavelengths, it is necessary to apply phase corrections from an ionospheric model after correlation. In applying the ionospheric and tropospheric models, it is only the mean phase offset that is removed from every antenna. The terms corresponding to small-scale temporal and spatial fluctuations still remain and it is hoped that they are the same for the target and the reference source.

For these observations, the AIPS task TECOR was used to apply an ionospheric model, produced by the Jet Propulsion Laboratory (JPL). The model is calculated using the ionospheric data gathered by the GPS (Global Positioning System) community which provides maps of the total electron content (TEC) [see Appendix E.2] at the zenith as a function of

longitude, latitude and time (with a spatial resolution of 5 °, and temporal resolution of 2 hr). Presently, there are five groups that use the GPS data to model the ionosphere; their models are available at CDDIS (Crustal Dynamics Data Information System) data archive, and even though their results show a scatter at the level of 20 % to 50 %, in most cases calibrated data improves the results of phase-referencing (Walker & Chatterjee 1999). To investigate the efficacy of the ionospheric model, the phase-referenced images made with and without ionospheric phase corrections were compared. One such comparison can be seen in Fig. 4.2 which shows maps of B0215+364 at 2.25 GHz. The peak flux per unit beam is almost 1.5 times higher if an ionospheric model is used. Moreover, the peak positions differ by almost half a milliarcsecond.

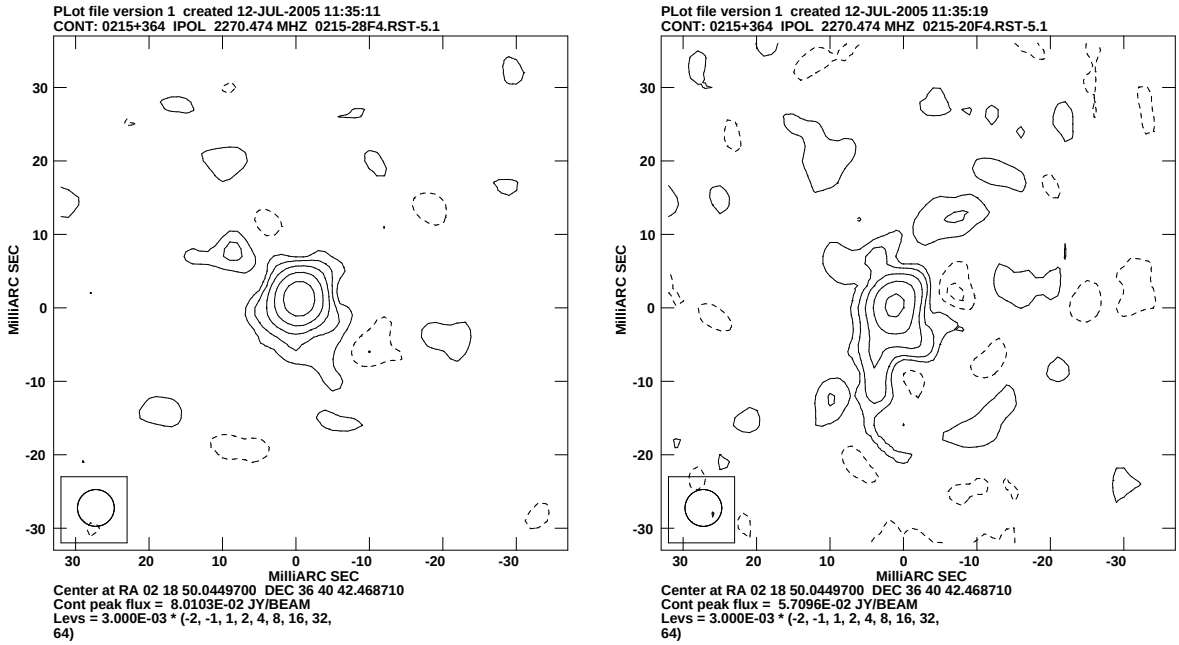

Figure 4.2: Maps of 0215+364 at 2.3 GHz using a restoring beam of 5 mas and contour levels at multiples of 3 mJy. (a) Inverse phase-reference map with ionospheric phase calibrations applied to the data. (b) Without ionospheric phase calibrations.

4.2.3 Standard-calibration

In the further analysis standard reduction procedures described in chapter 3 were used, applying amplitude calibration derived from telescope radiometry measurements and using fringe-fitting, self-calibration, CLEAN deconvolution procedures and mapping. To prevent fringe-rate and bandwidth smearing, 2 s and 8 MHz data samples were used for mapping. As mentioned earlier, B0218+357 is sufficiently strong that self-calibration procedures could be applied at all frequencies. Hybrid maps were made using the AIPS task 'IMAGR' in which the CLEAN algorithm is implemented. Two subfields were cleaned simultaneously, one for image A and the other for image B. After initial maps had been obtained the fringe-fitting was repeated using these as an input model, and the mapping was repeated. Full resolution hybrid

Table 4.3: The flux-densities (S, in mJy) of the position-references and the rms noise (σ, in mJy beam^{-1}) in the hybrid maps.

ν (GHz)	B0210+366		B0215+364		B0222+369	
	S	σ	S	σ	S	σ
1.65	30.86	0.32	100.41	0.15	100.04	0.16
2.25	54.37	0.40	111.44	0.31	119.00	0.29
4.96	132.81	0.19	103.20	0.16	164.65	0.16
8.40	170.21	0.31	93.55	0.28	159.38	0.27
15.35	146.89	0.35	75.85	0.29	122.48	0.34

maps of both A and B images made using the natural weighting scheme at all five frequencies are shown in Fig. 4.3. The origin (0,0) of these maps is defined by the position of the peak intensity found in the initial run of fringe-fitting. This is the centre of A at all frequencies except for 1.65 GHz at which the peak is in image B, resulting in an offset in the labeling of the axes. The images clearly manifest all the earlier observed lensing-characteristics. Image A is tangentially stretched at a PA $\sim -30\,^{\circ}$ and image B seems to be tangentially compressed. At 8.4 GHz and 15.35 GHz the images reveal further substructure, subcomponents 1 and 2 with ~ 1.4 mas separation, reproducing the core-jet morphology of the background source.

All three position-references also proved to be strong enough to use phase self-calibration, and hybrid maps were therefore also made of these. On inspection, two of these sources were deemed to be unsuitable as position-references. For B0210+366 the flux-density drops to about 30 mJy at 1.65 GHz (see Table 4.3) and consequently the position of the emission peak is not well defined. The maps of B0222+369 reveal a jet like feature at 2.3 GHz and 1.6 GHz, casting doubt as to whether the position of the peak is achromatic. Therefore for further analysis only B0215+364 was used as a position-reference; it appeared most point-like in the maps at all frequencies. An amplitude self-calibration procedure was used on this source to determine corrections to the *a priori* amplitude calibration (see Sect. 3.3.4), and these were then applied to the B0218+357 data to improve the maps. The Spectral Energy Distribution (SED) of the three position-references is shown in Fig. 4.4 and their contour plots at all the frequencies are shown in Fig. 4.5.

Phase-reference maps of B0215+364 were made at all frequencies by applying the self-calibration solutions obtained from B0218+357 to the B0215+364 data, and are shown in Fig. 4.6. The dynamic range of these maps is poor and deteriorates with increasing frequency from $\sim$ 30:1 to $\sim$ 4:1, and the rms noise increases from 1 mJy to 1.5 mJy. The reason for the degradation in the quality of the phase-referenced maps is difficult to determine. Ionospheric phase errors scale as ν^{-1}, therefore improper ionospheric phase-calibration can be ruled out. Atmospheric phase errors scale as ν and even though the mean first-order error terms are accounted for by applying corrections at the correlator, second-order error terms might still persist. No further attempts have been made to provide a more precise atmospheric model. Other systematic errors which may be responsible for the loss in flux-density at higher frequencies include geometrical errors that corrupt only a subset or subsets of the uv visibilities. For example, an error in the assumed source position will corrupt all the

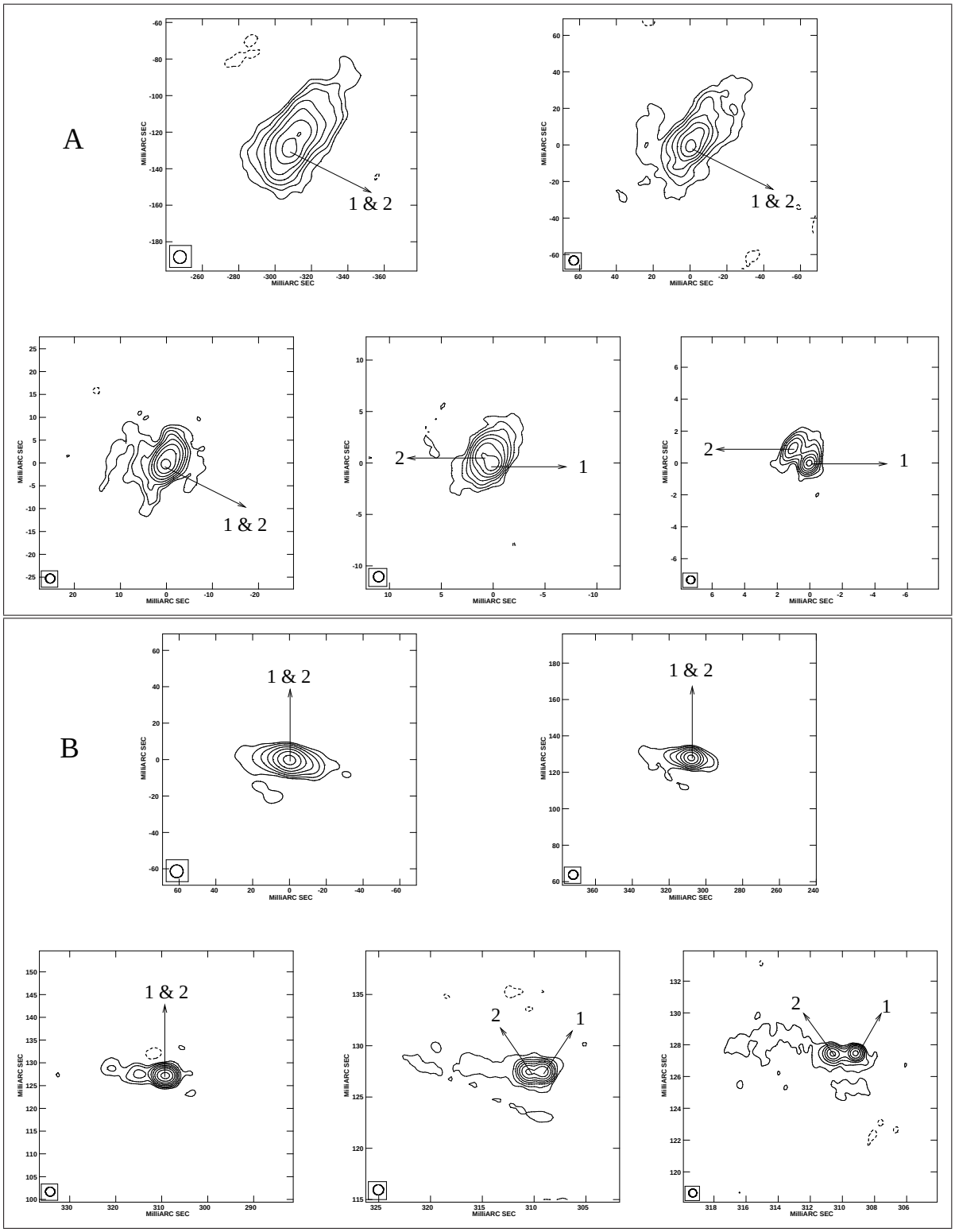

Figure 4.3: The top and bottom panels show 1.65 GHz, 2.25 GHz, 4.96 GHz, 8.40 GHz and 15.35 GHz maps of images A and B respectively, with frequencies increasing from left to right, top to bottom. The residual noise in the maps is ≤ 500 μJy beam^{-1}. The restoring beams used are (7, 5, 2, 1, 0.5) mas in the order of increasing frequency.

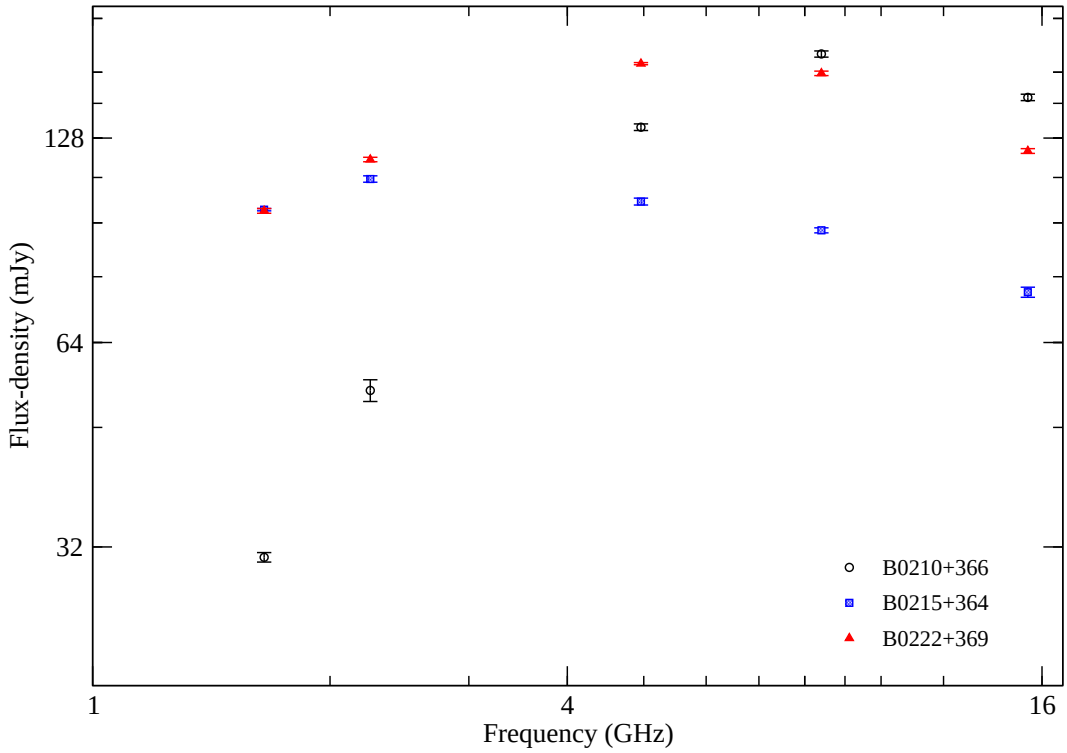

Figure 4.4: The spectral energy distribution of the position-references. The error bars are 3 σ where σ is the rms noise in the maps.

visibilities in a similar way, resulting in all the point-like components shifting coherently in the image plane, changing the position of the peak emission but leaving the structure and the flux-density of the image intact. This might not be the case if only one antenna or a subset of antennas are in error. Then, only a subset of the visibilities will contribute to the geometrical errors. Further, these errors will be different for the target and the reference sources (because of slightly different source directions, see Fig. 3.1) and the difference scales as ν $\times$baseline length. To test this scenario, phase-reference maps of B0215+364 were made using a subset of closely spaced antennas only. The resulting maps, although having a slightly higher dynamic range due to relatively bigger beams, did not improve the positional accuracy of the peak emissions at different frequencies. The differences in peak-positions in maps made using all the antennas and only a subset of antennas are negligible in comparison with the positional uncertainties and, therefore, not considered any further.

4.3 Results

4.3.1 Image flux-densities and flux-density ratios

The image flux-densities and flux-density ratios from these observations are presented in Table 4.4. To guard against loss of flux-density due to over-resolution, low-resolution maps were also made by discarding data from the longest baselines (using uv resolution cut-offs). The flux-densities from these maps were estimated by putting a box around the images and integrating the flux-density within the box. The errors on the integrated flux-densities given in Table 4.4 are derived from examining the spread in estimates obtained by varying a number

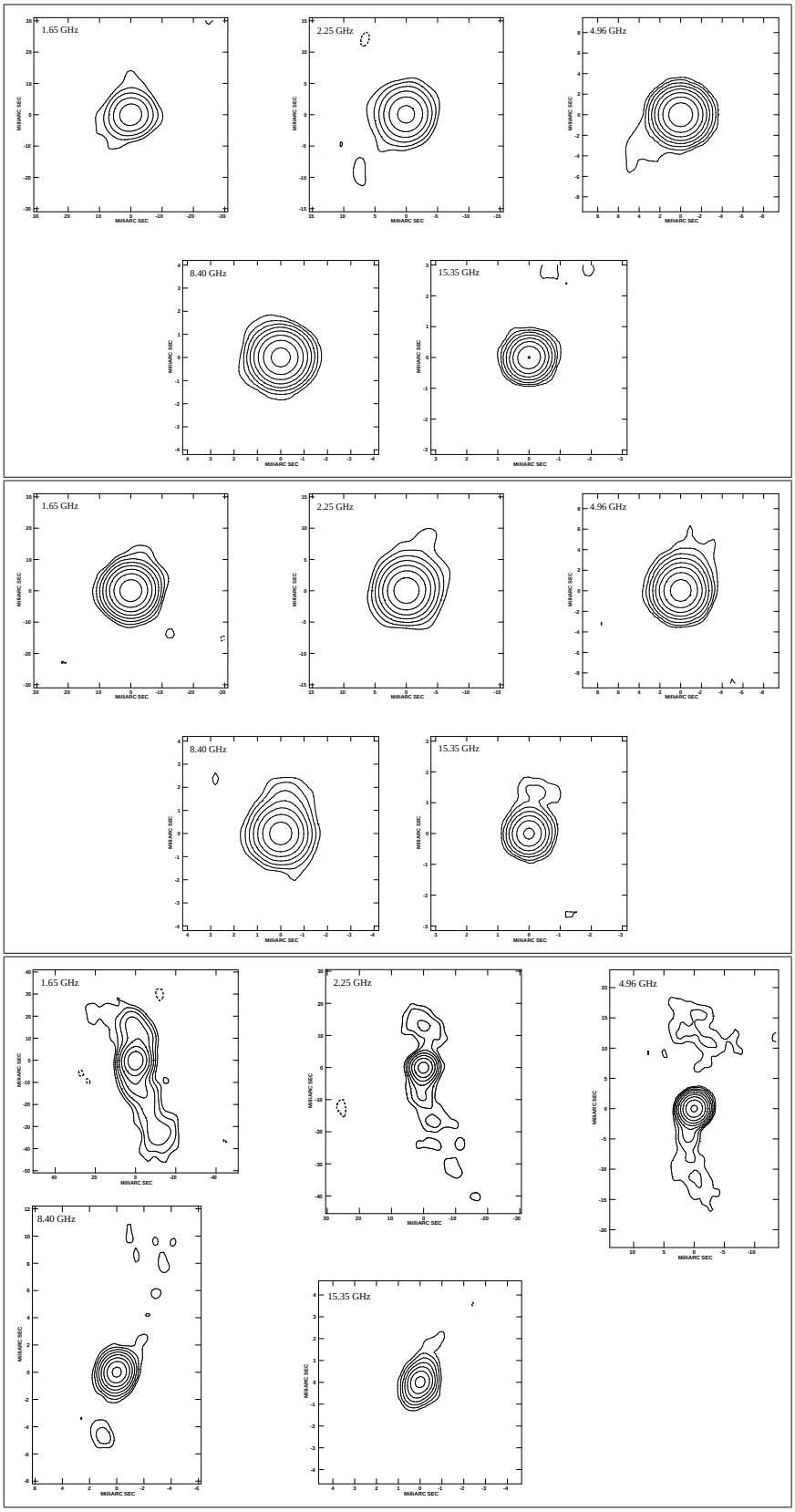

Figure 4.5: Hybrid maps of the position-references B0210+366, B0215+364 and B0222+369 from top to bottom, respectively, with resolutions of (8, 4.5, 2.5, 1.2, 0.7) mas in the order of increasing ν. The contour levels are at (-1,1,2,4,8,16,32,64) $\times$ 3σ, where σ for all three position-references at different frequencies is given in Table 4.3.

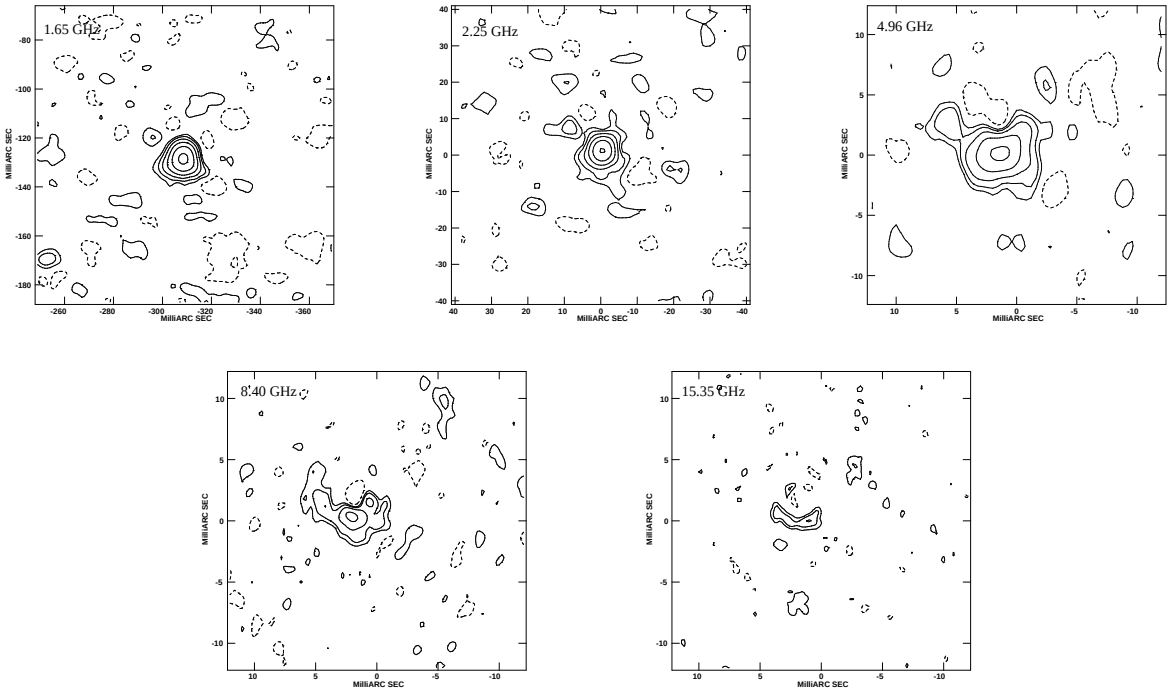

Figure 4.6: Phase-reference maps of B0215+364 with resolutions of (8, 5, 2.5, 1.2, 0.8) mas in the order of increasing ν. The contour levels are at (-1, 1, 2 ,4, 8, 16, 32) multiples of (2 to 3) σ where σ is the rms noise in the maps and is $\lesssim 1.5$ mJy.

Table 4.4: The B0218+357 image flux-density ratios (A/B) obtained from this data set. S denotes the flux-density, b denotes the resolution and σ is the rms noise in the maps.

ν (GHz)	b (mas)	σ (mJy/beam)	$S^{\rm A}$ (mJy)	$S^{\rm B}$ (mJy)	$S^{\rm A}/S^{\rm B}$
1.65	50	0.35	504 ± 9	249 ± 5	2.02 ± 0.05
2.25	50	0.48	646 ± 16	243 ± 7	2.67 ± 0.10
4.96	30	0.25	650 ± 9	217 ± 3	3.00 ± 0.06
8.40	10	0.50	681 ± 8	206 ± 8	3.31 ± 0.13
15.35	5	1.00	661 ± 5	171 ± 6	3.87 ± 0.14

of parameters in the imaging process, including the *uv* resolution cut-offs, and are larger than the formal errors obtainable either from a Gaussian fit, such as JMFIT or IMFIT (see Sect. 4.3.4 and Table 5.3), or from the rms noise in the maps. Shown in Fig. 4.7(a) are the image spectra and it can be seen that image A flux-density remains almost constant (to within $\pm$ 25 mJy) at the upper four frequencies but drops suddenly by about 130 mJy (20 %) at 1.65 GHz. In contrast, image B shows a gradual, monotonic increase with wavelength with no sharp drop. It is to be noted that the variation of the image flux-density ratio, as shown in Fig. 4.7(b), is similar in trend to that found for previous observations, although the range is even larger (~ 4 to ~ 2), with the value at 1.65 GHz differing most from previous estimates.

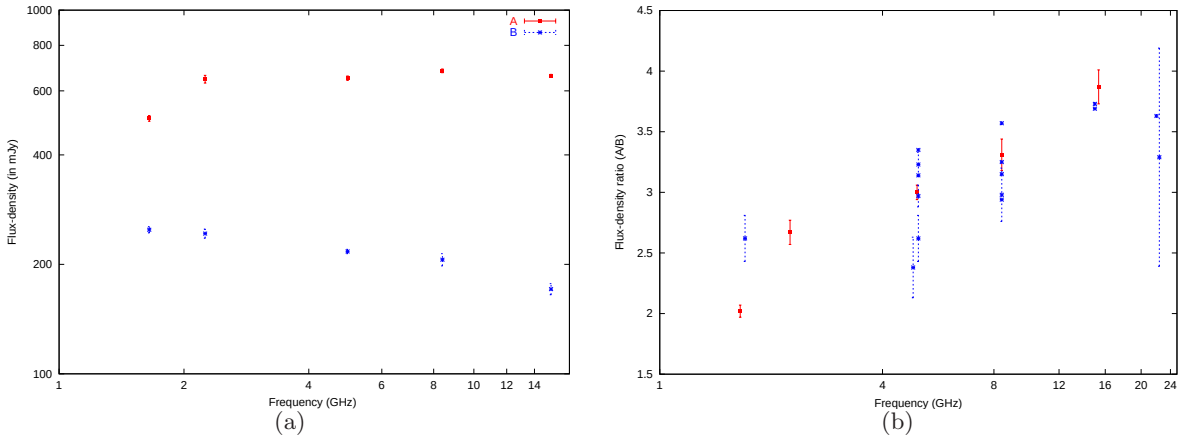

Figure 4.7: (a) Flux-densities of image A (red filled squares) and image B (blue crosses) obtained from these observations. (b) Image flux-density ratio from these observations (red filled squares and solid error bars) and previous observations (blue crosses and dashed error bars, see Table 2.2).

4.3.2 Phase-referencing

The result of the phase-reference observations is shown in Fig. 4.8, which shows the variation with frequency in the centroid position of the radio emission in the images with respect to B0215+364. For this investigation, the centroid position is a more relevant quantity, rather than the peak position, since it is a better representative of the image brightness distribution at different frequencies. To determine an image centroid position, the CLEAN components were convolved with a low-resolution restoring beam, and the peak in the resulting map was located using AIPS tasks MAXFIT, which fits a quadratic function to the brightest area of the map to determine the position offset with respect to the map centre. The same steps were followed to locate the offset from the map centre of the peak position of the calibrator, 0215+364, but using a full-resolution, phase-referenced map. The position of the B0218+357 image centroid with respect to 0215+364 (ignoring the constant position difference used for correlation) is then given by the difference of these offsets (B0218+357 – 0215+364). The same procedure was used for image B. The right panel of Fig. 4.8 indicates a relative shift of $\sim$ 3.5 mas in the centroid of image A between 15.35 GHz and 1.65 GHz, although the shift occurs only at 1.65 GHz. For image B, on the contrary, there is no shift detected in the centroid of the brightness distribution. From the Singular Isothermal Elliptical Potential (SIEP) model used in chapter 5 (see Table 5.1), it is found that a shift of 3.5 mas may cause the flux-density ratio to change as much as ~ 0.5. Assuming a true value of 3.9[1] for the relative image-magnification produced by the macro-model, this corresponds to ~ 10 % change in the observed flux-density ratio. However, this depends upon the direction in which the shift has occurred. From the phase-referenced results for image A, it is inferred that this direction roughly coincides with that of the constant relative magnification contours (more or less tangential with respect to the lens centre). The relative image-magnification at the 1.65 GHz centroid position corresponds to ≤ 1 % change in the observed ratio. Therefore the conclusion may be drawn that the measured shift with frequency of either image centroid positions is *not sufficient* to account

[1]this is the relative image-magnification for a point source at the position of A1 at 15.35 GHz using an isothermal mass-radius profile.

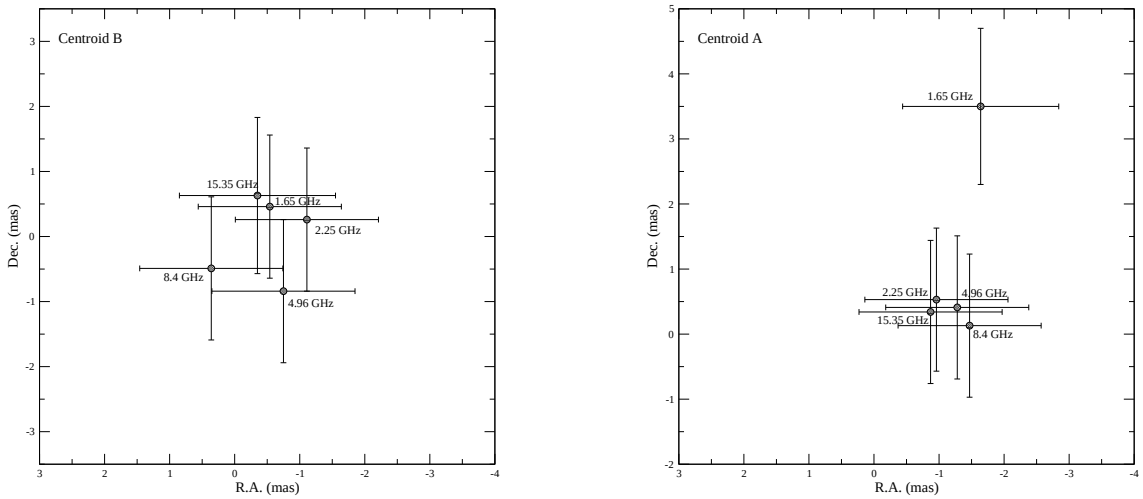

(a) (b)

Figure 4.8: The change in the centroid position relative to the position-reference B0215+364, at five frequencies. The error bars at 1.65 GHz, 2.25 GHz and 4.96 GHz are dominated by the position uncertainty in the B0218+357 maps due to the use of relatively large beams, and at 8.4 GHz and 15.35 GHz due to the position uncertainty of B0215+364 caused by the poor dynamic range of the phase-referenced maps at these frequencies. (a) For image B. (b) For image A.

for the flux-density ratio anomaly for B0218+357. However, it should be emphasized that this magnification change due to the shift in the centroid position in image A is only an approximate result, which has been derived based on the assumption that the relative image-magnification at the centroid position is the true relative image magnification (see chapter 5).

4.3.3 Image-separation

An advantage of imaging gravitational lenses is that any frequency-dependent position in the source can be seen as a frequency-dependence of the separation vector of the lensed images, without requiring the use of an external reference source. As mentioned in Sect. 2.7, this method is insensitive in cases where the position shift is along the same direction in both the images, but the accuracy of the measurement of the A−B separation is much higher than for that between B0218+357 and B0215+364. The peak-to-peak image separations at different frequencies, measured with MAXFIT in full resolution maps, are shown in Figure 4.9 as red crosses. Since the images at 15.35 GHz are resolved into subcomponents 1 and 2, the separations of both A1−B1 and A2−B2 are indicated in the plot. It is seen that the separation at 15.35 GHz (A1−B1), 8.4 GHz and 4.96 GHz remains roughly the same, implying that the "peak" is centred around component 1 in both the images. At 2.25 GHz and 1.65 GHz, the separation increases in declination and decreases in right ascension, in a direction opposite to component 2. This is surprising as one might expect the separation at lower frequencies to gradually coincide with the A2−B2 separation, reflecting relatively more prominent emission from component 2. Shown in the same figure as blue circles are the centroid-to-centroid image separations which are not the same as the peak-to-peak separations, although the behaviour of the latter is in concert with the image-structures seen at low frequencies (see below).

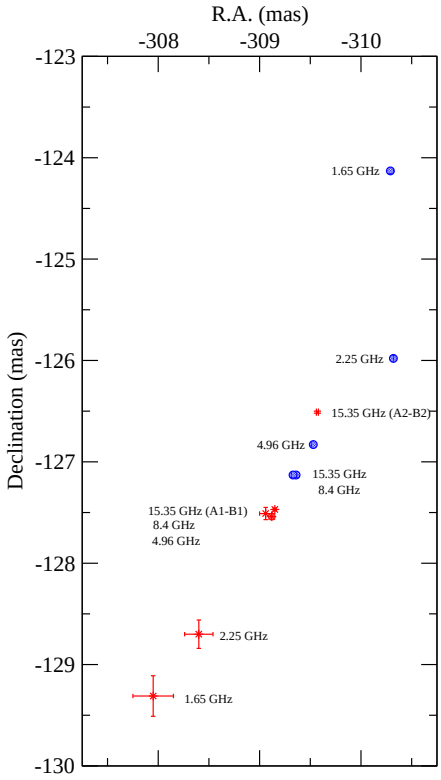

Figure 4.9: The A and B peak-to-peak separation (red cross symbols) as a function of frequency. At 15.35 GHz, separations for both the components A1−B1 and A2−B2 are marked. The A and B centroid-to-centroid separation is also shown (in blue circles) but the error bars are omitted for the sake of clarity.

4.3.4 Model fitting: subcomponents 1 and 2

The positions and deconvolved sizes for subcomponents 1 and 2 were derived by fitting elliptical Gaussians to the images at 15.35 GHz. Two AIPS tasks were used for this purpose, JMFIT and IMFIT. These tasks have very similar model-fitting procedures but use different methods for estimation of errors on the modelled parameters, though both are based on the error propagation theory for two-dimensional elliptical Gaussian fits in the presence of Gaussian noise formulated by Condon (1997). The final errorbars were derived by examining the results obtained from running both the tasks in parallel. This provides a more realistic estimate for the error bars in comparison with the formal uncertainties obtained from running only one of the tasks. The results of these fits are given in Table 4.5 and Table 4.6, along with similar measurements made by other authors.

From these measurements a few interesting comparisons can be made. First, the sizes of the subcomponents in both the images from these observations agree well with those made by Patnaik et al. (1995) at 15.35 GHz. These sizes will be used in chapter 7 in the context of scattering which may plausibly be occurring and affecting image-A properties. Second, on comparing the $(A2 - A1)$ and $(B2 - B1)$ separations at 15.35 GHz measured by authors (1) and (4) with a gap of 8 yrs between the observations and those at 8.4 GHz by authors (2) and (3) with a gap of 6 yrs between the observations, it is seen that the differences are within

Table 4.5: Deconvolved sizes and separations (Table 4.6) of components 1 and 2 obtained from fitting two-dimensional elliptical Gaussians to the images derived from these observations, and values from previous observations (the references are given in column 1). a and b are the major and minor axes of the ellipse, ϕ is the position angle of the major axis measured from north through east.

Ref.	Comp.	a	b	ϕ	S	Ratio	
		(mas)	(mas)		(mJy)	A1/B1	A2/B2
1	A1	0.52±0.02	0.25±0.01	-27.8±1.7	397±5		
	A2	1.05±0.02	0.57±0.01	-38.1±1.3	235±3		
	B1	0.26±0.03	0.15±0.05	90.2±12.5	105±6		
	B2	0.61±0.05	0.29±0.05	80 ±6.5	72±8	3.78±0.22	3.26±0.36
2	A1	1.3±0.1	0.5±0.1	-33±2	270±5		
	A2	2.3±0.1	1.2±0.1	-30±2	280±5		
	B1	0.30±0.02	0.16±0.02	83±2	114±3		
	B2	0.80±0.02	0.40±0.02	81±2	68±3	2.37±0.08	4.12±0.20
3	A1	1.90±0.3	1.12±0.3	-23±6	544±25		
	A2	≥2	≥2		223±5		
	B1	0.72±0.3	0.35±0.04	73.2±12.1	171±5		
	B2	≥0.73	≥0.73		59.9±3	3.18±0.17	3.72±0.20
4	A1	0.58±0.05	0.28±0.05	-37±5	477±7		
	A2	1.02±0.05	0.54±0.05	-47±5	291±5		
	B1	0.36±0.05	0.16±0.05	113±15	132±3		
	B2	0.61±0.05	0.23±0.05	83 ±10	80±3	3.61±0.10	3.61±0.15

Table 4.6: The peak-to-peak image and component separations.

Ref.	$A2-A1$		$B2-B1$		$B1-A1$	
	Sep. (mas)	ϕ	Sep. (mas)	ϕ	Sep. (mas)	ϕ
1	1.36±0.06	46.79±0.08	1.42±0.06	91.37±1.58	334.40±0.06	67.59±0.01
2	1.45±0.02	48.46±0.07	1.46±0.02	91.88±0.76		
3	1.47±0.04	53.4±2.5	1.50±0.05	92.3±0.6	334.19±0.06	67.61±0.02
4	1.38±0.06	51	1.47±0.06	90	334.43±0.06	67.59±0.01

1 from this data (15.35 GHz) ; 2 Biggs et al. (2003) (8.4 GHz) ; 3 Kemball et al. (2001) (8.4 GHz) ; 4 Patnaik et al. (1995) (15.35 GHz, corrected by factor 0.77)

the combined uncertainties. An upper limit on the apparent relative velocity between the subcomponents can be derived by taking an upper value of 3σ, with $\sigma = 0.08$ mas, for the shift over a period of 8 years and is $v_{|1-2|} < 0.85$ c. The same comparison can be made from the $(A1 - B1)$ separations measured by authors (1) and (4), for which the separations along R.A. and Dec. are available for both the observations, and the shifts are within $\sigma = 0.06$ mas. This translates into an upper limit of $v_{|\mathrm{A1-B1}|} < 0.65$ c. Since the subcomponent 1, the "core", is assumed to mark the base of the jet in the background AGN, which by definition is stationary with respect to the mass centre, it may be concluded that none of the components exhibit superluminal motion.

4.3.5 New structure

Shown in Figure 4.10(a) is another component in image A identified at 1.65 GHz (the peak contour in black), separated by ~ 12 mas from the superposition of components 1 and 2 (the peak contour in red) marked as 1 & 2, and at position angle $\sim -35\,^{\circ}$. The origin of this newly-identified feature (hereon component 3) is of great interest and it was investigated whether this can be part of the background source. On applying a SIEP lens model (see chapter 5), it is deduced that in image B it should be ~ 4.5 mas from component 1 as indicated in Figure 4.10(b). Unfortunately the resolution at this frequency is not enough (~ 7 mas) to resolve this separation. This can be seen by placing an additional flux-component at the expected position of component 3 in image B. The strength of this component is estimated by dividing the peak intensity of component 3 in image A, shown in Figure 4.10(c), by the relative magnification ratio at this position. On convolving this with the restoring beam, its effect can be assessed by comparing a slice[2] generated through it and the components 1 and 2 with the slice generated through the same points in the observed image. As shown in Figure 4.10(d), including another component in image B corresponding to component 3 in image A has no observable effect other than changing the centroid of the brightness distribution by a distance less than the positional uncertainty. Therefore, it cannot be distinguished whether component 3 is a distinct feature in the background source imaged in A by the smooth macro-potential of the lens, or whether it is caused by some other mechanism. The shift in the centroid position of image A at 1.6 GHz can be attributed to the existence of component 3.

Another question that naturally follows the "discovery" of component 3 is whether it is visible at 1.65 GHz only or at other frequencies as well. The colour-composite maps of image A at 2.25 GHz are shown is Fig. 4.11. The map shown in the first panel is made using a 5 mas beam corresponding to the true resolution (TR) allowed by the highest spatial frequency measured by the interferometer array, whereas the map shown in the second panel is made using a false high-resolution (FHR) of 3 mas. At the first glance at these maps it appears that component 3 is absent at this observing frequency. But a closer look reveals an elongated region of emission originating from the centre of the maps (which coincides with the superposition of the 1 and 2 core-jet components) and extending toward the north-west direction, coinciding with the direction of component 3 relative to the core emission at 1.65 GHz. There is nothing new or surprising about this elongation as it represents the tangential stretching due to lensing except it has a broad base at the origin and turns into a bottle-neck structure away from it. However, it is difficult to judge from these maps alone if this points to another maximum in the image. For further clarification, the same 'SLICE'

[2]The analysis presented here is done using the AIPS task 'SLICE' which allows one-dimensional cut of the intensity profile of an image at an arbitrary angle chosen by the user.

parameters that were used to generate the slice through the peak emission and component 3 at 1.65 GHz in image A [Fig. 4.10(c)] served as the input parameters to generate new slices in the map at the same frequency but made using a FHR of 5 mas and in the maps at 2.25 GHz shown in Fig. 4.11. These curves and also the one from Fig. 4.10(c) are shown in Fig. 4.12. A striking feature present in the curves corresponding to FHRs is a second maximum at the position of the component 3 observed at 1.65 GHz (7 mas). In fact, there is a shoulder at the same position at 2.25 GHz (5 mas) also, even though it is only slightly resolved. It is to be noted that the positions of the primary maxima, relative to the centre of the maps (0,0), are slightly different for different curves, even at the same frequency. This is attributed to the

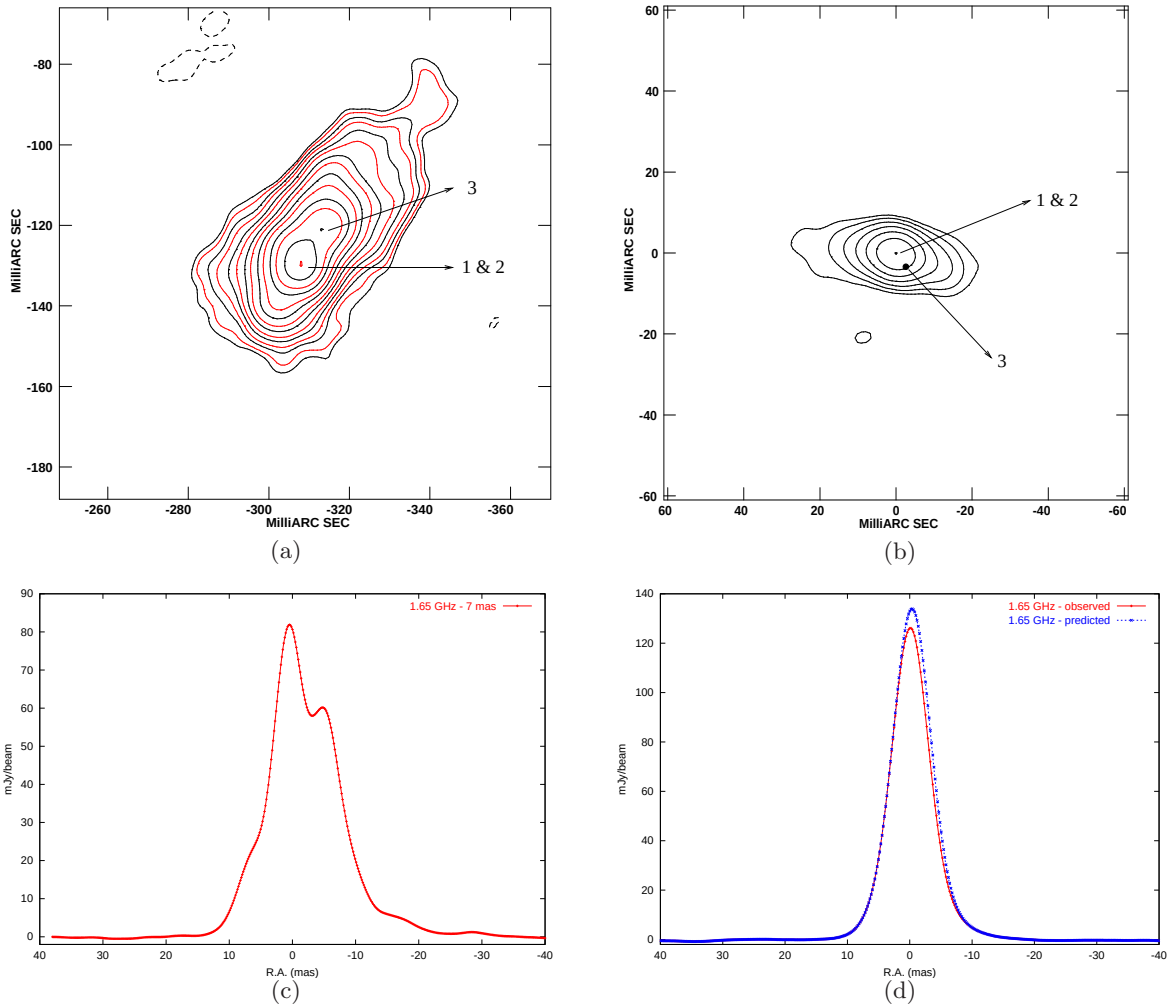

Figure 4.10: (a) Second maximum (component 3) detected at 1.65 GHz in image A at a separation of $\sim$ 12 mas from component 1 & 2. (The components 1 and 2 are not resolvable at these frequencies, hence what is marked is their superposition). (b) The predicted position of component 3 in image B at 1.65 GHz, marked as a black dot about $\sim$ 4.5 mas from component 1 & 2. The resolution at this frequency is about 7 mas. (c) A slice through the components 1 & 2 and 3 in image A. (d) The predicted (blue) and observed (red) slices through the components 1 & 2 and the expected position of component 3 in image B at 1.65 GHz.

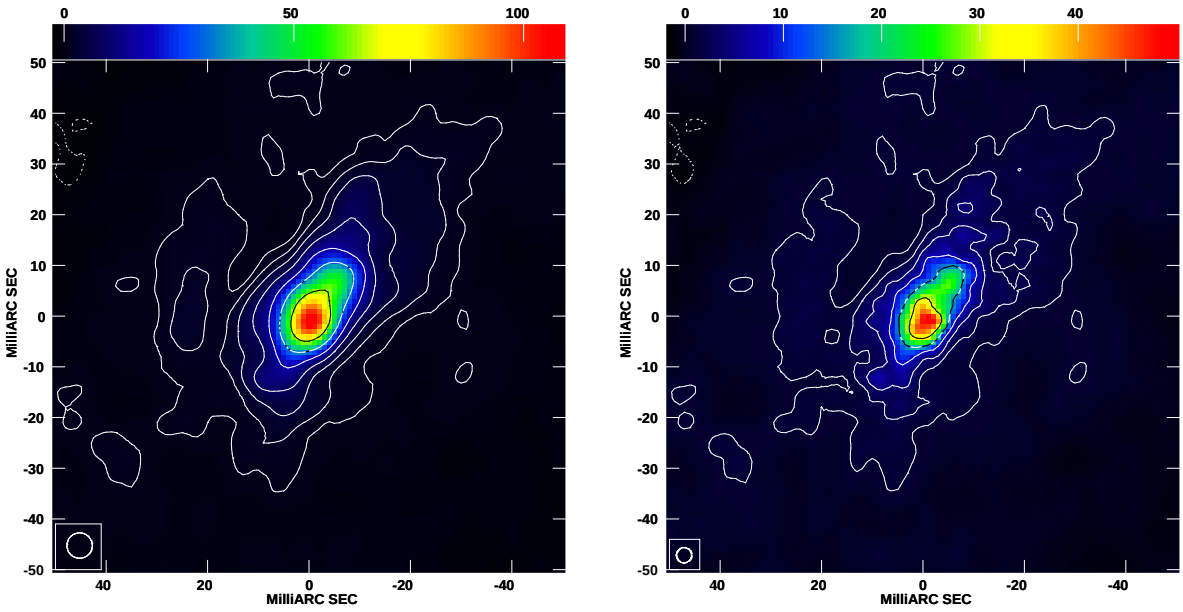

(a) (b)

Figure 4.11: A colour-coded plot of image A at 2.25 GHz with intensity contours overlaid. On the top of each map is a linear intensity wedge in mJy beam^{-1}. The contour levels are at (-1, 1, 2, 4, 8, ...) $\times$1 mJy beam^{-1}. (a) Image A map made with a normal resolution of 5 mas. (b) Image A map made with a false high-resolution of 3 mas.

different beam sizes which, when convolved with the clean components, result in a change in the centroid position. From the above analysis it is tempting to believe that component 3 is indeed present in the maps of image A at 2.25 GHz as well. Future observations are necessary to confirm this conclusion.

The results based on FHRs should be interpreted with caution since using a false-resolution, higher than permissible by the data, essentially generates *uv* visibilities that have not been measured. These newly generated *uv* visibilities might not represent the true source brightness distribution. It is important to consider the extent to which the maps made using FHRs, and the physical quantities they render, can be believed. Shown in Fig. 4.13 are slices through components 1 and 2 in the original image A (right panel) and image B (left panel), at 15.35 GHz using a TR (0.5 mas). Using the same 'SLICE' parameters, other slices are made in both the images at 15.35 GHz using a FHR (0.3 mas), 8.40 GHz using the TR (1 mas) and a FHR (0.75 mas) and 4.96 GHz using a FHR (1 mas). Again, maxima positions corresponding to components 1 and 2 (at 15.35 GHz, 0.5 mas) are well-matched by maxima seen for other curves. These are believed to correspond to components 1 and 2 beyond doubt, even though they are hardly discernable in the contour or the colour plots of the images (not shown). From the above exercise, therefore, the following statement can be made: true features are very likely to show up in slice plots of radio-images made using false high-resolutions. The same cannot be said about additional features, such as the tiny maximum that appears in between components 1 and 2 at 15.35 GHz using a FR (0.3 mas) in both the images. Additional components separated from 1 and 2 on a scale of a few milliarcseconds and non-collinear with them are extremely desirable as their separation vectors provide enough constraints for a unique determination of all four components of the two-by-two relative image-magnification

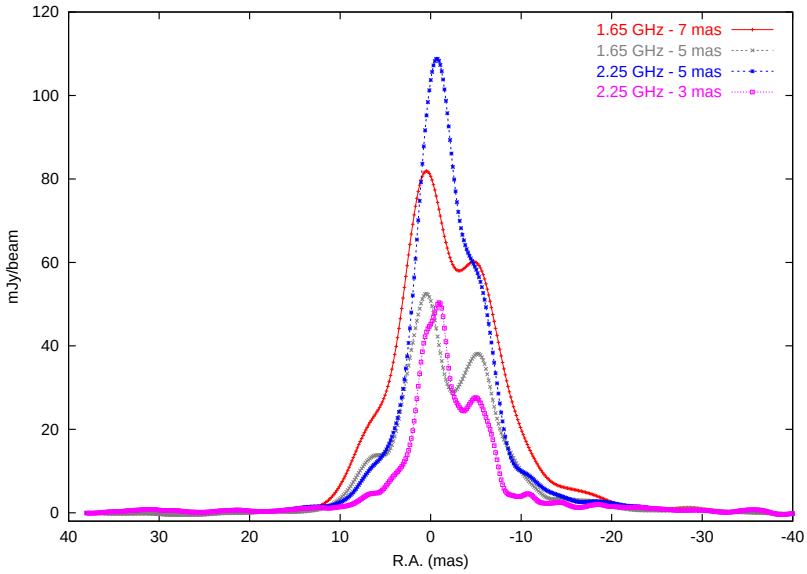

Figure 4.12: Slices made through the core-components (1 & 2) and component 3 in image A using true and false high-resolutions of 7 mas and 5 mas at 1.65 GHz and 5 mas and 3 mas at 2.25 GHz, respectively.

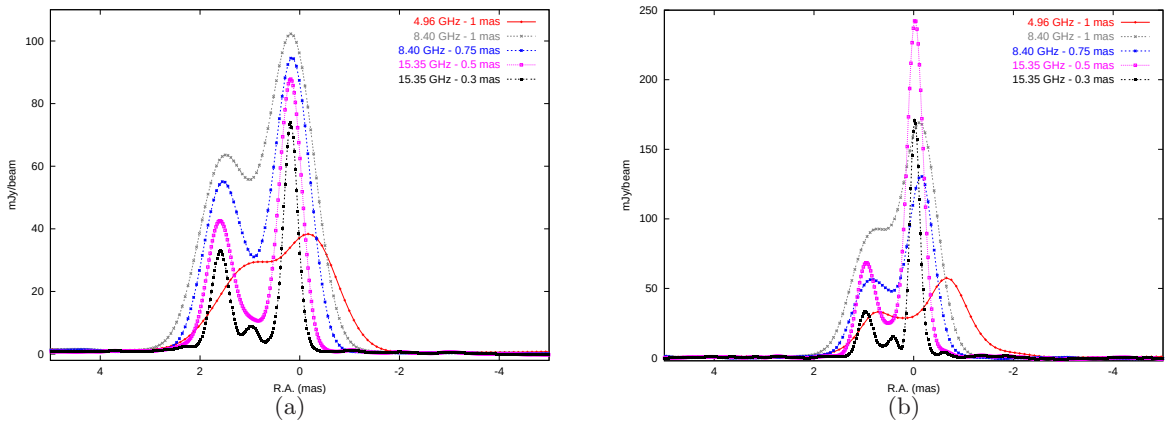

Figure 4.13: One-dimensional slices through components 1 and 2 at 15.35 GHz, 8.40 GHz and 4.96 GHz using different resolutions. (a) Image B. (b) Image A. (see text)

matrix. Even if the additional feature that appears between components 1 and 2 is assumed to be genuine (or proven so from future observations), it cannot, however, be used for this purpose as it lies almost on the line joining 1 and 2.

4.4 Conclusion

The technique of inverse phase-referencing was successfully used to investigate the frequency-dependence of the emission from the images of B0218+357; this is the first time in which a gravitational lens has been used as a phase-reference. The change in the centroid position of the image brightness distributions has been established over five frequencies, and also

the change in the positions of the emission peaks has been investigated using inter-image astrometry. The shift in the centroid in image A, which is significant ($\sim$ 3.5 mas) only at 1.65 GHz, is in a direction along which the relative magnification is predicted to be constant. In image B no significant frequency dependent shift is detected in the position of the centroid. A reasonable assumption is that the relative image-magnification at the centroid positions derived from the model gives a good measure of the expected image flux-density ratio, the accuracy of which is examined in the next chapter. Thus, it can be concluded that the changing magnification gradient across the images is not the main cause of the anomalous change of image flux-density ratio with frequency.

5 Derivation of magnification-weighted image flux-density ratios using LensClean models

The question that motivated further investigation of the frequency-dependent structure of the B0218+357 images is whether the magnification at the centroid position, $\mu(\vec{x}_c)$, gives a good estimate of the average magnification suffered by an extended object. Source regions that are mapped in pathological magnification domains, such as near critical curves, with extremely high magnifications, or near the centre of the lens-mass distribution, with extremely low magnifications, are excluded from the current analysis. For a simple source structure, then, it may reasonably and intuitively be assumed that $\mu(\vec{x}_c)$ is close to the average magnification, given by Eq. 5.1. But for complicated source structures involving steep magnification gradients in the image plane, the assumption does not hold any longer.

As can be clearly seen in Figure 4.3, at 1.65 GHz there is a large amount of low brightness emission that extends out to $\sim \pm 30$ mas. In comparison, at 15.35 GHz the emission is dominated by the compact subcomponents with a separation of ~ 1.4 mas. At lower frequencies the (larger) images extend over regions where lens models do, indeed, predict significant changes in the relative magnification, and it may be insufficient to simply consider magnifications at the centroid positions. This is because low frequency emission from different regions of the background source is magnified by very different amounts. The resultant average magnification is thus the integral of the (background source) magnification-weighted intensity over the image area.

5.1 Magnification of an extended source

The average magnification of a lensed image of an extended source is obtained by modifying Eq. 1.15 to

$$\bar{\mu}_\nu \;=\; \frac{\int\, I_\nu(\vec{y})\,\mu(\vec{y})\,d^2y}{\int\, I_\nu(\vec{y})\,d^2y}\,, \tag{5.1}$$

where $d\Omega_{\rm I} = \mu(\vec{y})d\Omega_{\rm S}$ and $d\Omega_{\rm S} = d^2y$. Here, $\mu(\vec{y})$ is not the total magnification for a point source, i.e. the sum of magnifications of all the images it is lensed into, but the magnification for only the image under consideration. Hence, $\bar{\mu}_\nu$ is the ratio of the image flux-density to the source flux-density. The frequency dependence can be attributed to the frequency-dependent source brightness distribution and structure. By applying this equation to both the images of B0218+357, the true relative image-magnification can be determined. The only hurdle in accomplishing this task is that the source intensity of a lensed object is unknown to the observer. This problem can be overcome by inverting the equation in terms of the known quantities to,

$$\bar{\mu}_\nu \;=\; \frac{\int\, F_\nu(\vec{x})\,d^2x}{\int\,[F_\nu(\vec{x})/\mu(\vec{x})]\,d^2x}\,, \tag{5.2}$$

Table 5.1: The lens model parameters derived from the LensClean algorithm (Wucknitz et al. 2004). The lens position coordinates are given relative to A1 with right ascension increasing to the left (east) and declination increasing to the north.

β	x_{01} (mas)	x_{02} (mas)	ϵ_1	ϵ_2	ξ_0 (mas)
1	255.214	117.193	0.0057	-0.0494	163.269
1.063	255.212	118.522	0.0179	-0.0410	169.020

where F_ν is the image flux-density[1] at position $\vec{x}$, $\mu(\vec{x})$ is the lens magnification at this position and the integral is carried over the entire image area. The relative image-magnification is then simply

$$\mu_{R_\nu} \;=\; \frac{\bar{\mu}_{A_\nu}}{\bar{\mu}_{B_\nu}} \;=\; \frac{\dfrac{\int\, I_\nu(\vec{x}_A)\, d^2x_A}{\int [F_\nu(\vec{x}_A)/\mu(\vec{x}_A)]\, d^2x_A}}{\dfrac{\int\, I_\nu(\vec{x}_B)\, d^2x_B}{\int [F_\nu(\vec{x}_B)/\mu(\vec{x}_B)]\, d^2x_B}}\,. \tag{5.3}$$

5.2 Lens model

To use the above recipe for estimating the relative image-magnification demands the knowledge of the lens mass-distribution so that the magnification at all image points can be derived. The lens model used for the subsequent analysis is a singular elliptical potential with the mass-radius slope, β, fixed to 1 to obtain an isothermal profile (SIEP, Sect. 1.3.2). The elliptical iso-potential form is given by Eq. 1.28. Such a model is parameterized by five parameters, the lens position, x_{01} and x_{02}, the ellipticity, ϵ_x and ϵ_y and the lens strength, ξ_0. These parameters are derived from the LensClean algorithm (Sect. 3.5.2) and given in Table 5.1.

The lens position coordinates given in Table 5.1 are relative to A1. The coordinate frame of reference adopted for the calculations, (X_1,X_2), is such that the major axis of the ellipse (the locus of points obtained with constant u in Eq. 1.29) and the X_1–axis are aligned with each other. The two frames of reference, (R.A., Dec.) and (X_1,X_2) are shown in Fig. 5.1. The ellipticity in this reference frame is

$$\epsilon \;=\; |\epsilon|\, \mathrm{e}^{2\mathrm{i}\theta} \;=\; \epsilon_1 \cos 2\theta + \mathrm{i}\, \epsilon_2 \sin 2\theta\,, \tag{5.4}$$

where

$$\tan 2\theta \;=\; \frac{\epsilon_1}{\epsilon_2} \quad ; \quad |\epsilon| \;=\; \epsilon_1^2 + \epsilon_2^2\,,$$

θ is equal to $(90\,^\circ - \phi)$, and ϕ is the position angle of the major axis of the ellipse, measured from north through east. Further, the ellipticity can be viewed as a complex number of spin two as implied by the '2' that appears in the exponent. A field or vector can be associated with an object of spin n if it returns to its original value on rotation through an angle equal to the ratio of $360\,^\circ$ to n. Hence, the same value of ellipticity is obtained when rotated through an angle of $180\,^\circ$.

The isothermality can be disturbed by varying the value of β to values around 1; the best fitting non-isothermal value of β is also given in the table. However, the procedure employed for this was not completely self-consistent. The best-fitting value for $\beta \neq 1$ was derived by

[1] The flux-density at *a position* $\vec{x}$ in the image plane, in principle, is not defined but in the following 'positions' will be identified with pixels that contain flux-densities.

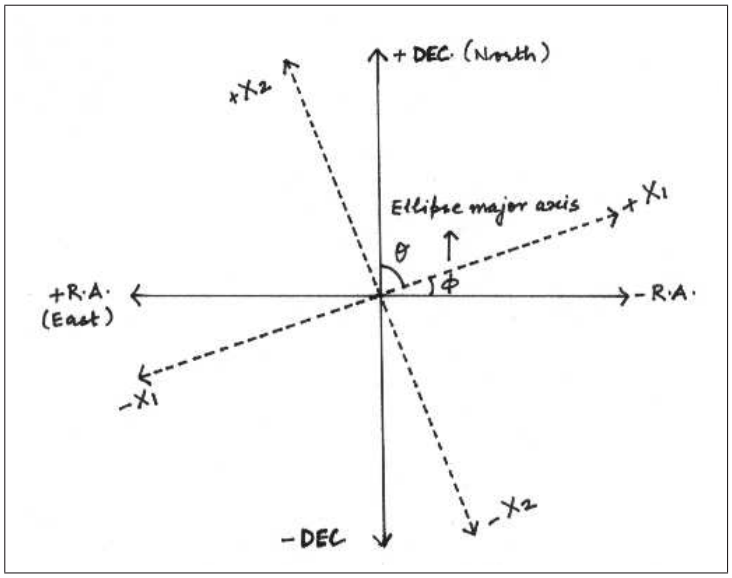

Figure 5.1: The frames of reference in which the observations are made (R.A., Dec.) and in which the lens calculations are done (X_1,X_2).

fixing the lens position determined for an isothermal model (but was allowed to vary and contribute to the total χ-square) and using the following VLBI constraints: the $(A1 - B1)$, $(A1 - A2)$ and the $(B1 - B2)$ separations, and the image flux-density ratio at 15.35 GHz.

There are two main motivations behind including non-isothermality that come from both these as well as previous observations. Firstly, using the SIEP lens model on these data, there is an evident 4 σ to 5 σ discrepancy between the observed and the modelled $B2 - B1$ component separation along right ascension (see Table 5.2). On applying the Singular Non-Isothermal Elliptical Potential (SNIEP), the $B2 - B1$ component separation falls to within 1 σ. The second clue is obtained from a qualitative comparison made by Biggs et al. (2003) between the CLEAN maps of images A and B back-projected into the source plane. The authors used the CLEAN components from their 8.4 GHz observations of B0218+357 and a classically fitted lens model[2] with the lens centre at $x_{01} = 260$ mas, $x_{02} = 177.5$ mas,

[2]The lens position was fixed at a value derived from an older version of LensClean and the other three parameters of the lens model were determined using the three radio constraints described in Sect. 3.5.2.

Table 5.2: The observed and modelled quantities at 15.35 GHz. $A1 - A2$ separation is held fixed and the modelled $B1 - B2$ separation is compared with the observed value. The observed image-separations and component-separations are accurate to within ±40 microarcseconds.

Quantities	Observed (mas)		Modelled (mas)			
			$\beta = 1$		$\beta = 1.0632$	
	R.A.	Dec.	R.A.	Dec.	R.A.	Dec.
A2 − A1	0.991	0.931	0.991	0.931	0.991	0.931
B2 − B1	1.418	-0.034	1.232	-0.054	1.417	-0.052
B1 − A1	309.147	127.471	309.147	127.472	309.146	127.471
flux-density ratio (A/B)	3.87±0.14		3.88		3.88	

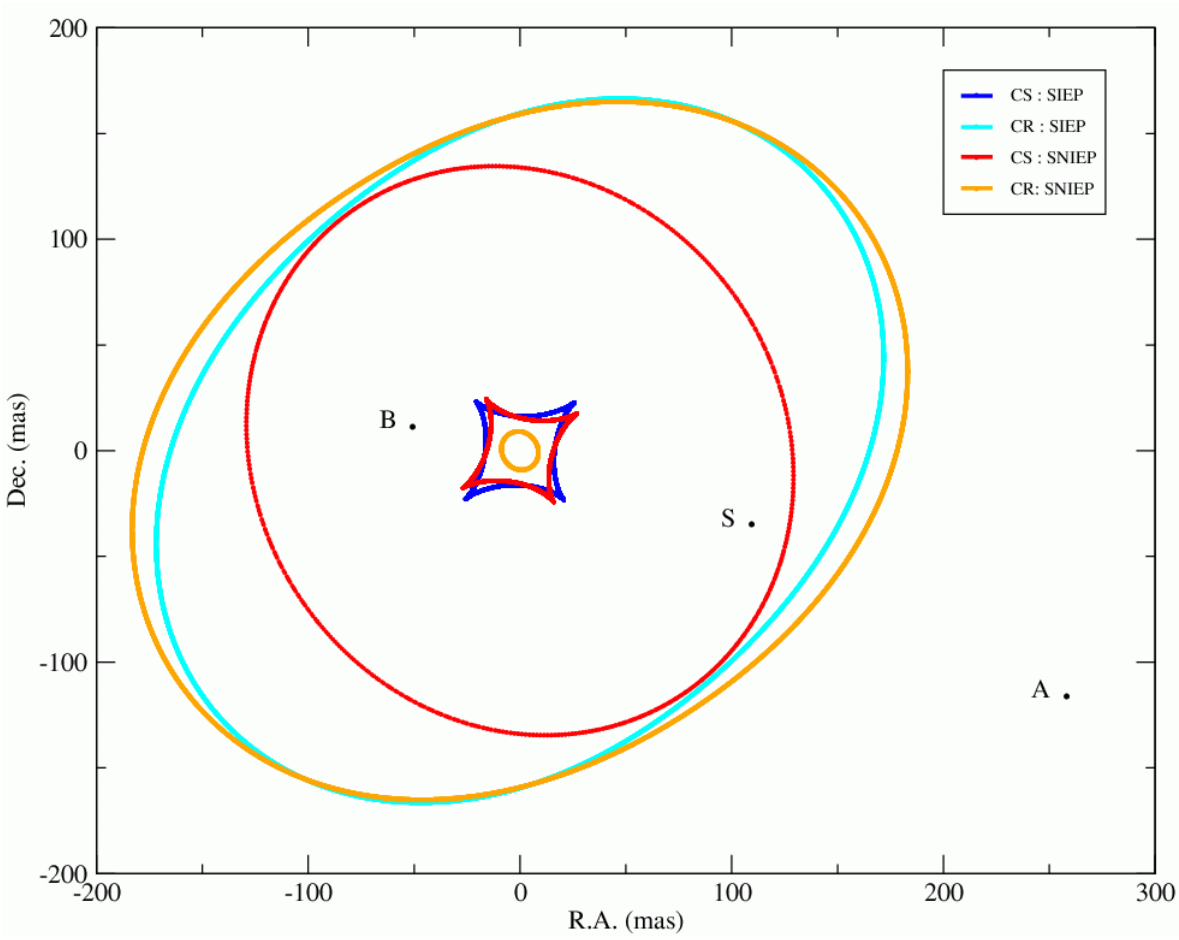

Figure 5.2: Caustics (CS) and critical curves (CR). The dark blue tangential caustic (SIEP model) is mapped into the light blue tangential critical curve. The red tangential and radial caustics (SNIEP model) are mapped into the orange tangential (outer) and radial (inner) critical curves. The 15.35 GHz positions of the images (A and B) and the source (S) are marked (see text).

which is close to the best results from LensClean. To allow easy comparison, both the images were restored with the same source-plane beam (Wucknitz 2002) to have the same nominal resolution. Though the source plane maps look very similar, there are a few non-negligible differences in their appearances. One such difference is that the B jet seems to be more elongated or stretched than the A jet by about 10 %. This dissimilarity can be resolved only by invoking a different mass-radius profile. This is because the jet in the source structure is directed almost radially towards the centre of the galaxy. The departure from isothermality needed to account for the ten percent effect is of only about 5 % or $\beta \approx 1.05$. This agrees very well with the value of β derived to improve the fitting from 4 σ or 5 σ discrepancy in the $B2 - B1$ component separation(see Table 5.2) to within 1 σ.

The caustics and critical curves for SIEP and SNIEP models are shown in Fig. 5.2. For a singular isothermal model, with a non-zero ellipticity, there is a tangential (astroid) caustic (dark blue curve in Fig. 5.2) and a pseudo-caustic (not shown), the latter representing a transition between regions where the number of images differs by one. For a SNIEP model, there are two caustics (red curves in Fig. 5.2) that are mapped into two critical curves (or-

ange curves in Fig. 5.2). An image that falls inside the radial (inner) critical curve has a positive magnification, an image between the radial and tangential (outer) critical curves has a negative magnification (image B), and an image outside the tangential critical curve has a positive magnification (image A). If the singularity at the centre is removed and replaced with a core of a finite size, an additional de-magnified image will appear close to the core.

5.2.1 Limit on the core-radius

The central image is produced only if there exists a radial critical curve, which is commonly produced by models such as a Non-singular Isothermal Sphere (NIS) or power-law profiles with $\rho \propto r^{-n}$, with an inner slope shallower than an isothermal profile, i.e. $n < 2$. In terms of β in Eq. 1.28, the power-law index for the potential, this implies[3] $\beta > 1$. The potential corresponding to a NIS model can be described as

$$\psi \propto \left[x_{\rm c}^2 + \frac{x_1^2}{(1+\epsilon)^2} + \frac{x_2^2}{(1-\epsilon)^2}\right]^{\beta/2}, \tag{5.5}$$

where $\beta = 1$ and $x_{\rm c}$ is the core-radius. Central images are suppressed if the core radius $x_{\rm c}$ is sufficiently small because then the lens model effectively converges to an isothermal profile with a singular core. Since there is no third image detected in B0218+357, this can be used to derive an upper limit to $x_{\rm c}$. Assuming that any additional image would have been detected if its peak surface brightness was greater than 3σ rms noise in the map of B0218+357 at any frequency, the 'non-detectability' of the third image can be interpreted as $\mu_{\rm c}/\mu_{\rm A} < (3\sigma/S_{\rm A})_\nu$. Here, $\mu_{\rm c}$ and $\mu_{\rm A}$ are the magnifications for the centre image and image A, respectively, and $S_{\rm A}$ is the flux-density of image A at the same frequency for which σ is evaluated. Using the measurements for $\nu = 4.96$ GHz given in Table 4.4, the above limit transforms into $\mu_{\rm c}/\mu_{\rm A} < 1.2 \times 10^{-3}$. Using the average magnification of $\mu_{\rm A} = 2.0$, this further implies that $\mu_{\rm c} < 2.3 \times 10^{-3}$. In the above, it has been assumed that the third image will be unresolved and, therefore, the upper limit to its total flux-density is 3σ. This can be verified on the basis of its strong relative de-magnification factor of ~ 1000, with respect to image A. A rough estimate of the total area of image A at 4.96 GHz is 30 mas^2 which when scaled down by a factor of thousand leads to a circular area of radius ~ 0.2 mas. This is much lower than the size of the beam at this frequency ($\gtrsim 1$ mas).

For a NIS model, it has been calculated that in order to satisfy the limit $\mu_{\rm c} < 2.3\times10^{-3}$, the core-radius can be no larger than $x_{\rm c} < 0.5$ mas. This is the upper limit on the angular radius of the finite core introduced at the centre of the lens mass distribution, which is translated into a linear size of $r_{\rm c} < 3.5$ pc at the redshift of the lens galaxy. A more stringent limit can be derived using the detection threshold based on the 8.4 GHz global VLBI maps of B0218+357 produced by Biggs et al. (2003), the rms noise level in which is much lower, $\sigma = 30$ μJy beam^{-1}. In comparison, the rms noise level in the 4.96 GHz map of image A, which has been used in the above calculations, is $3\sigma = 250$ μJy beam^{-1}. Even though their observations correspond to a different frequency, the flux-density of image A is almost the same ($\gtrsim 600$ mJy) as that at 4.96 GHz from these observations. Therefore, the upper limit to the magnification of the centre image, derived from their maps, is $\mu_{\rm c} < 3 \times 10^{-4}$. This implies that $x_{\rm c} < 0.06$ mas or that $r_{\rm c} < 0.5$ pc.

[3]If the three-dimensional mass density$\rho \propto r^{-n}$, the projected mass density goes as $\kappa \propto r^{-n+1}$. Then, from Poisson's Equation, $\kappa \propto \nabla^2\psi \rightarrow \psi \propto r^\beta$, where $\beta = (-n+3)$.

Gravitational lensing is a unique tool to probe the inner slope of the mass profiles of galaxies. There is a well-known scarcity of odd-image lens systems despite the odd number of images predicted from theoretical considerations (see Sect. 1.2 and Sect. 1.3.1). The lack of odd-image lens systems is indicative of either very small core radii, as derived in this section, or steep central profiles ($\beta < 1.0$). These results are also in agreement with the observations of early-type elliptical galaxies with the HST, which show the light distribution to be cuspy (Faber et al. 1997).

5.3 Image finding routines

The most tedious step in deriving the image magnifications is the inversion of the lens equation to solve for the image positions for a given source position. This is, in general, the most time-consuming part of analysing gravitationally lensed systems as there exist very few realistic lens models for which analytic inversion is possible. In this regard, however, lens models with elliptical iso-potential curves (as opposed to elliptical iso-density curves) are much easier to deal with (see Sect. 1.3.2). Care must be taken, though, not to have high ellipticities for the iso-potential contours because of the danger of translating them into very unrealistic iso-density curves.

Starting with Eqs. 1.34 and 1.35, the two-dimensional lens equation can be converted into the following one-dimensional form,

$$x_2 \;=\; \frac{y_2 x_1 (1+\epsilon)^2}{y_1 (1+\epsilon)^2 - (4\epsilon) x_1}\,, \tag{5.6}$$

where (x_1, x_2) is the image position of the corresponding source position (y_1, y_2). To solve for the image position, the above expression is re-inserted into either one of the two-component lens equations [Eq. 1.35] and the roots of the final equation indicate one of the position components for each image and the other component is found from Eq. 5.6.

As mentioned in Sect. 3.5.2, the general expression for the lens equation for a SIEP model that needs solving to locate the images, is a fourth-order polynomial. But since one of the image positions (the primary image) is already known, as it serves as an input to calculate the source pixel in question, the method of *deflation* can be used to convert this quartic equation into a cubic one. This step is only a simplification to ease the process of root-finding and not really necessary as the roots of polynomial equations extending up to fourth-order can be analytically found. The lens images from the resulting cubic equation are solved by employing one of the root-finding libraries provided by the GNU Scientific Library (GSL). A cubic equation has, in general, three roots. In the case where the source is outside the tangential caustic, only one of the roots is real and corresponds to either image A or image B.

For a SNIEP model, locating roots is more difficult as the lens equation is no longer a polynomial and cannot be analytically inverted. To get around the problem, the Newton-Raphson method (NR) was used, which is known to be one of the most robust and efficient routines for finding zeroes of a function, provided the function has a continuous and a non-zero derivative around the neighbourhood of a solution. For the current purpose, i.e. for regions around the observed positions of images A and B, both the conditions are satisfied. Then, using Taylor's expansion, it can be proved that, given a trial solution x_i which is in error by ϵ_i from the true solution, the next iterative trial solution x_{i+1} will be in error by an amount

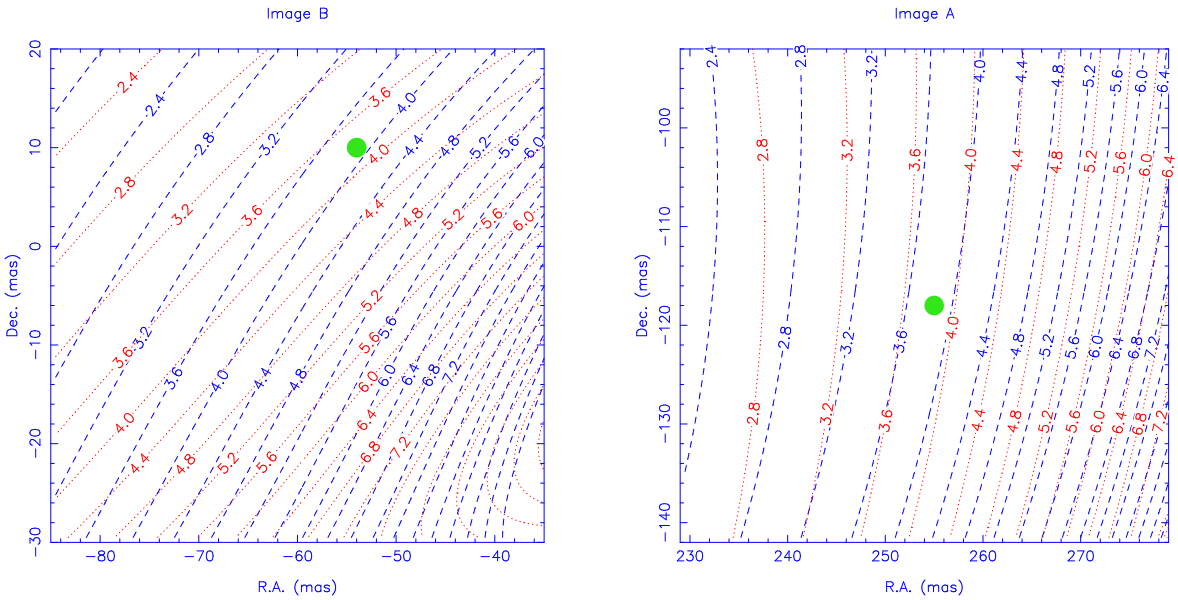

Figure 5.3: The contours of constant relative image-magnification obtained from the SIEP model (blue and long dashed) and those from the SNIEP model (red and dotted).

proportional to ϵ_i^2. From the above argument, it is clear that the rate of convergence for the NR routine is extremely strong. If the trial solution is close to the true solution, due to the above property of quadratic convergence, the accuracy of the solution doubles with each step. On the other hand, if the initial estimate is far from the true solution so that the resulting corrections are large, or surrounded by one or more local extrema so that the solution hops from one side of the zero-axis to another non-convergently, obviously the method does not work.

Once the images have been located and their magnifications calculated, the contours of constant relative image-magnifications can be determined and are sketched in Fig. 5.3. There are two sets of curves plotted; one is for the SIEP model (long dashed and blue) and the other is for the SNIEP model (dotted and red). The labels along the curves specify the value of the relative image-magnification. The green filled circles represent the 15.35 GHz positions of the components A1 and B1. The difference in these models is hardly visible around image A. Around image B, the curves do not overlap as much and this is due to the different position angles of the major axes of the ellipses, the effect of which is stronger near the lens centre.

5.4 Computation of relative image-magnification

The model-predicted relative image-magnifications at different frequencies were calculated on the basis of the observed flux-density distribution of either image A or image B (termed the primary image). The flux-density distribution of the second image was derived using either of the lens models (SIEP or SNIEP). In this section, the details of the procedure are described.

5.4.1 Selection of the CLEAN components

The maps of the B0218+357 images, A and B, used to calculate the relative image-magnification, were obtained after applying the natural weighting scheme (see Sect. 3.5) to the visibility data set. This is advantageous since the goal of this analysis is to calculate the image flux-density ratio as precisely as is possible with the data. Therefore, in the case of low-brightness and extended emission, such as the low-frequency maps of image A, it is the signal to noise ratio that needs optimization rather than the position accuracy of various components. In the case of the latter, the uniform weighting scheme is more suitable. The CLEAN components corresponding to the brightness distribution of the images were selected by enclosing the emission within a small 'tight box'. The size and position of the box were guided by the contour plots of the images shown in Fig. 4.3. This can result in one of the following two things. First, there is a well-known problem that occurs during the execution of the AIPS task 'IMAGR' (Sect. 4.2.3) used for CLEANing of the images, in that after a few number of clean iterations the algorithm starts to accumulate negative components. Although these negative components are unphysical and do not represent any real features in the source (image) brightness profile, they are needed to compensate for components whose flux densities have been over-estimated in the earlier steps of CLEAN and to attain convergence. However, these negative components need not necessarily reside in regions describing the true structure of the source and are usually scattered all over the cleaned maps. Thus, it may well be that by not including the entire CLEAN'ed field around the main emission regions results in an over-estimation of the flux density integrated within the box. Second, in the case where the images are described, in most part, by a few compact components but lie in a bed of low brightness emission accounting for only a few percent of the total flux-density, summing of emission in a region constrained by a compact 'tight box' might result in an under-estimation of the total image strength.

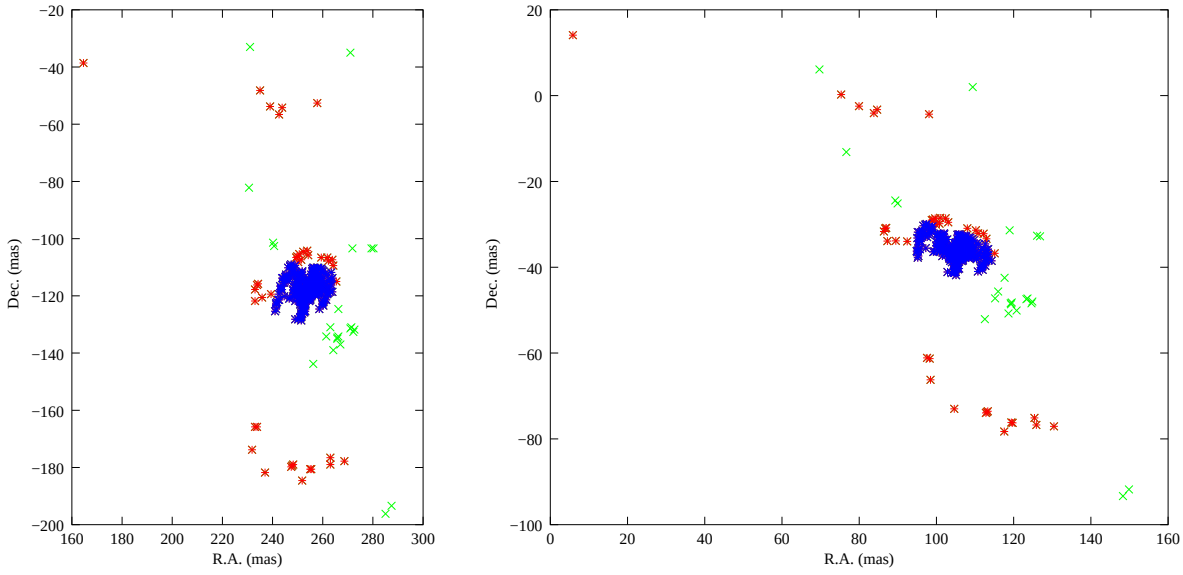

Figure 5.4: Image A CLEAN components in the image plane (left) and back-projected into the source plane (right) at 4.96 GHz. The lens plane and the source plane are not commensurate with each other in scale.

Table 5.3: The flux-density estimations from various techniques. The error bars on the JMFIT results are only tentative estimates derived from the rms in the image, while those on IMSTAT results are by varying the window size and examining the spread in the values. For JMFIT, the high-resolution CLEAN components were convolved with a low-resolution beam. The latter is given in parenthesis. The 'tight box' corresponds to adding up all the high-resolution CLEAN components within a 'tight box' around the emission, the values in parenthesis are with negative components.

ν (GHz)	JMFIT		IMSTAT		CC		'Tight Box'
	Beam	S	Beam	S	Beam	S	S
	(mas)	(mJy)	(mas)	(mJy)	(mas)	(mJy)	(mJy)
1.65							
A	7, 12 (50)	504^{12}_{12}, 496^{1}_{1}	7, 12	501^{6}_{6}, 509^{5}_{5}	7, 12	509, 513	493 (491)
B	7, 12 (50)	245^{1}_{1}, 250^{5}_{5}	7, 12	246^{2}_{2}, 254^{6}_{6}	7, 12	247, 260	238 (238)
2.25							
A	5, 12 (50)	628^{1}_{1}, 647^{9}_{9}	5, 12	630^{4}_{4}, 647^{1}_{1}	5, 12	635, 648	620 (620)
B	5, 12 (50)	236^{1}_{1}, 245^{8}_{8}	5, 12	236^{1}_{1}, 241^{3}_{3}	5, 12	235, 239	229 (229)
4.96							
A	2, 6 (30)	644^{1}_{1}, 646^{9}_{9}	2, 6	641^{2}_{2}, 650^{1}_{1}	2, 6	643, 650	640 (637)
B	2, 6 (30)	214^{1}_{1}, 244^{6}_{6}	2, 6	214^{1}_{1}, 216^{1}_{1}	2, 6	215, 218	213 (213)
8.4							
A	1, 4 (10)	673^{3}_{3}, 680^{50}_{50}	1, 4	675^{3}_{3}, 681^{5}_{5}	1, 4	679, 683	668 (668)
B	1, 4 (10)	194^{1}_{1}, 203^{38}_{38}	1, 4	199^{1}_{1}, 210^{5}_{5}	1, 4	201, 214	196 (196)
15.35							
A	0.5, 2 (5)	667^{3}_{3}, 666^{30}_{30}	0.5, 2	666^{12}_{12}, 667^{12}_{12}	0.5, 2	672, 672	661 (661)
B	0.5, 2 (5)	166^{1}_{1}, 171^{3}_{3}	0.5, 2	164^{15}_{15}, 168^{1}_{1}	0.5, 2	165, 171	165 (165)

The 'tight box' method has an advantage in the present scenario that masks the effects of these drawbacks. The negative components, which get accumulated during the deconvolution of the true brightness profile from the dirty beam, are usually thrown randomly over the maps and can lie in regions of high image-magnifications. Therefore, including them can lead to very unrealistic lensed source-structures and improper estimations of the lensed source-brightness-distribution. This is true also for the spurious positive components that result from errors in the deconvolution process and amplitude calibrations. Shown in Fig. 5.4 are the CLEAN components corresponding to image A at 4.96 GHz in the image plane (left panel) and back projected into the source plane using the isothermal model corresponding to $\beta = 1$ in Table 5.1 (right panel). Plotted in blue are the CLEAN components chosen only from within a box placed in the close vicinity of the emission at the centre. The negative components are not included. The red points correspond to the positive CLEAN components the green points to the negative CLEAN components outside of the box. It is visible from the image plane distribution of the CLEAN components that the red points (positive components) that are disjoint from the central emission are distributed symmetrically about the centre of the map hinting at the corrupting effects of the sidelobes of the dirty beam. The negative components are relatively less structured, but as mentioned earlier, do not represent the true source structure and after mapping them into the source plane, they lie at regions that are definitely not connected with the true source brightness distribution.

To check against either of the two possibilities mentioned above, the flux densities of the

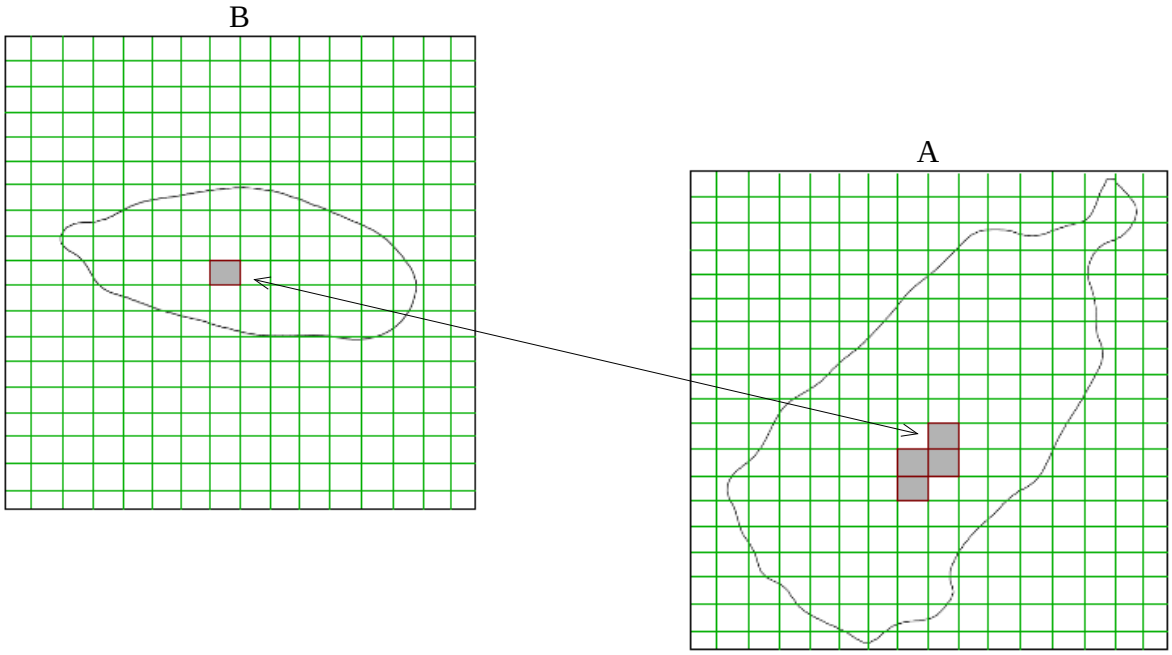

Figure 5.5: The B0218+357 images, A and B extracted from AIPS in pixel format. One pixel (subpixel) of B corresponds to more than one pixel (subpixel) in image A. The contours represent the approximate shapes of the images at 1.65 GHz.

images estimated using various methods were compared to the values obtained from integrating the emission within the 'tight box'. One method was using the AIPS task 'JMFIT' (see Sect. 4.3.4) to fit elliptical Gaussians to images obtained from convolving the CLEAN components with a big restoring beam. The other was using 'IMSTAT' to integrate the emission within a bigger box using both low-resolution beams as well as high-resolution beams (similar to the method used to estimate the image flux-densities given in Table 4.4). The third method comprised adding up all the high-resolution CLEAN components (CC) in the list created after running 'IMAGR'. The CLEAN components for this analysis ('tight box' in Table 4.4) were obtained from the high-resolution (or full-resolution) maps of images A and B. From the table it is seen that the flux densities estimated by putting a 'tight box' are less than the average of the values determined from the other three techniques by 2 % to 5 % at all the frequencies. But the ratios of the image flux-densities are the same to within 3%. These differences and losses in the image flux-densities should be compared with the (negative) effect of including spurious negative or positive components at arbitrary locations in the maps, which would lead to comparable errors in computing the source flux-densities (denominator of Eq. 5.2) at different frequencies.

5.4.2 Mapping the secondary image

The CLEAN components of the primary image were extracted from AIPS in the pixel format and decomposed into even smaller units. The rationale behind the analysis that follows next is that, since the images A and B are replicas of the same background source, the LensClean models can be used to calculate the image magnifications and their ratios at different frequencies, and to compare these ratios with the observed ones. Fig. 5.5 shows

mapping of one image (the primary image) into the other (secondary image). The total flux-density of the secondary image is computed by calculating the contribution of each element of the primary image, using a model, to the secondary image flux-density and summing them up. The pixels, each of which hosts a delta CLEAN component at its centre, are divided further into subpixels ranging from 5 to 30 in number depending upon the frequency. Using Eq. 5.6 and the image-finding algorithms described in Sect. 5.3, for every one of the subpixels in the primary image the corresponding subpixels in the secondary image are located. Generally, the secondary images do not lie exactly at the grid points but since the grid is finer than the Nyquist frequency by a factor of several tens, all secondary image positions falling into a pixel are assigned to the same grid point at the pixel center. The level of inaccuracies introduced due to rounding off of the secondary image positions to the nearest grid point can be evaluated by changing the number of subcells (N) into which the CLEAN pixels are further divided, and was found to be negligible beyond certain values of N on the order of 5 to 10.

Since image A is brighter (more magnified) than image B, each pixel in image B will point to more than one pixel in image A. In such a case, where more than one pixel in either image correspond to only one pixel in the other, the normalization of flux is essential while calculating the flux density of the corresponding secondary image pixels. For example, if image B is assumed to be the primary image in Fig. 5.5 and one pixel of image B corresponds to four pixels in image A, each of these four pixels is attributed a flux density equal to a quarter of the flux-density contained in the pixel in consideration in image B times the ratio of the magnification at the pixel in image A to the magnification at the pixel in image B.

5.5 Results

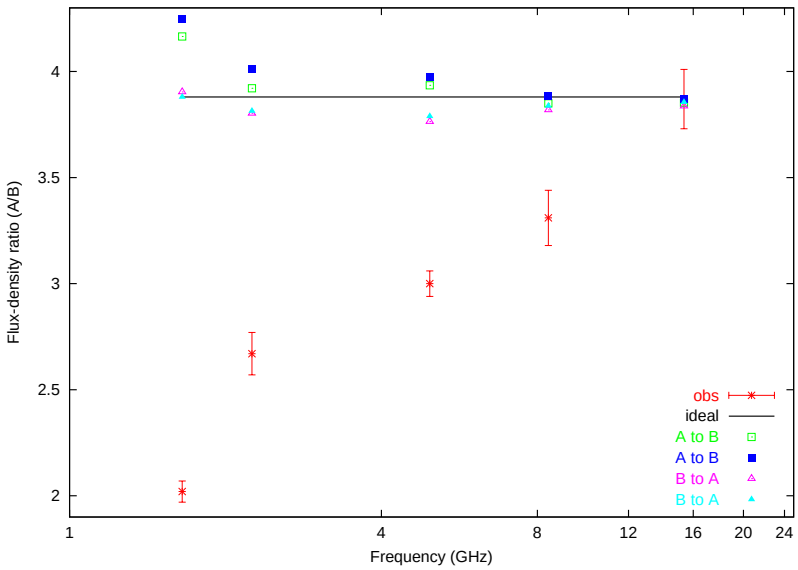

Figure 5.6: The image flux-density ratio calculated from the LensClean models. The open square and triangle symbols correspond to the results from the isothermal fitting and the filled square and triangle symbols correspond to the results from the non-isothermal fitting. The star symbols (red) are the observed image flux-density ratios.

The results from the detailed analysis of the radio maps of the two images of B0218+357, A and B, and from applying the LensClean lens-models are shown in Fig. 5.6. The line parallel to the x–axis is the ideal expectation of the image flux-density ratio of a background point-like source at the position of A1 (or B1) at 15.35 GHz, depicting the frequency-independent nature of the gravitational lensing effect. The model-predicted ratios for the isothermal and non-isothermal mass-radius profiles are shown as open and filled symbols, respectively. The square symbols are used when image A is taken as the primary image and the triangle symbols are used when image B is taken as the primary image. Also shown as red 'stars' are the image flux-density ratios calculated from the multi-frequency observations (Table 4.4). As can be seen, for all four model-predictions the ratio remains the same to within < 4 % except for 1.65 GHz using A as the primary image, where the ratio differs from a point-source model by about 8 % for the isothermal model and 10 % for the non-isothermal model. Furthermore, the change in the ratio due to the shift in the centroid position in image A at 1.65 GHz, as derived from the phase-reference observations in chapter 4, is less than a percent.

5.6 Conclusions

This detailed analysis of the effect of the interaction of frequency-dependence source structure with macro-model magnification gradient confirms that this cannot be the cause of the observed ν–dependent image flux-density ratio in B0218+357.

This analysis also shows that the relative image-magnification estimated from applying the entire structure of image A at 1.65 GHz is significantly different from when the image-A centroid position at the same frequency is directly applied to the model. It is to be noted that, even though the above 8 % to 10 % effect on the ratio is compatible with the values of relative image-magnification in the direction of the component newly-identified only in image A (Sect. 4.3.5), this is in a direction in which the relative image-magnification increases, opposite to the declining trend observed at decreasing frequencies. Finally, there can be departures from the general notion that the phenomenon of gravitational lensing preserves the spectrum of the background source in all the images. This can be seen as small deviations of the relative image-magnifications at any given frequency relative to the neighbouring frequencies in Fig. 5.6. This has been proven based on the frequency-dependent radio structure of the background source in B0218+357 and without invoking any other external mechanisms, some of which are described in the following chapters.

6 Small-scale gravitational perturbations

The joint effect of a frequency-dependent source structure and a varying gradient in the relative image-magnification in the image plane, derived on the basis of a lens macro-model only, does not produce any significant changes in the image flux-density ratio with frequency (chapter 5). Small-scale mass substructures, which perturb the image magnifications on scales of milliarcseconds can, however, introduce even stronger varying gradients in the relative image-magnification. The interplay between these small-scale perturbations and the frequency-dependent source structure may, then, reproduce the observed trend in the flux-density ratios in B0218+357.

In the framework of gravitational lensing, image flux-density ratios that fail to obey certain universal laws predicted by simple lens models are termed 'anomalous flux-ratios'. The ubiquity of lens systems with anomalous flux-ratios has drawn considerable attention in the last seven years, starting from the investigation by Mao & Schneider (1998) of the discordant image flux-ratios found in the four-image gravitational lens B1422+231. They pointed out for the first time that, whereas lensed image-positions can be reproduced to match the observed ones by any of the generic lens models (which are mostly isothermal ellipticals and variants) with remarkable agreement, the image flux ratios are rather difficult to fit and in some cases impossible. At present, the number of lens systems[1], including B0218+357, that form case studies of anomalous image flux-ratios in the radio and/or the optical, has increased to $\gtrsim 15$. All systems in this sample, except for B1600+434 and B0218+357, are four-image systems (or include multiple sets of four-images such as the ten-image lens B1933+503), for which there exist two model-independent relations between magnifications of images produced by sources within and close to the tangential caustic. These relations are schematically sketched out in Fig. 6.1 (Chiba 2002). In the first case, if the source is close to the cusp of the astroid shaped caustic, a singular lens model produces four images, three of which are highly magnified and clustered on one side of the lens. The fourth image is close to and on the other side of the lens and suffers high de-magnification due to high surface mass-density. In this scenario, the sum of the magnifications of the outer two images (with positive parity) of the three bright images equals the magnification of the third image (with negative parity). This is shown in Fig. 6.1a, where A, B and C are the three bright images. In the asymptotic regime, $r_1 = \mu_A + \mu_B + \mu_C/(|\mu_A| + |\mu_B| + |\mu_C|) \approx 0$. The second case is shown in Fig. 6.1b, wherein a source close to a fold produces two bright images A1 and A2 of equal and opposite parity, with $r_2 = |\mu_{A1}|/|\mu_{A2}| \approx 1$.

Anomalous flux-ratios observed in gravitational lenses, by and large, refer to cases where there is a significant violation of these laws predicted by a smooth gravitational potential. The

[1] B0128+437, Phillips et al. (2000); HE 0230−2130, Wisotzki et al. (1999); MG0414+0534, Turner et al. (1989); HE 0435−1223, Wisotzki et al. (2002); B0712+472, Jackson et al. (1998); HS 0810+2554, Reimers et al. (2002); RX JO911+0551, Bade et al. (1997); PG 1115+080, Weymann et al. (1980); B1359+154, Myers et al. (1999); H1413+117, Magain et al. (1988); B1422+231, Patnaik et al. (1992b); B1555+375, Marlow et al. (1999a); B1600+434, Jackson et al. (1995); B1608+656, Myers et al. (1995); B1933+503, Sykes et al. (1998); B2045+265, Fassnacht et al. (1999); Q2237+030, Huchra et al. (1985).

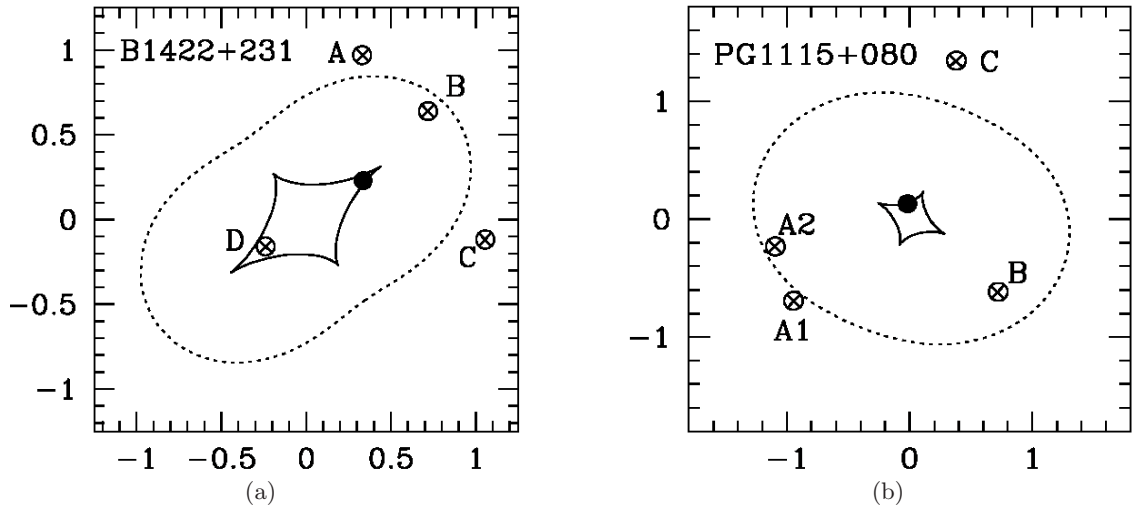

Figure 6.1: Cusp and fold relations for sources inside the tangential caustic (Chiba 2002). (a) A source close to a cusp produces three bright images A, B and C such as seen in B1422+231. For such a lens geometry, the cusp relation states that $r_1 \approx 0$. (b) For a source close to a fold, two bright images A1 and A2 of equal and opposite parity are produced, and $r_2 \approx 1$. PG1115+080 shows a similar geometry but the observed flux ratios violate this equality (see text for definitions of r_1 and r_2).

initial analysis of the flux-ratio anomalies in B1422+231 by Mao & Schneider (1998) showed that including mass perturbations or substructures with surface mass-density on the order of 1 % of the critical surface mass density of the lens galaxy can potentially reproduce the observed flux ratios. The fact that neither globular clusters nor luminous dwarf galaxies are able to produce changes in flux-ratios at any significant probability (Mao & Schneider 1998; Chiba 2002), has led many to firmly believe in the Cold Dark Matter (CDM) subhalos as a promising candidate for the required perturbations. Semi-analytic and numerical simulations based on the CDM structure formation unequivocally over-predict the fraction of galaxy masses in the form of substructures in the mass range 10^6 $M_\odot$ to 10^9 $M_\odot$ (e.g. Klypin et al. 1999; Moore et al. 1999) by an order of magnitude. Numerous solutions have been proposed to resolve this discrepancy by either altering the nature of dark matter to reduce the predicted fraction of low-mass haloes or by invoking mechanisms that destroy the baryon content or prevent star-formation in these structures to keep them dark (Bullock et al. 2000; Spergel & Steinhardt 2000; Colín et al. 2000). In the case of the latter, GL provides a powerful technique for revealing their existence. Substructures along the line-of-sight will lead the image magnifications to deviate from values dictated by simple macro-lensmodels. Anomalies in image flux-density ratios seen in numerous galaxy-scale GL are highly indicative of such missing small-scale power (e.g. Dalal & Kochanek 2002). But, as argued by Koopmans et al. (2003), Kochanek & Dalal (2004) and Mao et al. (2004), before jumping to any conclusions in favor of CDM halo models, a careful disentangling of gravitational (milli- and micro-lensing) and propagation effects (extinction, scattering, free-free absorption) is necessary.

6.1 'Milli' and 'micro' lensing

When perturbations to the macro-potential of the lens are caused by CDM subhalos, the phenomenon is known as milli-lensing and when caused by foreground stars (in the lens galaxy), the phenomenon is called micro-lensing. The prefixes (to the root word lensing), 'milli' and 'micro', reflect the characteristic angular scales of deflection caused by the perturbers in question. Since the underlying principle of both these phenomena is gravity, the perturbations in the properties of the lensed images due to either milli- or micro-lensing share the same qualitative features. Detailed calculations have shown that the magnification probability distributions for saddle-point images (with negative parity) and images corresponding to the minima of the Fermat potential (minima-images) are different, with the implication that saddle images are more susceptible to de-magnification. Additionally, the distribution is seen to be broader for brightest images (both minima as well as saddle images), making the effects of substructures more easily discernible in bright images (Chiba 2002; Dalal & Kochanek 2002; Keeton 2003; Kochanek & Dalal 2004).

The differences in the effects due to CDM subhalos and stars can be attributed to the different mass or length scale of the intervening perturber. First, in regards to relative motions between the background source, the lens and the observer, it is estimated that the flux density of the images undergo variations on time-scales proportional to the square root of the mass of the lens (for the present case the mass of the perturber). Hence, whereas the typical time-scale of flux-density variations due to solar-mass stars is in the range 1 yr to 10 yr, for subhalos in the mass range of $10^4\ M_\odot$ to $10^9\ M_\odot$ the time-scale is commensurately increased by a factor 10^2 to 10^4 (Schechter & Wambsganss 2002; Kochanek 2004). The time-scale of variations thus, in principle, gives away the nature of the disturbance. Second, the deflection angle due to an intervening star in the lens galaxy is on the order of a few microarcseconds while for subhalos it is milliarcseconds. Lensed radio sources have relatively much bigger emitting-regions; therefore, large and long-lived variations in their radio flux-densities are not expected to be due to micro-lensing. The nucleus of optical emission of lensed images, on the other hand, is comparable to the Einstein angle of stellar mass objects. Consequently, sources which suffer from micro-lensing are usually likely to be noticed in optical observations. For the flux-density ratio anomalies observed in B0218+357, due to the large radio size of the continuum-emitting region of the background source (> 1 mas), the above discussion implies that micro-lensing effects are negligible. Milli-lensing due to low-mass halos associated with the lens galaxy or clumps along the line-of-sight at arbitrary redshifts (Keeton 2003), on the other hand, can produce non-negligible magnification changes in the images but only for a certain range of source size relative to the perturber. It is the observed frequency-dependent source size of B0218+357 which introduces a mechanism whereby milli-lensing can create a ν–dependent image flux-density ratio. Furthermore, this mechanism entails astrometric shifts in the centroid of brightness distribution of the radio images A and B, which can be easily detected with high-resolution VLBI observations.

6.1.1 A brief analysis

Unfortunately, all studies conducted so far have concentrated only on four-image lens systems with a typical fold or cusp configuration. A similar analysis for B0218+357 is beyond the scope of this thesis, although some qualitative interpretations can be made based on a few general principles which are derived from detailed substructure-analyses of other systems.

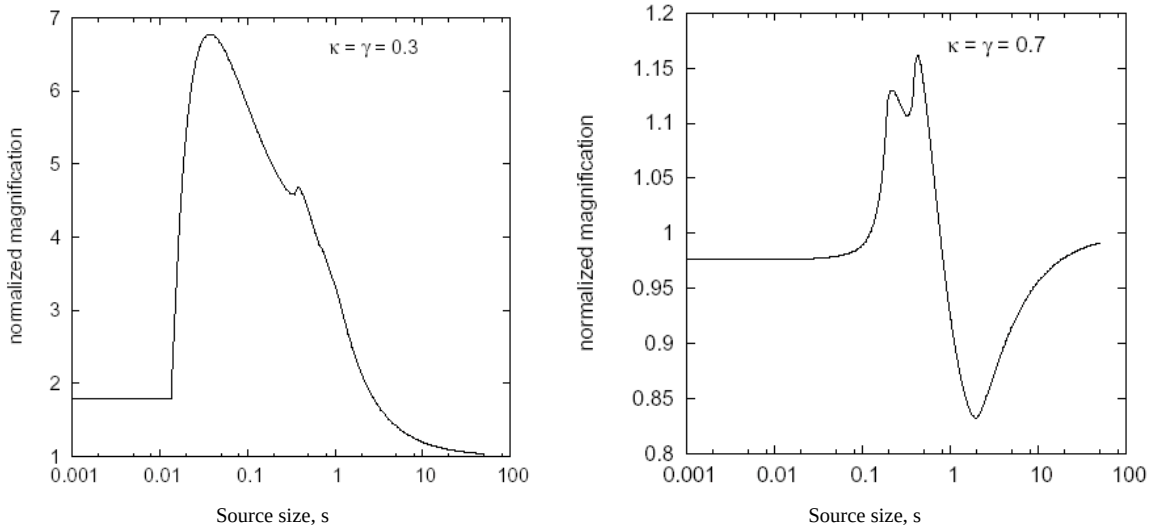

Figure 6.2: Normalized magnifications of a positive-parity (left panel) and a negative-parity (right panel) image as a function of source size, s, in units of the Einstein radius, ξ_c, of the subclump (Dobler & Keeton 2005). The source is at $(0.2, 0.6)$ relative to the position of the clump.

Shown in Fig. 6.2 are the effects of substructure on the magnification of an image that is directly behind the clump, analysed by Dobler & Keeton (2005). The clump is modelled as a SIS with Einstein radius ξ_c. The magnification due to the combined system (macro-model and the clump) normalized with respect to the magnification due to the macro-model alone, is calculated as a function of the source size, s, in units of ξ_c. For a positive parity image (left panel), the magnification differs significantly from the unperturbed value for $s \lesssim 3$ and slowly retreats to it with increasing source-size. But even for large source size ($s \sim 50$), the change in magnification is on the order of ~ 3.7 %. Further, from their calculations it appears that a positive parity image is always magnified by isothermal clumps. For a negative parity image (right panel), the most prominent distinction is relative de-magnification for most source positions and source sizes. For large s (~ 50), the effect of substructure can still be felt at the one percent level. The property of declining curves for large source-size is equivalent to the perturber being too small relative to the source-size to cause any significant changes in the magnification given by the macro-model.

To get an idea of the numbers involved for B0218+357, a clump of mass 10^8 $M_\odot$ has a corresponding Einstein radius of ~ 8 mas at the redshift of the lens galaxy ($z = 0.685$). Also, with a change in frequency from 15.35 GHz to 1.65 GHz, the radio image-sizes increase by a factor 30. The lower limit to s can be derived from the image-sizes observed at 15 GHz. A rough estimate of the total extent of image A (including both the subcomponents) at 15 GHz is ~ 1.3 mas. This is the equivalent circular radius of the deconvolved ellipse fitted to the entire image. For a rough translation of a measured size in the image plane to its true size in the source plane, the following recipe is used. Consider a small elliptical background object with a' as the major axis and b' as the minor axis of the ellipse. Let the major axis be aligned with the direction of the tangential magnification. Then, for an isothermal mass profile, the source will be lensed into an elliptical image of size $\sqrt{(\mu a') \times b'}$, where μ is the tangential magnification (the radial magnification for an isothermal mass profile is unity). Equivalently, if an image-component has a size of $\sqrt{a \times b}$, its equivalent size in the

source plane is $\sqrt{(a \times b)/\mu}$. For image A, the rough value of the tangential magnification over the region of its extent in the image plane is ~ 2. It is assumed that the 15.35 GHz image flux-density ratio (~ 3.87) is close to the true value, i.e. the magnification obtained only from the macro-model. Thus, for a mass-clump of 10^8 $M_\odot$ (10^6 $M_\odot$), a lower limit of $s \sim 0.12$ ($s \sim 1.2$) is yielded. Now, from the observed image flux-density ratios given in Table 4.4 it is clear that the ratio (A/B) changes rather continuously and decreases with increasing wavelength. Also, while the flux-density of image B increases steadily with λ, the flux-density of image A remains constant with λ and exhibits a sharp drop at 1.65 GHz. Remembering that image A has a positive parity (left panel of Fig. 6.2) and image B has a negative parity (right panel of Fig. 6.2), it may be concluded that the magnification of image A due to the presence of the clump is very unlikely to remain constant and then abruptly decline at the lowest frequency with increasing source-size and, thus, decreasing frequency as required from the observations. Similarly, starting from the unperturbed value of 1, it does not seem possible for image B magnification to rise continuously with increasing wavelength. Moreover, the total magnification of a positive-parity image, even for extremely small source sizes, is always different from 1. In other words, at frequencies higher than 15 GHz also, the relative image-magnification does not correspond to the unperturbed value.

6.2 Discussion

The above speculations are made based on the assumption that the ratio observed at 15 GHz is the value predicted by the macro-model. But if this assumption is relaxed and the true, unperturbed ratio is assumed to correspond to the value obtained at 1.65 GHz instead (2.5), it might be possible to reproduce the observed frequency-dependent trend in the image flux-density ratios. However, in that case the Einstein ring cannot be fitted using the LensClean algorithm (Wucknitz, private communication). Variations in the image magnifications by more than 5 % from their respective values, which give a ratio of 4, are followed by a substantial increase in the residuals. Thus, the above approach of adopting a value of the image flux-density ratio that is observed at lower frequencies is not in accordance with the optimal lens model. There is an inconsistency in the above argument in that the mass distribution can be different from the assumed SIE (singular isothermal elliptical) profile but the fact that the SIE fits so well with the observed flux-densities gives some evidence against the presence of substructure.

Lastly, it is also predicted that the CDM mass-clumps around the lensed images produce astrometric shifts in the centroid of the image brightness-distribution, typically on the order of several Einstein radii of the subclump (Chiba 2002; Dobler & Keeton 2005). For masses of subhalos in the above range, this implies changes on the order of a few to even ten milliarcseconds. Moreover, the effect of substructure on astrometric image-positions changes as the source size increases with wavelength. Thus, multi-frequency observations are best-suited for providing evidence of substructure. From the above brief analysis, even though CDM-substructure seems to be an unlikely cause of the observed discrepant flux-density ratios, the image peak-to-peak separation *does* show an anomalous shifting at lower frequencies by about ~ 2 mas (see Sect. 4.3.3). Therefore, the substructure hypothesis cannot be ruled out either. It must be realized that for a two-image lens system the substructure effects are especially difficult to examine because of the severe shortage of constraints. In principle, a distribution of CDM-subclumps around one or both the images within a certain range of masses can re-

produce any observations comprising image-positions and flux-ratios. But such a solution is not be unique because in such a case the number of model parameters exceeds the number of constraints as obtained from observations. For future studies, one way of analysing the substructure hypothesis in B0218+357 further is by fixing the macro lens-model to the one obtained from the LensClean algorithm and generating random realizations of substructures (Dalal & Kochanek 2002) based on analytic approximations of substructure statistics.

7 The effects of interstellar medium (ISM): non-gravitational effects

The intervening matter along the line-of-sight to the gravitationally lensed images can (through electromagnetic or non-gravitational effects) produce deviations in the image properties. Emission from the background source can be absorbed and/or scattered causing a change in the original radiation intensity. These mechanisms, in combination with the resolution of the observations, can affect the surface brightness of the lensed images differently and perturb the image flux-density ratio from its expected value. The most common physical processes that occur are extinction in the optical region, and free-free absorption, scatter-broadening and Faraday rotation in the radio region. It is generally assumed that these mechanisms occur in the ISM of the lens galaxies and, when they occur, cause the lens to be no longer 'transparent'. It is to be noted that whichever mechanism/s is responsible for the flux ratio anomaly in B0218+357, it should explicitly produce a frequency-dependent change in the image flux-density ratios, as observed. The physical quantity which appears in these above-mentioned astrophysical processes and which induces this ν–dependence is the refractive index of the intervening plasmas. In this chapter, the effects of a plasma, such as free-free absorption (Sect. 7.2) and scattering (Sect. 7.3), on the properties of the B0218+357 images are investigated.

7.1 Differential extinction in B0218+357

Extinction due to ISM includes both absorption and scattering of light by interstellar dust grains whose diameters are less than or of the same order as the wavelength of the radiation. The effect of extinction is wavelength dependent, being stronger at shorter wavelengths. In the optical, normalized extinction, also known as the extinction curve, is defined as

$$R_\lambda \; = \; \frac{E_{\lambda-V}}{E_{B-V}}, \tag{7.1}$$

where $E_{B-V} = A_B - A_V$ is the selective extinction and A_λ is the total extinction at λ. B and V refer to the blue and visual photometric bands centered at 4400 Å and 5500 Å, respectively. Extinction curves are redshift dependent and carry information about the composition and size of the dust grains, the metallicity, the elemental abundance ratios and the star formation rate of that region of the ISM. One of the techniques that yields measurements of dust properties in high-redshift galaxies is by analysing the differential extinction curves of gravitationally lensed images. This can be achieved by assuming that the images have identical extinction laws, the image magnifications are both time- and wavelength-independent, and the source spectrum is time-independent during the observation time. Then, the difference in the magnitudes between a pair of images, A and B, of a lensed object is given by (Falco

et al. 1999)

$$m_{\rm A}(\lambda) - m_{\rm B}(\lambda) \;=\; -2.5 \log \frac{\mu_{\rm A}}{\mu_{\rm B}} + R\left(\frac{\lambda}{1+z_{\rm l}}\right)(E_{\rm A} - E_{\rm B}), \tag{7.2}$$

where $R(\lambda)$ is the extinction law for the lens galaxy in the rest-frame of the dust, and μ_i is the magnification and E_i is the selective extinction for the $i^{\rm th}$ image. A further assumption made is that the amounts of extinction due to the intervening material in the source galaxy and the Milky Way are equal in both the images.

Falco et al. (1999) investigated 37 differential extinction curves in 23 gravitational lens galaxies and found that B0218+357 and one other system (PKS 1830−211) in their sample have exceptionally high differential extinctions. According to their measurements, the extinction for image A is higher than for image B by $\Delta E_{B-V} = 0.9$ mag and the extinction for the images A and B together is equal to $E_{B-V} = 0.6$. This result is not surprising as there are various observations of atomic and molecular absorption lines in B0218+357 (see Sect. 2.2) that present strong evidence of large amounts of molecular gas and H I in the lens galaxy. However, a strong relative extinction in image A additionally implies that the molecular cloud, which is associated with these molecular absorption lines, lies directly in front of image A. This is in agreement with the observations of H I absorption in B0218+357 using VLBI with a resolution of 80 mas by Carilli et al. (2000). They found that the dominant contribution to the H I 21 cm line comes from the south-west component (image A). Similar findings were achieved by Menten & Reid (1996) who observed the formaldehyde (H_2CO) absorption lines with the VLA at 14.1 GHz and 8.6 GHz (VLA provides a spatial resolution of $\lesssim 0.2$ arcsec at these frequencies). They showed that the absorption arises solely due to image A and derived an upper limit on the optical depth for image B, 3 times smaller than that calculated for image A. This also lends support to the explanation proffered by York et al. (2005) in order to account for the mismatch in the image separation between the radio and the optical measurements (see Sect. 2.3.3). Dust obscuration of image A can also explain why image B is observed to be brighter that image A at optical wavelengths (Jackson et al. 2000; Lehár et al. 2000) while the opposite is true at all radio wavelengths.

Molecular clouds are of different types, such as Giant Molecular Clouds (GMCs) and dark clouds, and have a range of sizes (subparsec to larger than 100 pc), temperatures ($\sim$ 10 K to 100 K), number densities (10^2 cm^{-3} to 10^6 cm^{-3}) and masses (10 $M_\odot$ to 10^7 $M_\odot$) (Dame et al. 1986; Friberg & Hjalmarson 1990). Giant Molecular Associations or complexes (GMAs) are much bigger than the typical GMCs observed in the Milky Way Galaxy (Adler et al. 1992) and contain several smaller fragments associated with recent star formation sites and regions of ionized hydrogen (H II regions). Therefore, it is not unlikely that the line-of-sight to image A passes through one or more regions of ionized hydrogen residing in the molecular cloud. Assuming that the flux ratio anomaly in B0218+357 can be attributed to the molecular cloud in front of image A only, the mechanisms that are capable of altering the image flux-densities in the radio part of the spectrum are free-free absorption and refractive scattering. Both these mechanisms are caused mainly by free electrons and have a ν^{-2} dependence, and therefore multi-frequency observations, such as those described in this thesis, are needed to analyse them.

The nature of the molecular cloud associated with B0218+357, albeit not well-known to date, is starting to become clear. Recently, Henkel et al. (2005) made detections of ammonia (NH_3) absorption lines in the spectrum of B0218+357 using the 100 m Effelsberg radio telescope at a frequency of 15 GHz. Through determination of the rotation temperature

of ammonia, which provides a lower limit to the kinetic temperature of the molecular gas, they concluded that the nature of the absorber is consistent with a diffuse molecular cloud scenario rather than with a cold dark cloud. They have calculated a value of 55 K for the kinetic temperature and $\sim 10^{20}$ cm^{-2} to 10^{22} cm^{-2} for the column density of neutral hydrogen, depending upon whether the column densities are averaged over the entire continuum source or only over the core of image A. Further, using the measurements of CS, H_2O and CO molecular excitations, a firm upper limit for the number density of neutral hydrogen has been derived, $n \lesssim 2 \times 10^4$ cm^{-3}.

7.2 Free-free absorption

In the process of free-free absorption (Bremsstrahlung), a photon passing through a plasma is absorbed by an electron in a continuum energy state which jumps to a higher continuum energy state. It accelerates in the field of a positive ion where the presence of the latter is necessary for the conservation of momentum. Assuming the plasma to be in a state of Local Thermal Equilibrium (LTE) so that the Kirchoff law is valid, the free-free absorption coefficient (per unit length) is given by Kembhavi & Narlikar (1999, and references therein)

$$\alpha_{\rm ff} \;=\; \frac{4e^6}{3mhc}\left(\frac{2\pi}{3km}\right)^{1/2} T_e^{-1/2}\, Z^2 n_{\rm e}\, n_{\rm i}\, \nu^{-3}\,(1-{\rm e}^{-h\nu/kT_e})\,\bar{g}_{\rm ff}(T_e,\nu)\,, \tag{7.3}$$

where m and e are the electron mass and charge, $n_{\rm e}$ and $n_{\rm i}$ are the electron and positive-ion densities, T_e is the kinetic temperature of the gas, Z is the ionic charge and $\bar{g}_{\rm ff}$ is the velocity-averaged Gaunt factor. The Gaunt factor represents the quantum-mechanical correction to the classically derived result, and depends upon the electron energy (T_e) and the frequency of the photon (ν). At radio frequencies, the Gaunt factor can be approximated to (Brown 1987)

$$\bar{g}_{\rm ff}(T_e,\nu) \;=\; 11.962\left(\frac{T_e}{\rm K}\right)^{0.15}\left(\frac{\nu}{\rm Hz}\right)^{-0.1}. \tag{7.4}$$

In the Rayleigh-Jeans regime (Sect. B.1), the numerical expression for the absorption coefficient is

$$\alpha_{\rm ff} \;=\; 0.018\left(\frac{T_e}{\rm K}\right)^{-1.5} Z^2\left(\frac{n_{\rm e}\, n_{\rm i}}{\rm cm^{-6}}\right)\left(\frac{\nu}{\rm Hz}\right)^{-2}\bar{g}_{\rm ff}\ {\rm cm}^{-1}\,. \tag{7.5}$$

7.2.1 H II regions

For H II regions, an LTE environment is a good assumption. H II regions are formed around hot O– or early B–type stars that emit uv–photons capable of ionizing hydrogen clouds out of which these stars form in the first place. The delicate balance between the heating and the cooling mechanisms within such a photo-ionized plasma, which comprises mainly hydrogen atoms followed by helium (with relative abundance on the order of 10 % by number) and heavy elements (with abundances on the order of 10^{-3} or 10^{-4}), results in an equilibrium electron temperature of $\sim 10^4$ K. An electron in such a plasma can lose its initial kinetic energy either via Coulomb collisions or inelastic collisions with an ion or an atom. But for such regions, with a relatively narrow range of temperatures (10^4 K), and low ion to proton ratios ($\sim 10^{-3}$), it turns out that the time-scale associated with the Coulomb collisions is much shorter than that associated with the inelastic collisions. Therefore, the thermal equilibrium

is well maintained in such regions as any perturbation that enters into the system is quickly redistributed through Coulomb collisions amongst all the elements of the plasma.

H II regions can either be of an ultracompact-type with diameters ~ 0.1 pc, $n_{\rm e} > 10^4$ cm^{-3} and Emission Measures ($EM = \int n_{\rm e}^2\, ds$) $\sim 10^7$ cm^{-6} pc (Wood & Churchwell 1989) which form around young hot stars, or of an extended diffused-type with $n_{\rm e} \sim$ (1 to 1000) cm^{-3} and sizes ranging from a few parsecs to a few tens or a hundred parsecs (Shaver 1976; Roshi & Anantharamaiah 2001). But both types have a rather narrow range of temperatures from a few thousands kelvins to 10^4 kelvins. Substituting Eq. 7.4 in Eq. 7.5, the free-free absorption coefficient for an H II region is

$$\alpha_{\rm ff} \;=\; 3.19 \times 10^{-7} \left(\frac{n_{\rm e}}{1\,{\rm cm}^{-3}}\right)^2 \left(\frac{T_e}{10^4\,{\rm K}}\right)^{-1.35} \left(\frac{\nu}{\rm GHz}\right)^{-2.1} \;{\rm pc}^{-1}\,, \tag{7.6}$$

where a pure hydrogen nebula has been assumed and thus, $n_{\rm e} = n_{\rm i}$ and $Z = 1$. The intensity of background radiation that passes through an H II region is modified according to the law of radiative transfer to

$$I_{\rm ff}(\nu,\tau) \;=\; I_{\rm o}(\nu)\, e^{-\tau_{\rm ff}(\nu)} + S(\nu)\,(1 - e^{-\tau_{\rm ff}(\nu)})\,, \tag{7.7}$$

where $I_{\rm ff}$ and $I_{\rm o}$ are the modified and background intensities, respectively, $\tau_{\rm ff}$ is the optical depth equal to the integral of the free-free absorption coefficient over the path length through the plasma ($\int \alpha_{\rm ff}\, ds$) and S is the source function equal to the ratio of the emission coefficient to the absorption coefficient, which under the conditions of LTE is equal to the Planck blackbody spectrum. Since a source temperature of $\sim 10^4$ K is below the minimum brightness temperature that can be detected using VLBI, the second term including the source function can be ignored. This simplification can be verified as follows. The flux-density per unit beam of a blackbody of temperature T is equal to its source function integrated over the synthesized beam,

$$F \;=\; S(\nu)\,\Omega_{\rm B} \;=\; \frac{2kT}{\lambda^2}\,\Omega_{\rm B}\,, \tag{7.8}$$

where the source function is set equal to the Planck function in the Rayleigh-Jeans part (see Appendix B.1), $\Omega_{\rm B}$ is the synthesized beam $\approx \lambda^2/d^2$, d is the baseline length, and the source function is assumed to be a constant throughout the region of the plasma. Then,

$$F \;=\; \frac{2kT}{d^2}\,. \tag{7.9}$$

For typical VLBI experiments, $d \sim 10^4$ km. Thus, the flux-density per unit beam is on the order of 0.1 μJy which is much lower than the detection threshold of few tens of μJy. Hence, the outgoing radiation from a region of plasma can be written as

$$I_{\rm ff}(\nu,\tau) \;=\; I_{\rm o}(\nu)\, e^{-\tau_{\rm ff}(\nu)}\,. \tag{7.10}$$

Assuming the H II region to be homogeneous in electron density and temperature, the optical depth of the cloud is equal to $\alpha_{\rm ff} L$, where L is the size of the plasma. Therefore, using Eq. 7.6 and the definition of $EM = n_{\rm e}^2 L$, the optical depth is

$$\tau_{\rm ff} \;=\; 3.19 \times 10^{-7} \left(\frac{T_e}{10^4\,{\rm K}}\right)^{-1.35} \left(\frac{EM}{{\rm cm}^{-6}\,{\rm pc}}\right) \left(\frac{\nu}{\rm GHz}\right)^{-2.1}\,. \tag{7.11}$$

Table 7.1: b and d are the power law indices fitted to the spectra of images, A and B. T is the temperature and EM is the emission measure of the H II region. Given also are the various combinations of the electron density and the size of the cloud for given emission measures.

b	d	T	EM	L		$n_{\rm e}$
		(K)	($\rm cm^{-6}$ pc)	(pc)	(mas)	($\rm cm^{-3}$)
0.153±0.018	0.147±0.022	10^4	$(6.00 \pm 0.92) \times 10^6$	1	0.15	2450
				10	1.5	775
				100	14	245
				200	28	173
		4 000	$(1.74 \pm 0.27) \times 10^6$	1	0.15	1321
				10	1.5	418
				100	14	132
				200	28	93

7.2.2 Parameter estimation of the H II region

In order to determine the parameters of the H II region, under the hypothesis of free-free absorption as an explanation for the anomalous image flux-density ratios in B0218+357, the spectrum of image B is assumed to reflect the true source spectrum. It is also assumed that the H II region covers the whole of image A at all frequencies. Then, using the isothermal lens model described in chapter 5 ($\beta = 1$ in Table 5.1), the true spectrum of image A can be determined. Further, with the help of Eq. 7.6 and from the knowledge of the true and the modified spectrum of image A, Eq. 7.10 can be fitted to the observed flux-densities at different frequencies to determine the best fitting values of the plasma parameters. Unfortunately, the optical depth is degenerate to the following parameters which describe the H II region: the electron density, the temperature and the size of the cloud. But since the temperature is known to within a factor of two or three, the combination of the two remaining parameters, EM, can be uniquely determined.

The parameters of the hypothesized H II region were estimated as follows. First, it is to be noted that the spectra of image B and the modelled image A can be well-approximated by a synchrotron power-law,

$$F_A(\nu) \propto \nu^{-b} \; ; \; F_B(\nu) \propto \nu^{-d} \, , \tag{7.12}$$

where $F_A(\nu)$ is the image A flux-density and $F_B(\nu)$ is the image B flux-density, and b and d are the power law indices fitted to their spectra. The spectral indices of image A and image B are chosen differently due to slightly different relative image-magnifications at varying frequencies (see Fig. 5.6). This has the effect of producing small differences in the spectral shapes of the lensed images as explained in Sect. 5.6. Substituting $F_A(\nu)$ for $I_o(\nu)$ in Eq. 7.10, the best-fitting value for EM can be calculated using the χ-square minimization method to minimize the difference between the observed and the modelled image A flux-densities. Shown in Fig. 7.1 are the flux densities of image A (blue crosses) modelled using the observed flux densities of image B (pink crosses). The fitted power-law spectra are shown in dotted lines. The free-free absorption curve (red solid curve) is fitted to the observed flux-densities of image A (red crosses). The various parameters, including the electron densities for different values of L, estimated for two temperatures are given in Table 7.1. The values of EM, although quite large, are consistent with those measured in giant Galactic H II regions, and the estimations

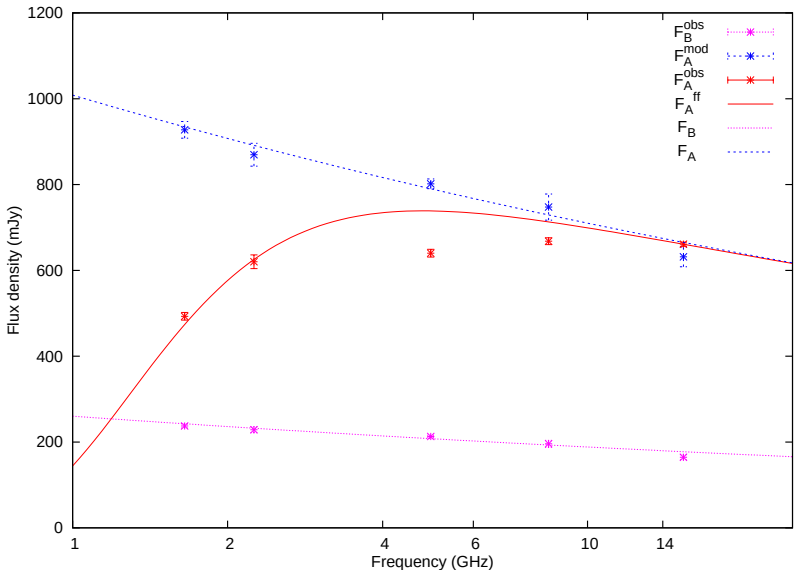

Figure 7.1: The free-free absorption curve (red solid curve) fitted to the observed spectrum of image A (red crosses). The modelled flux-densities of image A (blue crosses) follow the measured flux-densities of image B (pink crosses) and their spectra (dotted lines) have nearly the same power law index.

of n_e and L are also in good agreement with those observed for Galactic and extragalactic H II regions. Shown in Table 7.2 is a comparison between the image flux-density ratios obtained from the observations (second column) and those obtained after applying the free-free absorption model (third column), using Eq. 7.10. There is a good accordance between these values and it is seen that the absorption can explain the observed trend very well at all the frequencies except at 4.96 GHz where the two values differ slightly, as is also visible from Fig. 7.1. As a further comparison, the ratios calculated from applying the SIEP model in chapter 5, for the case where image-B is the primary image, are also given (the fourth column).

The most crucial assumption in the free-free absorption hypothesis, as discussed above, is that there is a plasma of free electrons in front of image A. This assumption is fairly reasonable considering that the Faraday rotation measured in front of image A is large (O'Dea et al. 1992; Patnaik et al. 1992a) which can arise only due to an electron-rich ISM. Such large Faraday rotation measures have been seen in the observations of extragalactic radio sources that lie directly behind H II regions (e.g. Heiles et al. 1981, and references therein). The latter have been modelled as a result of star formation activities within molecular clouds. Thus, the above picture in which emission from image-A is partly absorbed by a cloud of electrons is perfectly legitimate.

The size and position of the H II region relative to the brightness distribution of image A at different frequencies is difficult to analyse. This is due to an insufficient number of constraints available either from these observations or from the molecular (and atomic) line observations of this system by other authors. Even so, the maps of image A from the observations are strongly suggestive of the absorption screen being directly in front of the centre-most region containing components 1 and 2. Fig. 7.2 shows the spectrum of image B (green dashed line and cross symbols) resulting from the integration of the flux density over a small region which

Table 7.2: Image flux-density ratios versus frequency as obtained from the observations (second column), the free-free absorption model (third column) and the isothermal lens-model (fourth column).

ν (GHz)	F_A^{obs}/F_B^{obs}	F_A^{ff}/F_B^{obs}	F_A^{mod}/F_B^{obs}
1.65	2.07±0.06	2.00	3.90
2.25	2.71±0.11	2.73	3.80
4.96	3.01±0.06	3.44	3.76
8.40	3.41±0.15	3.61	3.82
15.35	4.01±0.15	3.98	3.84

has a maximum size at the lowest frequency (1.65 GHz) of about 2 mas by 1 mas around B1 (15.35 GHz). The corresponding spectrum of image A (blue dashed line and star symbols) at all the frequencies was computed from mapping these subregions of image B into equivalent regions in image A using the isothermal mass-radius profile and the techniques described in Sect. 5.4. The observed flux-densities of image A integrated within these predicted subregions (red plus symbols) are also indicated. The mapped region in image A has the maximum size (also at the lowest frequency) of about 4 mas by 2 mas. From comparing the modelled spectrum of image A to the observed one in Fig. 7.2, it can be seen that while there is a good match between the modelled and the observed flux-densities at 15.35 GHz, there is a clear indication of strong absorption at lower frequencies. The percentage absorption increases with decreasing frequency and is (< 0.1, 28.2, 47.5, 76.7, 81.2) % at (15.35, 8.40, 4.96, 2.25, 1.65) GHz. Thus, this gives a lower bound of 4 mas on the size of the ionized region, which corresponds to linear size of ~ 30 pc in the lens plane.

From the above discussion, it can be concluded that the free-free absorption hypothesis *is capable* of solving the image flux-density ratio anomaly in B0218+357. The parameters of the

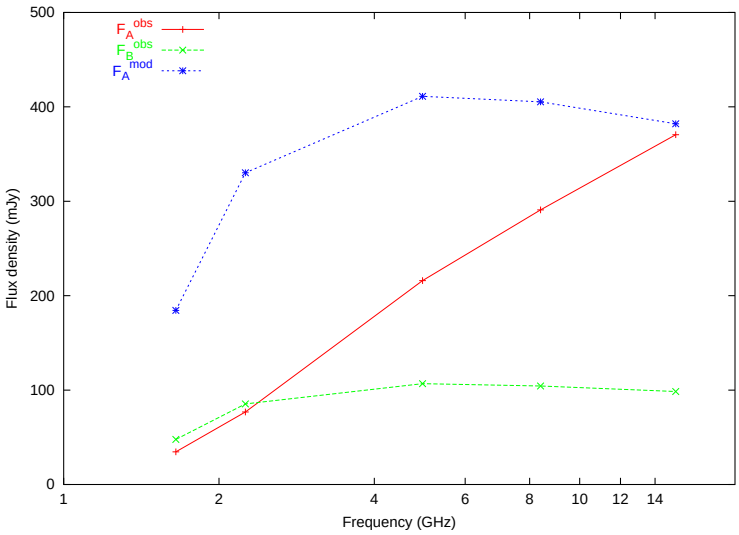

Figure 7.2: Absorption in image A in the inner-most region containing components 1 and 2. Shown are the observed flux-densities in image B (green stars) within a region of (2 by 1) mas around B1, and the modelled image-A flux-densities (blue crosses) at different frequencies. The observed flux-densities in image A are shown as red plus symbols.

H II region cannot be constrained uniquely because of an insufficient number of constraints and the existing degeneracy between the size of the region and the electron density. But the combinations of n_e and L measured for two extreme temperatures, the emission measures, fit well to the observed trend in image A flux-density and, also, similar values have been measured for the Galactic and extragalactic H II regions, lending further support to the hypothesis.

7.3 Scattering

In this section, the scattering process, which is known to prevail in the observations of many extragalactic sources, will be discussed. The most important scattering mechanism is scattering due to electrons in a plasma. To investigate if this is the cause for the anomaly in the image flux-density ratio in B0218+357, two scenarios will be visualized. In the first scenario, the electron density is assumed to be constant within the region of interest and the optical depth due to Thompson scattering is determined to gauge its effect on the image A flux-density. This is investigated in Sect. 7.3.1. In the second scenario, the effect of inhomogeneity in the electron density is taken into account. This is commonly referred as refractive scattering which gives rise to radio scintillation and image broadening, and discussed in Sect. 7.3.2.

7.3.1 Thompson scattering due to a homogeneous electron density

The H II region discussed in the framework of the free-free absorption hypothesis in Sect. 7.2 comprises electrons and ionized H atoms which can scatter the radio emission coming from the lensed quasar away from the line-of-sight to the observer. If the electron is in motion relative to the incoming photon, the energy can either be transferred from the photon to the electron or vice-versa. The latter process is called inverse Compton scattering. If ϵ $(= h\nu)$ denotes the energy of the incoming photon, γ the Lorentz factor and mc^2 the rest mass energy of the electron then

$$\gamma\,\epsilon \;\ll\; m\,c^2 \tag{7.13}$$

corresponds to the Thompson scattering regime in the rest frame of the electron. After the scattering event, the energy of the photon changes from ϵ to $\gamma^2\epsilon$. Hence, for highly relativistic electrons (high Lorentz factor) the energy transfer can be quite large. But for an H II region, which is in a state of LTE and has a steady temperature of around $\sim 10^4$ K, the electrons are non-relativistic and $\gamma \sim 1$. Therefore, at radio wavelengths the above condition is always satisfied for H II regions and the fractional change in the photon energy is very small. Nevertheless, such a scattering event changes the direction of the emitted photon resulting in a net absorption of the background radiation.

Assuming a homogeneous electron-density throughout the H II region postulated in Sect.7.2.2, the optical depth of scattering by electrons is (Rybicki & Lightman 1979)

$$\tau_{\rm es} \;\sim\; \rho\,\kappa_{\rm es}\,L\,, \tag{7.14}$$

where ρ, $\kappa_{\rm es}$ and L are the mass density of the medium, the opacity due to the electron scattering and the size of the region. The electron scattering opacity for ionized hydrogen is 0.40 cm^2 gm^{-1}. The mass density of the medium can be approximated by the product of the proton mass and the electron number density. However, the electron density and the size of the cloud for the H II region in consideration are not uniquely known, as explained in Sect.7.2.2. But instead, the estimated emission measures given in Table 7.1 can be used

to replace L in Eq. 7.14 and to reduce the equation to a function of a single variable, the electron density. Thereafter, the scattering optical depth can be calculated for the different emission measures and its importance be assessed. With $\rho = m_{\rm p}\, n_{\rm e}$, where $m_{\rm p}$ is the proton mass, and $L = EM/n_{\rm e}^2$,

$$\tau_{\rm es} \sim \frac{m_{\rm p}}{n_{\rm e}}\, 0.40\, EM\,,$$

$$\sim 2 \times 10^{-6} \left(\frac{n_{\rm e}}{\rm cm^{-3}}\right)^{-1} \left(\frac{EM}{\rm cm^{-6}\,pc}\right)\,. \qquad (7.15)$$

On substituting different values of $n_{\rm e}$ and EM tabulated in Table 7.1, it is seen that the mean number of scatterings for all combinations is very low, $(0.002 < \tau_{\rm es} < 0.07)$. Thus, scattering due to a homogeneous density of electrons assumed to constitute the plausible H II region in front of image A can be safely neglected in the present context.

7.3.2 Scatter-broadening due to inhomogeneities in the electron density

Extragalactic sources are often found to be scatter-broadened by an intervening screen of turbulent plasma. The fluctuations in the plasma density induce variations in the refractive index, which roughly scale as ν^{-2}, and in turn scatter the background radiation. There have been claims of scatter-broadening seen in gravitational lenses as well, such as PMN J1838-3427 (Winn et al. 2004), PKS 1830-211 (Jones et al. 1996; Guirado et al. 1999), B1933+503 (Marlow et al. 1999b) and B0218+357 (Biggs et al. 2003).

Scattering by an infinite screen with homogeneous fluctuations in the electron density does not result in any changes in the flux-density of the background source. Based on symmetry arguments it can be proven that, in such a case, as much flux is scattered away as toward the line-of-sight to the observer, resulting in the conservation of flux-density. But this is no longer the case if there are variations in the statistical properties of the scattering screen. This includes the case where the scattering material appears in front of the scattered image only in parts, separated by 'holes' comprising neutral matter. In particular, if the scattering screen is truncated over the size of the scattered background image, it will lead to an attenuation of the source flux-density (Cordes & Lazio 2001). Thus, variations in the lensed image flux-densities because of an intervening scattering medium can occur only when there are discontinuities or variations in the scattering strength. To probe the amplitude of scattering, the first issue that is addressed in the following is whether image A is affected by scattering at all in the first place or not. From an observational standpoint, the quantities which provide evidence for scattering are the image-sizes, in particular their dependences on frequency, and temporal variations in the image flux-density. An observation history of B0218+357, which is over a decade long, reveals no temporal variations in the image flux-densities.

Scattering studies and measurements have been popular for over two decades now, and the basic physics behind the scattering mechanism is quite well-established (e.g. Rickett 1990; Narayan 1992; Goodman 1997). The general picture consists of an irregular ionized medium between the source and the observer, which is confined to a thin screen called the scattering screen. An initially plane wavefront from the source emerges irregular from the scattering screen due to phase changes imposed by the scattering medium. The scattering process is divided into several regimes and subregimes. The regime of relevance in the present context is refractive scattering, as opposed to diffractive scattering. Refractive scattering is due to large-scale inhomogeneities in the medium with length scales, $r_{\rm ref}$, known as the refractive

Table 7.3: The deconvolved sizes of the smallest components in the B0218+357 images at all the frequencies obtained from fitting two-dimensional elliptical Gaussians. a and b are the major and minor axes of the ellipse, ϕ is the position angle of the major axis measured from north through east. Also given are the geometric means of the axes of the Gaussians.

ν (GHz)	Comp.	a (FWHM, mas)	b (FWHM, mas)	ϕ	$\sqrt{a \times b}$ (mas)
1.65	A	11.34±0.02	9.37±0.02	-6.5±0.50	10.31±0.01
	B	6.91±0.29	2.73±0.45	77.4±3.0	4.34±0.37
2.25	A	9.77±0.13	6.88±0.10	-20.6±1.6	8.20±0.08
	B	4.055±0.001	1.671±0.001	77.25±0.01	2.603±0.001
4.96	A	2.93±0.07	2.70±0.07	-25.2±12.1	2.81±0.05
	B	2.18±0.01	0.51±0.01	88.7±0.1	1.05±0.01
8.40	A	1.11±0.03	0.90±0.04	-31.3±1.1	1.00±0.03
	B	0.68±0.10	0.231±0.001	88.1±1.1	0.40±0.03
15.35	A1	0.52±0.02	0.25±0.01	-27.8±1.7	0.36±0.01
	B1	0.26±0.03	0.15±0.05	87.5±2.3	0.20±0.04

scale. This scale is much greater than what is known as the diffractive length-scale, $r_{\rm diff}$, which represents the transverse spatial-scale for which the root-mean-square phase change due to the intervening plasma blobs is equal to 1 rad. For refractive scattering, $\theta_{\rm r} = r_{\rm ref}/D_{\rm l}$ corresponds to the size of the scatter-broadened image of a point source projected back on the scattering screen (which is assumed to be in the lens plane), where $D_{\rm l}$ is the angular diameter distance from the observer to the scattering screen. For a source with a non-negligible size in comparison with the angular broadening size, the Gaussian-equivalent angular size of the image as measured is the quadrature sum of the intrinsic source-size and the refractive length scale. The latter scales as $\nu^{-2.2}$ (Eq. 7.19), which introduces the ν–dependence of the scattering observables. Diffractive scattering, on the other hand requires sufficiently compact sources, $\theta_{\rm s} < r_{\rm diff}/D_{\rm l} = \theta_{\rm diff}$, which for extragalactic scattering screens is rarely ever fulfilled, and therefore is not considered here.

Shown in Table 7.3 are the results from fitting elliptical Gaussians using the AIPS task JMFIT (explained in Sect. 4.3.4) to the smallest detectable components in both the images at all frequencies. The tabulated parameters are the deconvolved major and minor axes (FWHM), the orientation angle and the geometric mean of the axes (equivalent circular radius, R). At 8.4 GHz and 15.35 GHz, due to poor error estimates on the parameters, another AIPS task IMFIT was used to yield more reliable errors by examining the spread in the results from both IMFIT and JMFIT (see Sect. 4.3.4). Shown in Fig. 7.3 are the equivalent circular radii, $R_{\rm A}$ and $R_{\rm B}$, of the ellipses fitted to these components plotted as a function of frequency. On fitting power-law curves through these data points $\sim \nu^{-k_{a,b}}$, where the power law indices, k_a and k_b, correspond to the curves through A and B respectively, it is found that

$$k_a = 1.40 \pm 0.11 \quad ; \quad k_b = 1.17 \pm 0.05\,. \tag{7.16}$$

Also shown in Fig. 7.4 is the ratio, $(a \times b)_{\rm A}/(a \times b)_{\rm B}$, at different frequencies. At 15 GHz the ratio agrees with the relative image-magnification predicted by the lens models to within the errorbars, which in turn is consistent with the observed ratio of the image flux-densities. The ratio increases gradually with wavelength as $\nu^{-0.4}$ up to 2.25 GHz and then shows a sharp

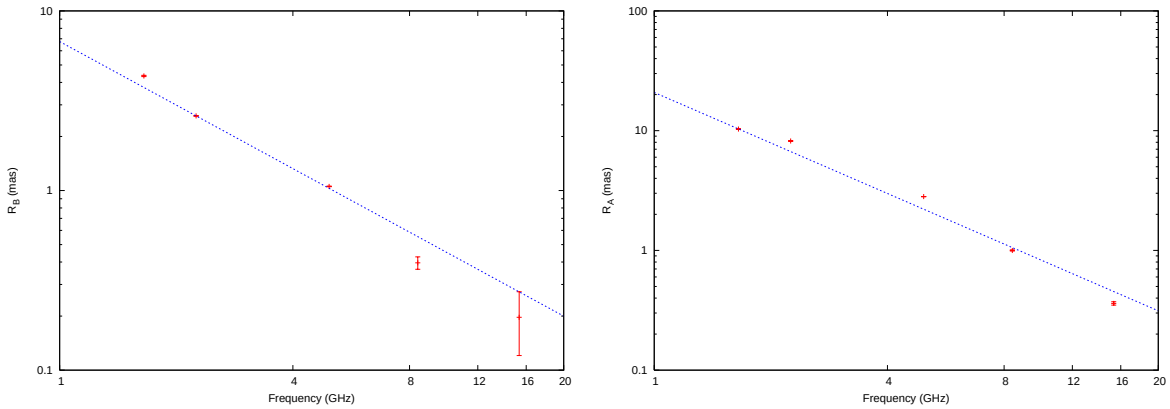

Figure 7.3: Log-log plots of the geometric means of the axes of the elliptical Gaussians fitted to the smallest components in image A (right panel) and image B (left panel) versus frequency. Note that the scales on the y–axes are different for the two images.

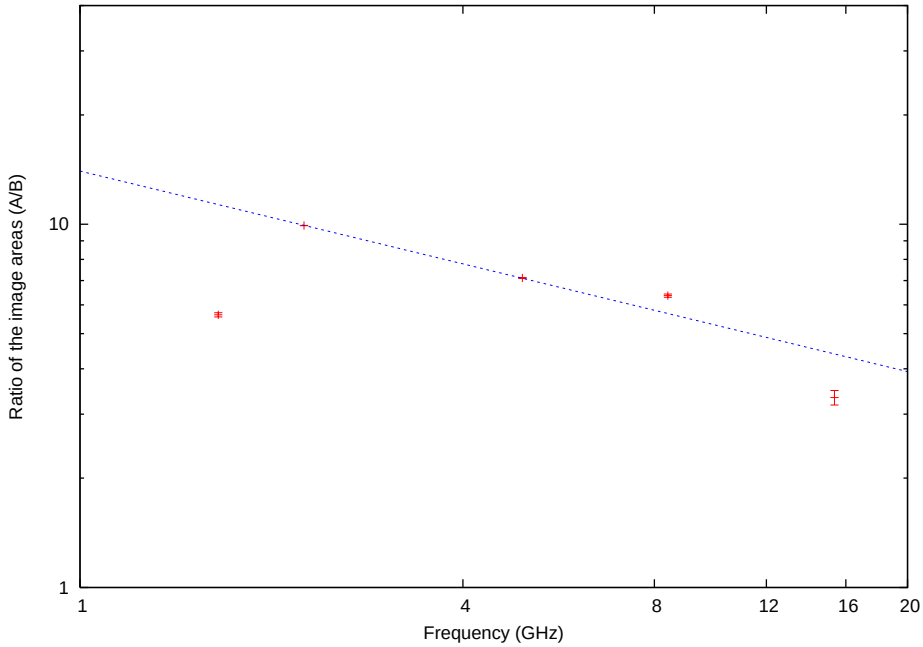

Figure 7.4: A log-log plot of the ratio of the areas (A/B) under the elliptical Gaussians fitted to the smallest components in the images versus frequency. The dotted straight line is fitted through all the frequencies except at 1.65 GHz and has a slope of -0.4.

decline at 1.65 GHz, albeit remaining above the value at 15 GHz. It should be pointed out that the scattered images produced by a homogeneous scattering screen, in general, have circular shapes due to isotropic scattering. Image A, on the contrary is elongated in roughly the same direction as predicted by the magnification matrix. In other words, the tangential eigen direction due to lensing is preserved. This is not an argument against scattering, however, because the phenomenon of gravitational lensing affects the scattering angle in the same way as the background source, i.e. the scattering angle also gets magnified in the tangential direction (Wucknitz, private communication).

The presence of two images of the same background source, if only one is assumed to be

affected by scattering, can be used to advantage through determination of the true source size using the unaffected image. To determine the effects of scattering on the B0218+357 image properties, similar arguments are followed as those presented in Sect. 7.2.2 in that it is assumed that image B is unaffected by scattering or any other mechanism such as free-free absorption or milli-lensing. Then, the size of a component measured at any frequency in image-B projected back to the source plane will correspond to the intrinsic size of this component. From this, its equivalent size in image A can be calculated and compared to the observed size to yield a value for the refractive scale at that frequency. But this one-to-one correspondence can, from these observations, only be made at 15 GHz since at lower frequencies neither of the components 1 and 2 can be resolved, nor has any other distinct component been unambiguously detected in both the images. The third component in image A does not add any new information since it can either be that it is intrinsic to the source structure but due to insufficient resolution remains undetected in image B, or that it is produced by some other astrophysical mechanism (see Sect. 4.3.5). Thus, translating image B component-sizes to the true source sizes is not a reliable approach for analysing the scattering hypothesis. Therefore, even though the similarity between the fitted power-law indices for both the images is highly suggestive of no or hardly any scattering in front of image A, the possibility cannot be ruled out completely. Accordingly, the scattering supposition in front of image A is pursued a little further in the hope to derive some meaningful limits.

Before deriving limits to $\theta_{\rm r}$, it should be recalled that the observed component-sizes are magnified by the lens galaxy. To translate a measured size in the image plane to its true size in the source plane, the same recipe is used as described in Sect. 6.1.1. The average values of tangential magnification and *de-magnification* for images A and B are assumed to be 2 and 0.5, respectively. Consequently, the estimated sizes of the source-component 1, from the equivalent circular sizes of A1 and B1 at 15 GHz, are:

$$\theta_{\rm s_A} \,=\, 0.25 \pm 0.03 \text{ mas} \quad ; \quad \theta_{\rm s_B} \,=\, 0.28 \pm 0.03 \text{ mas}\,. \tag{7.17}$$

Thus, there is an excellent agreement between the observations and the model-predictions at 15 GHz. But this is not surprising, since it is generally accepted that 15 GHz observations of this lens system are devoid of any discrepancies. The lens models discussed in chapter 5 are derived assuming that the image flux-densities and positions observed at 15 GHz are free from any intervening astrophysical mechanisms since most interstellar effects go as ν^{-2}.

On the other hand, assuming that the component in image A fitted at 1.65 GHz is solely due to the scattering disk, an upper limit of $\theta_{\rm r} = \theta_{\rm s_A} = 7.29$ mas is derived. It is to be noted that this is the *observed* scattering angle and depends upon the location of the scattering screen with respect to the source and the observer. The true scattering angle is

$$\hat{\theta_{\rm r}} \,=\, \frac{D_{\rm s}}{D_{\rm ls}}\,\theta_{\rm r}\,, \tag{7.18}$$

where $D_{\rm ls}$ is the angular diameter distance between the scattering screen (the lens galaxy) and the source. The quantity which is sought is the Scattering Measure (SM, in units of kpc m$^{-20/3}$), which is the integral of the strength of the turbulence in the electron density distribution along the line-of-sight. Following the mathematical prescription given by Walker (1998) for a homogeneous scattering screen, the relation between the refractive scale for a point source ($\theta_{\rm s} < \theta_{\rm r}$) and SM is

$$SM \,=\, \left[1.6 \times 10^{-5}\,\hat{\theta_{\rm r}}\,\left(\frac{\nu}{\rm GHz}\right)^{2.2}\right]^{5/3} \text{kpc m}^{-20/3}\,. \tag{7.19}$$

Table 7.4: The scattering angular-sizes as a function of frequency for $SM = 2.12$ kpc m$^{-20/3}$ ('I') and $SM = 0.76$ kpc m$^{-20/3}$ ('II'), the back-projected component sizes in image A, θ_{s_A}, the quadrature difference of θ_{s_A} and $\theta^2_{r(II)}$, and the back-projected component sizes in image B, θ_{s_B}.

ν (GHz)	$\hat{\theta}_r$ (mas)		θ_r (mas)		θ_{s_A} (mas)	$\sqrt{\theta^2_{r(II)} - \theta^2_{s_A}}$	θ_{s_B} (mas)
	I	II	I	II			
1.65	32.48	17.51	7.29	3.93	7.29	6.14	6.14
2.25	16.42	8.85	3.70	1.99	5.80	5.45	3.68
4.96	2.88	1.55	0.65	0.35	1.99	3.84	1.48
8.40	0.90	0.49	0.20	0.11	0.71	0.70	0.57
15.35	0.25	0.13	0.06	0.03	0.25	0.25	0.28

Thus as pointed out earlier in this section, the scattering angle corresponding to the refractive scale, θ_r (which is related to $\hat{\theta}_r$ through Eq. 7.18), scales as $\nu^{-2.2}$. Substituting $\hat{\theta}_r$ and $\nu = 1.65$ GHz in Eq. 7.19, a value of $SM = 2.12$ kpc m$^{-20/3}$ is obtained. It should be pointed out that the above limit on θ_r is a secure upper limit since the intrinsic size of this component at 1.65 GHz is > 0. In fact, $\theta_{s_A} = 7.29 \pm 0.01$ mas is close to $\theta_{s_B} = 6.14 \pm 0.52$ mas. Therefore, the true intrinsic source-size corresponding to the smallest component measured in image A at 1.65 GHz must be close to θ_{s_A}. This will decrease the scattering measure.

A second value of SM can be estimated by assuming a true correspondence between the observed components at 1.65 GHz. Then, the quadratic difference in the back-projected sizes of the components can be attributed to the intervening scattering disk. In this case, $\theta_r = \sqrt{\theta^2_{s_A} - \theta^2_{s_B}} = 3.93$ mas. This leads to a value of $SM = 0.76$ kpc m$^{-20/3}$.

Substituting these value of scattering measure into Eq. 7.19, θ_r can be determined at other frequencies as well and are given in Table 7.4. 'I' corresponds to when the A component at 1.65 GHz is used and 'II' corresponds to when the back-projected component in B at 1.65 GHz is assumed to represent the intrinsic source-size. Also given in Table 7.4 are the sizes of the image components projected back to the source plane, θ_{s_A} and θ_{s_B}, and the quadrature difference of θ_{s_A} and $\theta^2_{r(II)}$. For the first method ('I'), θ_r and θ_{s_A} can be directly compared and it is clearly seen that except at 1.65 GHz, there are strong inconsistencies at other frequencies. For the second method ('II'), the difference between θ_{s_A} and $\theta^2_{r(II)}$, in quadrature, should be compared with θ_{s_B}. Once again, except at 1.65 GHz the values don't match. It should be mentioned, nevertheless, that the two values for SM derived in this section are comparable to the values of SM calculated for other galactic and extragalactic scatter-broadened sources; for example, the extragalactic source B1849+005 associated with the supernova remnant G33.6.01 has $SM \sim 4.6$ kpc m$^{-20/3}$ (Spangler et al. 1986) and a sample of six other extragalactic sources with their lines of sight passing through the Cygnus OB1 association has SM in the range of 0.14 kpc m$^{-20/3}$ to 2.21 kpc m$^{-20/3}$ (Spangler & Cordes 1998). Biggs et al. (2003) have suggested a much higher value of $SM = 150$ kpc m$^{-20/3}$ which is atypical compared to those measured along the typical lines of sight through the Galaxy but not inconsistent with the measurements in the direction of the Galactic center. However, their value is clearly not in agreement with the upper limit derived from these observations, given in Table 7.4.

To summarize, it seems that scattering is not a satisfactory explanation for the flux ratio

anomaly seen in B0218+357. The reasons are two-fold. First, there is no strong evidence of image-broadening for image A. This follows from the similarity of the ν–dependencies of the component-sizes in both the images and under the assumption that image B does not suffer from any scattering. Moreover, the ν–dependencies do not resemble the standard ν^{-2} scattering law. Instead, the index-values (slightly bigger than one) indicate that the increase in image-sizes with wavelength is intrinsic, common to most synchrotron self-absorbed sources. Second, even though the scattering measures derived in the above analysis are within the observed range of scattering measures in other systems, the back-projected component-sizes in both the images and the size of the scattering disk are not in agreement with each other. However, these conclusions may be drawn only if the scattering strength is assumed to be homogeneous throughout the extent of the image A. On the other hand, if the scattering screen is clumpy and anisotropic, the analysis is no longer as straight-forward as that presented here. But again, due to the similar power-law indices for the component-sizes in both the images, inhomogeneous scattering screens in front of both the images will have to be considered. This is unlikely given the fact that the ISM in front of image A is very different and much more optically active that in front of image B (as explained in Sect. 7.1).

7.4 Conclusions

Two propagation effects, free-free absorption and scattering, with an inverse-frequency-squared dependence have been investigated in the context of the flux ratio anomaly in the lens system B0218+357. Both these mechanisms are assumed to occur in the medium of the lens galaxy. The image B properties, the flux-densities and sizes at varying frequencies, are assumed to remain unaffected by these processes. To test the free-free absorption hypothesis, an H II plasma in front of image A is envisaged which comprises free electrons that through Coulomb collisions absorb a part of the incoming image-A radiation, $I_{\rm o}$. The image A flux-density is attenuated by a factor, $e^{-\tau(\nu)}$, which depends upon the optical depth (τ) of the cloud, and the spectrum of image A is altered. Using the isothermal lens-model described in chapter 5, the observed flux-densities of image B are used to calculate the corresponding flux-densities of image A at all the frequencies. These values are used to fit the free-free absorption curve to the observed flux-densities of image A (Fig. 7.1) and the EM of the H II region is constrained to within 13 % accuracy. This has been done for two values of the electron temperature, which is known to have a very narrow range from copious observational data of other H II regions. The resulting values of EM appear to be in the typical range observed in other galactic and extragalactic H II regions. Thus, free-free absorption is an excellent candidate to explain the frequency-dependent image flux-density ratios.

From the lens models described in chapter 5, image A lies at a projected distance of 2 kpc from the lens centre. Its line-of-sight may well pass through one of the spiral arms of the galaxy (see Fig. 2.7), which are known to harbour extensive star forming regions and are rich in population I objects, such as young blue stars surrounded by H II regions. In fact observations of other late-type spiral galaxies, such as M 51 (Lo et al. 1987), have shown that molecular gas, in the form of huge complexes of giant molecular clouds, is strongly confined to the spiral arms of a galaxy. Thus, it is possible that the image-A line-of-sight passes through such a region rich in gas and ionized plasmas (HII regions). From the measurements of NH_3 absorption lines, Henkel et al. (2005) visualize the molecular absorber in front of image A to be elongated along a path with roughly constant galactocentric radius to reconcile with

high source covering factors observed at mm-wavelengths. Elongated filament-like molecular clouds have been observed in the Milky Way, such as the Orion GMC and the Monoceros GMC. For the free-free absorption hypothesis, it has been assumed that the H II cloud covers image A in entirety at all the observed frequencies. At 1.65 GHz, the total extent of image A in the tangential direction is ~ 28 mas which corresponds to a linear size of ~ 200 pc in the lens plane. Such giant (and supergiant) H II regions, although not ubiquitous, have indeed been observed, both as galactic and extragalactic as well. For example, the giant H II region complex W49 in the Milky Way Galaxy has $L = 150$ pc and $n_{\rm e} = 100$ cm^{-3}, NGC 604 in M33 has $L = 400$ pc and $n_{\rm e} \leq 60$ cm^{-3} and NGC 5471 in M101 has $L = 800$ pc and $n_{\rm e} = 200$ cm^{-3} (Shields 1990). Thus, the scenario in which the flux-density of image A is perturbed by a giant H II region embedded in a turbulent molecular complex via free-free absorption can be easily envisioned. In reality, it may well be that there are several H II regions embedded within the same molecular cloud but at different spatial locations and in projection cover the entire image A. Lastly, the question arises whether such a GMC visualized in front of image A can by virtue of its large mass result in the magnification of image A, and possibly also its position, differing from that predicted by the current lens-model. Solomon & Sanders (1980) estimated the mass-spectrum of the observed clouds in the Milky Way Galaxy and concluded that about 90 % mass of the molecular ISM is contained in GMCs with sizes larger than 20 pc and typical masses of 10^5 $M_\odot$. As future work, it will be interesting to assess the effect of a plausible giant molecular complex on the image A properties, provided it is massive and compact enough.

The scattering hypothesis has been invoked for this lens system before by Biggs et al. (2003), who compared the 8.4 GHz maps of the images back-projected on the source plane and concluded that the subcomponents A1 and A2 have bigger sizes than B1 and B2. This, they claimed, was due to scatter-broadening in image-A due to a turbulent medium in the lens galaxy, which is known to be ion and gas rich (see Sect. 2.2 and Sect. 7.1). In Sect. 7.3.2, similar comparisons between the image sizes have been tried with the present multi-frequency observations by applying a simple but effective method of determining the equivalent circular sizes of the components in the source plane from their fitted values in the image plane (the last two columns given in Table 7.4). But a direct comparison of the source-sizes derived from image A with those from image B presents a difficulty due to the ambiguity in the identification of the corresponding components in the images on the image plane. Except at 15 GHz, due to different image magnifications, it is not clear if the elliptical Gaussian fitted to an unresolved component in one image corresponds to the superposition of the same set of components in the source as fitted in the other image. The 8.4 GHz maps that Biggs et al. (2003) used for their analysis were obtained from global VLBI observations of B0218+357 with an rms noise of 30 μJy beam^{-1}. With this sensitivity, components 1 and 2 can easily be resolved in both the images. The rms noise in the 8.4 GHz maps of B0218+357 obtained from observations used in this work, in comparison, is at least a factor 10 higher and the components are unresolvable in image A and just resolvable in image B (this is because the component-separation along R.A. is more in image B than in image A, see Table 5.2). The sizes of the components fitted to the images indicate, individually, a similar frequency-dependence, $\nu^{-k_{\rm a,b}}$, with $k_{\rm b} = 1.2$ for image B and a slightly stronger dependence, with $k_{\rm a} = 1.4$ for image A. It is to be noted that while the scattering angle scales with the inverse of frequency-squared, the intrinsic size has a much less pronounced dependence on the frequency. Based on extensive observational evidence it is seen that the angular size of a synchrotron self-absorbed source scales roughly as inverse frequency (Marscher 1977). Thus, the increase in the component-sizes in both the images can

be an intrinsic effect. On the other hand, the scattering medium considered in this analysis is assumed to have statistically homogenous properties. It may well be that this assumption is not valid and that either the scattering measure has spatial variations transverse to the line-of-sight or the scattering screen is patchy with clumps of ionized material distributed over the image plane. This will then correspond to the phenomenon of anomalous scattering with a significant departure from a ν^{-2} scaling but always with a weaker dependence on ν (Cordes & Lazio 2001). Depending upon the distribution of ionized clumps, the image flux-density can either amplify or attenuate.

8 Summary and conclusions

B0218+357 is a double-imaged gravitational lens (GL) with the smallest known image angular separation (334 mas) amongst the galactic-scale GLs. Besides the two compact images with flat-spectra, A and B, it has a steep-spectrum Einstein ring of a similar diameter. The properties of the lens match a low-mass and gas-rich spiral galaxy, which based on a high differential Faraday rotation between the images (900 rad m^{-2}) is assumed to have an abundance of ionized matter. The nature of the lensed object is concordant with a blazar-type radio-source, which is variable in its radio emission.

This work focuses on the image flux ratio anomaly seen in B0218+357. Three possible scenarios have been investigated that can lead the observed image flux-densities differing from those predicted by the model, which assumes the 15 GHz image flux-density ratio of ~ 4.0 to be the true ratio. These scenarios were tested based on multi-frequency (1.65 GHz, 2.25 GHz, 4.96 GHz, 8.40 GHz, 15.35 GHz) and phase-reference VLBI observations of B0218+357.

1. Gradient in Relative Image-Magnification (RIM) and frequency-dependent source structure

The primary task of the project was to investigate whether frequency-dependent lensed image centroid-positions, combined with a magnification gradient across the image plane, could give rise to the frequency dependence of the RIM. Unambiguous registration of the structures of the radio images at different frequencies was made using "inverse" phase-referencing. The centroid positions in the brightness distribution of the images were established for all five frequencies. The shift in the centroid in image A, which is significant ($\gtrsim$ 5 mas) only at 1.65 GHz (the lowest observed frequency), is in a direction along which the RIM is predicted to be constant. In image B no significant frequency-dependent shift was detected in the position of the centroid. Thus, it can be concluded that the changing magnification gradient across the images is not the main cause of the anomalous variation of image flux-density ratio with frequency (Mittal et al. 2006). This scenario has been the least of the concerns for other lens systems. This is because of diminutive scale of the system which implies strong magnification gradients in the image plane.

At frequencies $\geq$ 8.4 GHz, both the images are resolved into further subcomponents $\rightarrow$ 1 and 2, identified with the core-jet morphology of the background radio-source. At 1.65 GHz, a distinct secondary maximum in image A has been detected, not seen before, separated by $\sim$ 12 mas from the superposition of A1 and A2. The origin of this newly-identified feature (A3) is of great interest and it was investigated how this can be part of the background source. On applying the SIEP model derived from LensClean, it is deduced that in image B it should be $\sim$ 3 mas from B1. However, the resolution at this frequency is not enough ($\sim$ 7 mas) to resolve this separation. Therefore, it cannot be distinguished whether A3 is a distinct feature in the background source imaged in A by the smooth macro-potential of the lens, or whether it is caused by some other mechanism. The shift in the centroid position of image A at 1.6 GHz can be attributed to the existence of A3. The details of the phase-referencing analysis

and the accompanying results are described in chapter 4.

In the foregoing analysis, it was assumed that the RIM at the centroid positions derived from the model gives a good measure of the expected image flux-density ratio of an extended object. However, for complicated source structures involving steep magnification gradients in the image plane, the issue needs further attention. A more detailed calculation of the relative image-magnifications has been given in chapter 5 using the SIEP model derived from the LensClean algorithm (Wucknitz 2004; Wucknitz et al. 2004). To provide better fitting of some of the observed data to the modeled data, the model was extended to one with a non-isothermal profile. Although the best-fitting model deviates only ~ 4 % from isothermality, the discrepancy is reduced from 5 σ to within 1 σ. But the overall predictions for the two kinds of models are nearly the same. The result of this analysis showed that the RIM estimated from applying the 1.65 GHz image-A centroid position to the model is different by ~ 10 % from when the entire structure of image A is applied. The change corresponds to an increase in the value of RIM at 1.65 GHz which, although compatible with values in the region around the newly identified component A3, is contrary to the observed trend of decreasing image flux ratios observed at lower frequencies.

2. Dark matter clumps: substructure

The macro-model, which produces steep gradients in the relative image-magnifications, does not produce any strong variations in the image flux ratio on interaction with the frequency-dependent source structure. Can structures of intermediate-mass, which are capable of producing even stronger local-gradients on the scale of milliarcseconds, explain away the anomaly? This is the subject of discussion in chapter 6.

The most valuable result in the course of analysing the effects of small-scale structure (milli-lensing) on properties of lensed images, which has emerged from previous studies is the dependence of the effect on the image parity and magnification. Statistical analysis of substructure lensing predicts the positive-parity and negative-parity images to be affected differently. In particular, the fluxes of negative-parity images are, on average, predicted to be perturbed in the direction of demagnification (Keeton 2003; Schechter & Wambsganss 2002). The second result, which is important for the investigation of the B0218+357 flux ratio anomaly, concerns the relative sizes and positions of the source and the substructure. It has been shown by Dobler & Keeton (2005) that the normalized magnification of a lensed macro-image in the proximity of a subclump, whose Einstein radius is much larger than the source-size, can be significantly different from the unperturbed value of unity. For a positive-parity image, it is more than unity for most source positions, whereas for a negative-parity image it is the opposite. As the source size increases there are no significant changes in the combined magnification (due to the macro-model plus the subclump) unless the source crosses the substructure-caustic. For source sizes much bigger than the Einstein radius, the normalized magnification reverts to unity (the net magnification is the same as that predicted by the macro-model in the absence of any substructure). Given the frequency-trend of the B0218+357 image flux-densities, it is difficult to reconcile the above results to reproduce the observed image flux-density ratios unless it is assumed that the ratio observed at the lower end of the frequency spectrum is the unperturbed relative image-magnification. Preliminary investigations carried out by Wucknitz et al. (2004) rule out this possibility since the LensClean residuals increase dramatically as the image magnifications predicted by the SIEP macro-model are changed by more than 5 %. Further, if substructure was interfering

only at high frequencies, the effects should have been visible in the 8.4 GHz global VLBI maps (Biggs et al. 2003) and 8.4 GHz and 15 GHz maps of the images from these observations. But this is not the case. The subcomponents look very alike at high frequencies. Thus, there are no strong arguments in favor of substructure as the main cause of the flux ratio anomaly in B0218+357. Admittedly, this conclusion from the above chain of arguments is rather speculative. A more systematic analysis requires either simulations of a CDM galaxy with a pre-distribution of subhalos or more precise information about the positions and masses of subhalos.

3. Propagation effects: Free-free absorption and scattering

Both these ISM effects have an inverse-frequency-squared dependence. In free-free absorption it is the optical depth that scales as $\nu^{-2.1}$, while in scattering it is the effective size of the scatter-broadened image that scales as $\nu^{-2.2}$. These effects are investigated in chapter 7, where it is assumed that these mechanisms occur, if at all, within the turbulent ionized medium of the lens galaxy and that image B is unaffected. The sharp downturn in the spectrum of image A at 1.6 GHz (not visible in image B) and the small shift in the 1.6 GHz centroid position in A are further results from these observations. These results have no obvious explanation in terms of the expected magnification gradients across the images and, therefore, lend support to the speculation that image A has been perturbed by electromagnetic effects.

There is a substantial body of evidence which indicates that the ISM in front of image A is rich in hot gas and optically active. Assuming that there is an H II region in front of image A, there is an excellent agreement between the predicted Bremsstrahlung absorption curve and the observed spectrum of image A. The resulting emission measure of the H II region, although high, is comparable to values measured for ionized components in galactic and extragalactic interstellar media. The plausible ranges of the electron density and the size of the H II region are such that the possibility of a complete coverage of image A by the ionized region is also included. It is believed that this is the first time that there has been offered a plausible explanation for the image flux ratio anomaly seen in B0218+357. This result has been achieved solely on the grounds of multi-frequency radio continuum observations presented in this work. The hypothesis receives support from radio and optical observations of molecular and atomic absorption lines which indicate the presence of an exotic interstellar medium in the lens galaxy, especially in front of image A. In order to prove that the effects of free-free absorption are compatible with the observed image flux-density ratio in B0218+357, no astrophysical process that was not known from before needed fabrication.

The scattering hypothesis, assuming that the scattering screen has statistically homogenous properties, is not very convincing in the context of discrepant image A flux-densities. From the observations, both the images show an increase in size with wavelength with a similar scaling, $\nu^{-1.4}$ and $\nu^{-1.2}$ for image A and B, respectively. In fact, the intrinsic sizes of synchrotron self-absorbed sources are expected to scale approximately as ν^{-1}, obviating the need for invoking any scattering mechanism. This is in contradiction with the conclusions of Biggs et al. (2003) who discerned bigger sizes for image A subcomponents relative to those of image B and imputed the disparity between the component sizes to scatter-broadening. The results from the observations presented in this work, which were made at five different frequencies, are much more robust since the frequency-dependence of the scatter-broadened regions in both the images can be easily verified. This was not possible with the data acquired by Biggs et al. (2003) since they had only single-frequency observations of this system. Adopting a

more conservative approach, and imposing that the component-size measured in image A at 1.65 GHz is entirely due to scattering, the resulting scattering measure, 2.12 kpc $m^{-20/3}$, is consistent with the values measured for lines of sight through the Milky Way Galaxy. Once again, this is contrary to the result declared by Biggs et al. (2003) who obtained a value of 150 kpc $m^{-20/3}$. Therefore, scattering as an alternative explanation for the anomalous image flux-density ratios can be discarded unless a fragmented scattering screen with clumps of ionized material distributed over image A is envisaged, which then can reproduce any desired result.

Future work on B0218+357

For a detailed investigation of propagation effects (scattering or free-free absorption) and of mass substructure in the lens galaxy, I (w/ Wucknitz, Garrett, Porcas, Koopmans & Biggs) recently observed this system (Nov. 2005) with the EVN (JB1, Wb at 90 cm) and the VLBA (50 cm and 90 cm). This will be the first VLBI measurement of the Einstein ring in B0218+357 yielding unprecedented resolution and will allow us to study the effects not only for the two lines of sights to A and B but over extended parts of the lensing galaxy where the ring emission is much stronger. At the other extreme of the radio frequency spectrum, I (w/ Porcas, Browne & Biggs) made Global 3 mm VLBI observations of B0218+357 (Oct. 2005), with a factor of two higher resolution and frequency than any previous observation of this system. If there is sufficient departure from linearity in the structure in the vicinity of the subcomponents 1 and 2, the relative image magnification matrix can be unambiguously determined for comparisons with the above mentioned SIEP lens model. This has proved difficult using cm-wavelength observations due to their limited resolution and the possibility that propagation effects in the lens galaxy further distort the lensed images.

A Cosmological tools

The foundations of the phenomenon of gravitational lensing are based on Einstein's theory of general relativity. In the following, the basic equations that describe a given cosmological model and the observables that can be derived from them are mentioned.

A.1 Einstein's field equations

Einstein's field equations express the influence of matter and field energy on the curvature of spacetime:

$$\left(\begin{array}{c} \text{Tensor representing the} \\ \text{geometry of space-time} \end{array} = \begin{array}{c} \text{Tensor representing the matter} \\ \text{and energy content of space} \end{array} \right) \tag{A.1}$$

$$R_{\mu\nu} - \frac{1}{2} g_{\mu\nu} R \;=\; \frac{8\pi G}{c^2} T_{\mu\nu} - \Lambda g_{\mu\nu}\,, \tag{A.2}$$

where the left-hand side of Eq. A.2 is the Einstein tensor, which depends on the Ricci tensor $R_{\mu\nu} = R^{\alpha}{}_{\mu\nu\alpha}$, and the Ricci scalar, $R = R^{\alpha}{}_{\alpha}$, which is a contraction of the Ricci tensor. The Riemann tensor, $R^{\alpha}{}_{\mu\nu\beta}$ depends on the metric tensor, $g_{\mu\nu}$, and describes the curvature of the manifold. A space-time is called flat if its Riemann curvature tensor vanishes. On the right-hand side of the equation, $T_{\mu\nu}$ is the energy-momentum tensor, which contains all forms of energy, such as matter energy, radiant energy etc., except for gravitational energy. Λ is the cosmological constant, interpreted as the vacuum energy. G and c are the gravitational constant and the speed of light, respectively.

The solution of Einstein's field equations can be derived based on the hypothesis of the Cosmological Principle (CP), which states that the universe is spatially homogeneous and isotropic over scales $\gtrsim 100$ Mpc. Without making this assumption, Einstein's field equations would contain a large number of unknowns, presenting difficulties in the determination of the metric. The validity of CP is provided by the isotropic distribution of galaxies on large scales and from the isotropy of the Cosmic Microwave Background Radiation (CMBR). Since Earth does not have any special position in this universe, isotropy about every point leads to homogeneity. On applying CP, the Robertson-Walker line element can be derived,

$$ds^2 \;=\; c^2\, dt^2 - R^2(t) \left(\frac{dr^2}{1 - kr^2} + r^2\, d\theta^2 + r^2\, \sin\theta^2\, d\phi^2 \right), \tag{A.3}$$

where t is the cosmic time-coordinate, and $R(t)$ is a function of time called the 'radius' of the universe, which provides a relation between the coordinate distances of a comoving system, r, θ, and ϕ (the comoving coordinates), and physical distances, d_{prop},

$$d_{\text{prop}} \;=\; R(t) f(r)\,, \tag{A.4}$$

where $f(r)$ is the time-independent comoving angular distance,

$$f(r) = \int_0^r \frac{dr}{\sqrt{1-kr^2}} = \begin{cases} \sin^{-1} r & \text{if k} = +1 \\ r & \text{if k} = 0 \\ \sinh^{-1} r & \text{if k} = -1 \end{cases} . \tag{A.5}$$

Assuming that the energy-momentum tensor, $T_{\mu\nu}$, takes the form of a perfect fluid, i.e. an observer moving with the same velocity as that of the fluid's sees the fluid around him as isotropic, Einstein's field equation are reduced to Friedmann's equations:

$$\dot{R}^2 + kc^2 = \frac{8\pi G}{3}\rho R^2 + \frac{\Lambda R^2}{3}, \tag{A.6}$$

where the total mass density (radiation plus matter), ρ, is a function of time (or the scale factor) only, and the dot represents derivative with respect to time. Combining this with the equation of energy conservation,

$$\frac{d}{dR}(\rho R^3 c^2) = -3\,pR^2, \tag{A.7}$$

the following equation, relating the acceleration of the universe to the energy-density of the universe, can be derived

$$\ddot{R} = -\frac{4\pi G}{3}\left(\frac{3p}{c^2} + \rho\right) R + \frac{\Lambda}{3} R, \tag{A.8}$$

where the pressure, p, like the density is a function of time only.

A.2 Cosmological redshift

In an expanding or contracting universe, the frequency of a photon emitted by a distant source undergoes a shift. If a photon of wavelength $\lambda = \lambda_e$ in the rest frame of the source is emitted at $t = t_e$ and reaches the observer at $t = t_o$, the total time-travel is given by,

$$\int_{t_e}^{t_o} \frac{c\,dt}{R(t)} = f(r) = \text{constant}. \tag{A.9}$$

Hence, the ratio of the time-interval of emission in the observer's frame to the rest-frame of the source is

$$\frac{\delta t_o}{\delta t_e} = \frac{R(t_o)}{R(t_e)}. \tag{A.10}$$

In terms of wavelength of the photon, the above equation translates to

$$\frac{\lambda_o}{\lambda_e} = 1 + z, \tag{A.11}$$

where $z = (\lambda_o - \lambda_e)/\lambda_e$ is known as the redshift of the source. Observations of atomic and molecular transitions of distant sources give information on the dynamics of the universe. In an expanding universe, the wavelength of the emitted photon is shifted towards a longer wavelength, and leads to a *red*shift in the wavelength of the photon. In a contracting universe, the opposite is true and will lead to a *blue*shift.

A.3 Density parameters

Introducing the Hubble constant, also known as the relative expansion rate, $H(t) = \dot{R}(t)/R(t)$, and dividing Eq. A.6 throughout by R^2,

$$1 + \frac{kc^2}{R^2H^2} = \frac{\rho_{\rm m} + \rho_{\rm r}}{\rho_{\rm c}} + \frac{\rho_\Lambda}{\rho_{\rm c}} = \frac{\rho_{\rm T}}{\rho_{\rm c}}$$
$$= \Omega_{\rm m} + \Omega_{\rm r} + \Omega_\Lambda = \Omega_{\rm T} \qquad \text{(A.12)}$$

where $\rho_\Lambda = \Lambda/(8\pi G)$ and

$$\rho_{\rm c} = \frac{3H^2}{8\pi G} \qquad \text{(A.13)}$$

is the critical density. $\Omega_{\rm T}$ is the total density parameter and gets contributions from three ingredients of the universe, matter, radiation and the Cosmological constant. If H_0 represents the present-day value of the Hubble constant, the corresponding present-day value of the critical density is $\rho_{\rm c,0} = 1.879 \times 10^{-29}\ h^2$ gm cm^{-3}, where $H_0 = 100\ h$ km s^{-1} Mpc^{-1} is the generally accepted format in which H_0 is written. Note that both Λ and H^2 have units of s^{-2}. From Eq. A.12, it is seen that $\rho_{\rm T} > \rho_{\rm c}$ for $k > 0$ and corresponds to a closed geometry, and $\rho_{\rm T} < \rho_{\rm c}$ for $k < 0$ and corresponds to an open geometry. If the total density is equal to the critical density ($k = 0$), the universe is said to have a flat geometry.

The current-most cosmological model based on CMB observations[1], 2dF galaxy survey and Lyman-α forest data favours the ΛCDM (Cold Dark Matter) flat-cosmology with $h = 0.71 \pm 0.04$, $\Omega_\Lambda = 0.73 \pm 0.04$, $\Omega_{\rm m} = 0.27 \pm 0.04$ and $\Omega_{\rm b} = 0.044 \pm 0.004$ (Spergel et al. 2003), where $\Omega_{\rm m} = \Omega_{\rm cdm} + \Omega_{\rm b}$, is the sum of the densities of cold dark matter and baryonic matter. This is the model that has been assumed throughout this thesis.

A.4 Distances

For sources which are at distances $\gtrsim$ Gly ($z \gtrsim 0.08$), the term 'distance' starts to becomes ambiguous; the value depends upon the observable based on which it is estimated. The most commonly used distances are the angular diameter distance $D_{\rm A}$ and the luminosity distance, $D_{\rm L}$. They both are related to the comoving angular distance between two objects at redshifts z_1 and z_2, defined as $D_{\rm com}(z_1, z_2) = R_0 f(z_1, z_2)$, where R_0 is the radius of the universe at present. Using Eq. A.9 and the definition of the Hubble constant,

$$D_{\rm com}(z_1, z_2) = \int_{R(z_2)}^{R(z_1)} \frac{cR_0}{R^2 H}\, dR = \frac{c}{H_0} \int_{a(z_2)}^{a(z_1)} da\, [a\Omega_{\rm m} + a^2(1 - \Omega_{\rm m} - \Omega_\Lambda) + a^4\Omega_\Lambda]^{-1/2}\,, \qquad \text{(A.14)}$$

where $a(t) = R(t)/R_0$ is a dimensionless scale factor.

The angular diameter distance is defined as the ratio of the physical size of a distant source at z_2 measured at z_1 to its apparent angular diameter, $d/\delta = R_2 f(z_1, z_2)$, where R_2 is the radius of the universe at the time the photon was emitted in the rest-frame of the source. If $z_1 = 0$, then, from the redshift equation, Eq. A.10, $R_2 = R_0(1 + z)^{-1}$ and

$$D_A = \frac{D_{\rm com}(0, z)}{(1 + z)}\,. \qquad \text{(A.15)}$$

[1] WMAP: Wilkinson Microwave Anisotropy Probe, CBI: Cosmic Background Imager, ACBAR: Arcminute Cosmology Bolometer Array Receiver

Similarly, it can be proven that the luminosity distance of a source defined as $D_{\rm L} = [L/(4\pi l)]^{1/2}$, where L and l are its absolute and apparent luminosities, respectively, is,

$$D_{\rm L} \;=\; (1+z) D_{\rm com}(0,z)\,. \tag{A.16}$$

B Emission mechanisms

Several physical processes contribute to the continuum emission observed in the spectrum of an AGN, which are listed below.

B.1 Thermal emission

A gas that is in complete thermal or local thermal equilibrium (any kinds of pressure gradients may be ignored), obeys **Maxwellian distribution of velocities** given by

$$N(v)\ dv\ \propto\ v^2\ e^{\frac{-mv^2}{2kT}}\ dv. \tag{B.1}$$

The medium is then said to be optically thick ($\tau > 1$) and using the Planck's law for blackbody radiation, we get

$$I_\nu\ =\ \frac{2h\nu^3}{c^2}\ \frac{1}{e^{\frac{h\nu}{kT}}-1}, \tag{B.2}$$

$$\begin{aligned}
\text{where}\quad I_\nu &= \text{specific intensity or the brightness, W m}^{-2}\ \text{Hz}^{-1}\ \text{sr}^{-1}\\
h &= \text{Planck constant, } (=\ 6.63\times\ 10^{-34}\ \text{J sec})\\
\nu &= \text{frequency, Hz}\\
c &= \text{speed of light in vacuum, } (=\ 3\times\ 10^8\ \text{km sec}^{-1})\\
k &= \text{Boltzmann constant, } (=\ 1.38\times\ 10^{-23}\ \text{J K}^{-1})\\
T &= \text{temperature, K.}
\end{aligned} \tag{B.3}$$

The peak intensity shifts to higher frequencies with increase in temperatures. On differentiating Eq. B.1 with respect to frequency, we get **Wien's displacement law**

$$\lambda_m T\ =\ const. \qquad \text{m K.} \tag{B.4}$$

The constant ≈ 0.0051 if the intensity is expressed in terms of unit bandwidth and ≈ 0.0029 if expressed in terms of unit wavelength. In the radio regime, $h\nu \ll kT$ and the Planck's equation reduces to **Rayleigh-Jeans law**

$$I_\nu\ =\ \frac{2\nu^2\ kT}{c^2}. \tag{B.5}$$

The **brightness temperature** of a body is defined accordingly

$$T_\mathrm{B}\ =\ \frac{I_\nu c^2}{2\nu^2\ k}. \tag{B.6}$$

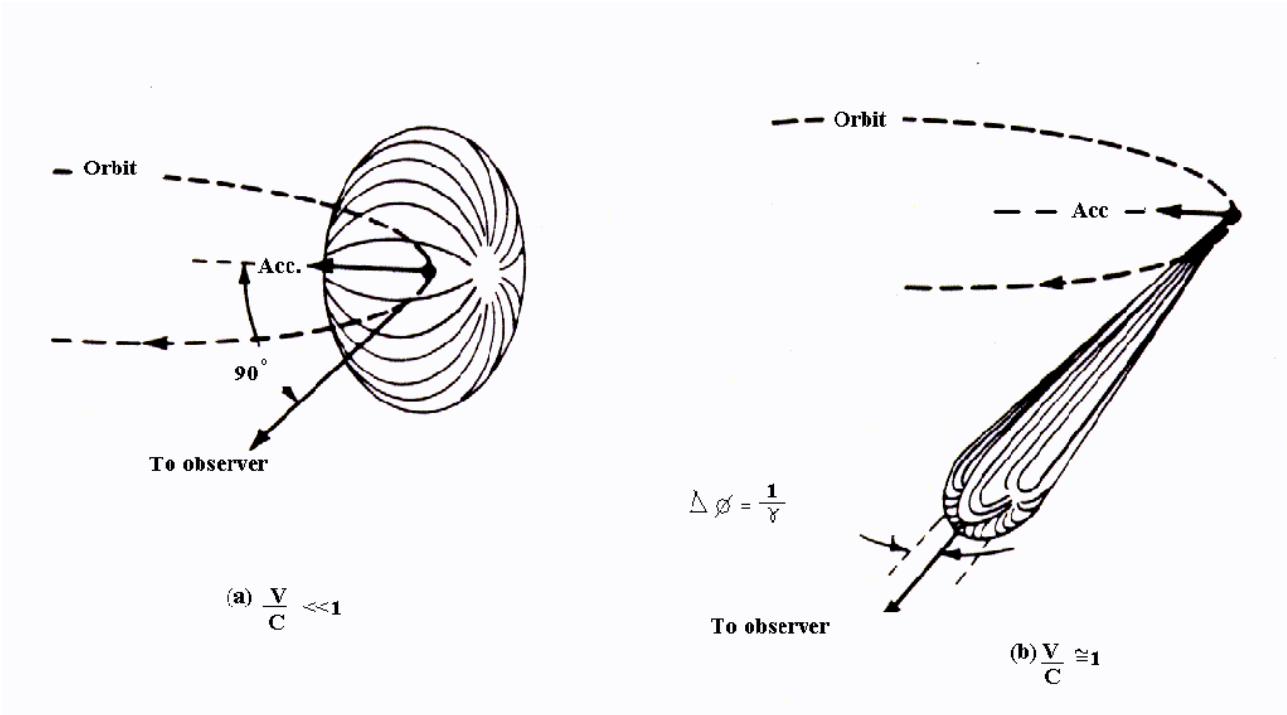

Figure B.1:

B.2 Synchrotron emission

Most non-thermal radio sources are driven by this mechanism. An electron moving in a magnetic field, $\vec{B}$, experiences a force perpendicular to both the direction of its motion, and the magnetic field. It assumes a helical trajectory about $\vec{B}$ with gyration radius, R, and gyration frequency, ν_g, given by

$$R = \frac{mv}{eB} \qquad \nu_g = \frac{eB}{2\pi m}, \tag{B.7}$$

$$\begin{aligned} \text{where} \quad m &= \text{mass of an electron, } (= 9.11 \times 10^{-31} \text{ kg}) \\ v &= \text{speed of the electron, m s}^{-1} \\ e &= \text{charge of an electron } (= -1.60 \times 10^{-19} \text{ C}) \\ B &= \text{magnetic flux density, Wb m}^{-2}. \end{aligned} \tag{B.8}$$

If the electron is relativistic, the above pair of equations are modified such that

$$R^* = \gamma R \qquad \nu_g^* = \frac{\nu_g}{\gamma}, \tag{B.9}$$

where $\gamma = \sqrt{\frac{1}{1-\beta^2}}$ is the Lorentz factor for electrons and $\beta = v/c$.

The radiation pattern of the electron is no longer dipole but instead is beamed at the observer in a cone of semi-opening angle $\sim 1/\gamma$ as shown in Fig. B.1. As a consequence of which, while the gyration frequency is reduced by a factor γ, the frequency of the radiation is increased by

a factor γ^2. Further, since the electron energy $E = \gamma mc^2$, the radiation frequency ν together with Eq. B.7 is

$$\nu \;=\; \gamma^2 \nu_g \;\propto\; BE^2. \tag{B.10}$$

The power radiated by an electron is

$$\frac{dE}{dt} \;\propto\; \gamma^2 U_{\rm mag} \;\propto\; B^2 E^2, \tag{B.11}$$

where $U_{\rm mag} = B^2/(8\pi{\times}10^{-7}$ H m$^{-1})$ is the energy density in the magnetic field. The power radiated by an ensemble of relativistic electrons in a magnetic field is a function of the energy distribution of the electrons, $N(E)dE \propto E^{-p}dE$, and is given by

$$W \;=\; const. \int \frac{dE}{dt}\, N(E)\, dE \;\propto\; \int B^2\, E^2\, E^{-p}\, dE.$$

Using Eqs. B.9 and B.10

$$W \;\propto\; B^2\, E^{3-p} \;\propto\; B^2 \left(\frac{\nu}{B}\right)^{(3-p)/2}$$

$$\frac{dW}{d\nu} \;\propto\; \nu^{(1-p)/2} B^{(1+p)/2}$$

$$F \;\propto\; \nu^{(1-p)/2} \;\propto\; \nu^{-\alpha}, \tag{B.12}$$

where F is the **flux density** and defined as the integral of the intensity Eq. B.1 over the image area ($= \int I_\nu\, d\omega$). Since radio sources have low flux densities, the unit of flux density is Jansky, where 1 Jansky $= 10^{-26}$ W m^{-2} Hz^{-1}. The spectral index of the synchrotron radiation energy spectrum is $\alpha = (p-1)/2$. For the case of well-known cosmic ray electrons that permeate our Galaxy and interact with the magnetic fields, the energy distribution has a power-law index, $p \approx 2.5$, which complies well with the observed flux density of spectral index ~ -0.75. The above treatment is only valid for the part of the spectrum that is optically thin to the synchrotron radiation. For $\nu < \nu_a$, where ν_a is the turnover frequency, the synchrotron photons are **self-absorbed** by the electrons and the plasma becomes optically thick. Then, using Eq. B.5 for an optically thick body, the flux density is

$$F_\nu \;\propto\; I_\nu \;\propto\; \nu^2 kT \;=\; \nu^{5/2}, \tag{B.13}$$

where $kT \equiv$ energy of an electron, which from Eq. B.9 $\propto \nu^{1/2}$. Therefore the sign of the spectral index reverses and α = -2.5. Starting from the definition of flux density and Eq. B.10, if the size and the turnover frequency, ν_a, of the radio source are known, the magnetic field strength can be determined

$$I_\nu \;=\; \frac{F_\nu}{\sigma(=\theta^2)} \;\propto\; \nu^{5/2} B^{-1/2}.$$

$$\theta \;\propto\; {F_\nu}^{1/2} \nu^{-5/4} B^{1/4} \tag{B.14}$$

θ is the one dimensional angular size of the source at frequencies below the turnover frequency.

B.3 Compton and inverse Compton processes

In the Compton process, high-energy photons are scattered by low-energy electrons to lower energies. Thus it provides a cooling mechanism for photons and a heating mechanism for electrons. The inverse Compton process (IC) can be initiated provided there are extremely energetic electrons in the plasma. Then, the electrons can upscatter and boost the photons to frequencies γ^2 times the initial frequency. Therefore radio or optical photons can be upscattered to X-ray or gamma-ray frequencies respectively, by relativistic electrons with $\gamma = 1000$. Inverse Compton process is an important tool in that it keeps the electron temperature from exceeding the inverse Compton limit of 10^{12} K. The synchrotron photons through Compton scattering increase the energy of the electrons which produce more energetic photons through synchrotron radiation. This cycle continues to upscatter the electrons to higher energies, and thus to higher temperatures, until inverse Compton sets in and produces highly energetic photons that are able to escape unlike the low-wavelength synchrotron self-absorbed photons that remain trapped because of the high optical depth of the system.

C Doppler effects

By virtue of an object's motion, in addition to the relativistic term (by virtue of high-velocities with respect to the speed of light), there appears a Doppler term which can be understood as follows. Consider a blob of jet moving with velocity $\vec{v}$, that emits radiation at time t in the rest frame of the observer. After a time-interval dt, the distance covered by the blob is $\vec{v}\,dt$. If the jet makes an angle θ with the line-of-sight, the distance propagated by the blob along the line-of-sight is $(v\cos\theta\,dt)$. Then, the difference between the arrival times of the radiation emitted at times t and $t+dt$ is

$$\Delta t \;=\; dt - \frac{v}{c}\cos\theta\,dt \;=\; dt\,(1-\beta\cos\theta), \tag{C.1}$$

where the second term arises due to the displacement of the blob in time dt in the direction of the observer and $\beta = v/c$. Using the time-dilation relation between dt and dt',

$$\Delta t \;=\; \gamma\,(1-\beta\cos\theta)\,dt'. \tag{C.2}$$

On introducing $D = [\gamma\,(1-\beta\cos\theta)]^{-1}$, known as the Doppler boosting factor, the above equation can be re-written as

$$\Delta t \;=\; \frac{dt'}{D}. \tag{C.3}$$

The $(1-\beta\cos\theta)$ term is a purely geometrical effect due to the motion of an object with respect to the observer, and observed quantities such as time-intervals, the frequency of radiation, and flux densities and velocities of objects are affected by the above described scenario. These cases are discussed in the following sections.

C.1 Superluminal motion

Due to high speeds and small angles subtended to the line-of-sight, the jet components appear to move at speeds more than the speed of light. Such apparent motions are observed by using high-resolution techniques, such as the VLBI which allows motions of the order of $\sim$ mas yr^{-1} to be registered. This anomalous behaviour is termed as superluminal motion and can be explained by considering a geometry similar to that gives rise to the $(1-\beta\cos\theta)$ term. From Eq. C.1, the observed speed of the blob is

$$v_o \;=\; \frac{v\sin\theta\,dt}{(1-\frac{v}{c}\cos\theta)\,dt}$$

$$\beta_o \;=\; \frac{\beta\sin\theta}{1-\beta\cos\theta}\;, \tag{C.4}$$

where $(v\sin\theta\,dt)$ is the displacement in the position of the blob projected in the plane of the sky. Thus, for sufficiently large values of β (> 0.7), superluminal motion in radio sources ($\beta > 1$) can be observed. To account for the cosmological distance associated with

the observed object, Eq. C.1 is multiplied with $(1+z)$, where z is the redshift of the object. If the measured shift in the jet component of a radio source with respect to a stationary core is d mas yr^{-1}, then the apparent observed speed is given by

$$\beta_o \;=\; \frac{66.48}{h_{70}q_0^2}\left(\frac{d}{\text{mas yr}^{-1}}\right)\left(\frac{q_0 z+(q_0-1)(\sqrt{1+2q_0 z}-1)}{1+z}\right). \tag{C.5}$$

Here, q_0 is the deceleration factor [$= -\ddot{R}_0/(H_0^2 R_0)$, where R_0 is defined in Appendix A] and the Hubble constant $H_0 = 71\ h_{70}$ km s^{-1} Mpc^{-1}.

C.2 Doppler boosting

From Eq. C.1, the Doppler effect modification induced in the rest-frame frequency ν' of the radiation is

$$\nu \;=\; D\,\nu'. \tag{C.6}$$

Using the facts that I_ν/ν^3 is a Lorentz invariant and for a spherically symmetric source $F_\nu \propto I_\nu$, a source with a power-law spectrum $F_\nu \propto \nu^{-\alpha}$ will behave as

$$I_\nu \;=\; D^3\, I'_\nu\,, \tag{C.7}$$

$$F_\nu \;=\; D^{3+\alpha}\, F'_\nu. \tag{C.8}$$

If the radiation makes a small angle, θ, with the line-of-sight, is highly relativistic and directed towards the observer, $D > 1$. On the other hand, for radiation directed away from the observer, $D < 1$. Consequently, the flux density is either amplified or deamplified as the case may be. A further modification in Eq. C.8 is introduced when instead of an unresolved point source, a jet feature bigger than the beam size is observed. The change is introduced in the power of D which changes from $3+\alpha$ to $2+\alpha$. Then, the ratio of the flux density of the jet feature pointed towards the observer to that of pointed away is

$$R \;=\; \left(\frac{1+\beta\cos\theta}{1-\beta\cos\theta}\right)^{2+\alpha}. \tag{C.9}$$

C.3 Time variability

Let the time variations observed in the source emission be Δt. Then by causal argument, the source size has an upper limit of $c\Delta t$. Therefore a source at angular distance R will have a solid angle $= (c\Delta t/R)$. From Eq. B.6, the brightness temperature is

$$T \;=\; \frac{c^2 I_\nu}{2\nu^2 K} \;=\; \frac{R^2 F_\nu}{2\nu^2 \Delta t^2 K}. \tag{C.10}$$

where F_ν is the observed flux density and ν the observed frequency. But some sources are observed to vary in their emission over time scales so short that the brightness temperature estimated from Eq. C.10 exceeds the inverse Compton limit of 10^{12} K. This discrepancy was solved by Rees (1966), even before any superluminal motion was observed. He concluded that to have a correct estimation of the brightness temperature, the above equation requires modification using Eqs. C.2, C.6 and C.7. Therefore,

$$T \;=\; \frac{R^2 {F_\nu}' D^3}{2{\nu'}^2 D^2 \Delta({t'}^2/D^2) K}.$$

$$T \;=\; D^3 \frac{R^2 {F'}_{\nu}}{2{\nu'}^2 {\Delta t'}^2 K} \;=\; D^3 T'. \tag{C.11}$$

where T' is the temperature of the source in the rest-frame. Thus for jets that make small angles to the line-of-sight, $D \approx \gamma$ and a Lorentz factor of 10 implies that an observed brightness temperature is overestimated by a factor 1000 in the rest-frame of the observer.

D Image flux and sensitivity

The power received by an antenna from a source is usually specified in terms of the temperature, T_a, of a matched resistor that produces the same amount of power on replacement,

$$P_a \;=\; g^2 k T_a \Delta\nu \,, \tag{D.1}$$

where k is the Boltzmann constant, $\Delta\nu$ is the observing bandwidth and g is the voltage gain; g^2 is the amplification factor. Similarly, the power from the system is

$$P_{sys} \;=\; g^2 k T'_{sys} \Delta\nu \,, \tag{D.2}$$

where T'_{sys} is the off-source system noise temperature. It includes the receiver noise temperature, physical temperature of the transmission line between the antenna and the receiver, antenna spillover, atmospheric emission, the cosmic microwave background (CMB) and galactic radiation. Using the definition of flux-density, the power received by the antenna from a source can also be written as,

$$P_a \;=\; \frac{1}{2} g^2 \eta A S \Delta\nu \;=\; g^2 k K S \Delta\nu \,, \tag{D.3}$$

where S is the source flux-density, A is the area of the antenna, η is the antenna efficiency (the ratio of the effective collecting area to the true geometric area) and a factor of (1/2) appears due to the fact that a single channel receiver responds to only one-half of the total intensity of a randomly polarized wave. $K = (\eta A)/(2k)$, is the antenna sensitivity and on comparing Eqs. D.1 and D.3, it is seen that $K = T_a/S$ with units of K Jy^{-1}.

D.1 System equivalent flux-density

An important parameter that expresses the system performance is the off-source system equivalent flux-density ($SEFD$) defined as,

$$SEFD' \;=\; \frac{T'_{sys}}{K} \,, \tag{D.4}$$

and corresponds to the source flux-density that gives rise to $T_a = T'_{sys}$. The VLBA antennas have a diameter of 25 m each with $SEFD'_{(5\ \mathrm{GHz})} \sim 300$ Jy. The Effelsberg radio telescope has a diameter of 100 m with $SEFD'_{(5\ \mathrm{GHz})} \sim 20$ Jy. By normal convention, the SEFD is a measure of the total temperature of the system,

$$SEFD \;=\; \frac{T_{sys}}{K} \;=\; \frac{T'_{sys} + T_a}{K} \,, \tag{D.5}$$

and corresponds to the source flux-density that doubles the off-source system temperature.

D.2 Signal-to-noise ratio

A quasi-monochromatic electromagnetic wave from a cosmic source gives rise to a voltage signal, $s \propto E(\vec{r},t) = E_0(t)e^{-i(\vec{k}.\vec{r}-wt)}$, which is a covariance-stationary, ergodic stochastic process, i.e. the time averages and ensemble averages are the same. The signal is quasi-monochromatic in that it is a superposition of monochromatic components and has a bandwidth $\Delta\nu$, and comprises short random pulses in time on the order of $\Delta\nu^{-1}$.

The power from an antenna is a sum of the source power [Eq. D.1] and noise power [Eq. D.2] given by

$$\begin{aligned}\langle P\rangle &= g^2k\,(T_a + T'_{sys})\,\Delta\nu \\ &= g^2k\,(KS_T + T'_{sys})\,\Delta\nu \\ &= a\,[\langle s^2\rangle + \langle n^2\rangle] \\ &= a\,\langle (s+n)^2\rangle\,, \end{aligned} \tag{D.6}$$

where s and n are the voltages produced by the source and noise elements, respectively, and do not correlate with each other as a result of which $\langle sn\rangle = 0$. a is a constant which includes the voltage gain and S_T is the total flux-density received by the antenna. The power from a single antenna is the expectation value of the square of the sum of the source and noise voltages. Similarly, the power correlated between an antenna pair $i-j$ is,

$$\begin{aligned}P_{ij} &= \frac{\sqrt{a_i a_j}}{\eta_s}\,\langle (s_i+n_i)(s_j+n_j)\rangle \\ &= \frac{g_i g_j}{\eta_s}\,\sqrt{K_i K_j}\,k\,\Delta\nu\,S_{ij}\,, \end{aligned} \tag{D.7}$$

where S_{ij} is the correlated flux-density, η_s accounts for the electronic and digital losses and the averaged quantities such as $\langle n_i s_j\rangle$, $\langle n_j s_i\rangle$ and $\langle n_i n_j\rangle$ are zero. The signal-to-noise ratio[1] (SNR) of the correlator output is defined in terms of the root-mean-square (rms) sensitivity of a pair of telescopes,

$$\Delta S_{ij} = \frac{1}{\eta_s\sqrt{2\Delta\nu\tau_{corr}}}\sqrt{S_{ij}^2 + S_T^2 + S_T\left(\frac{t'_{sys_i}}{K_i} + \frac{t'_{sys_j}}{K_j}\right) + \frac{t'_{sys_i}t'_{sys_j}}{K_i}K_j}\,, \tag{D.8}$$

where τ_{corr} is the correlator integration time. In the limit of a weak source, which is applicable most of the times, the rms fluctuations on a baseline formed by antennas with the same $SEFD$ is,

$$\Delta S_{ij} = \frac{1}{\eta_s}\frac{SEFD}{\sqrt{2\Delta\nu\tau_{corr}}}\,. \tag{D.9}$$

D.3 Map sensitivity

To derive the image sensitivity or noise in a map, Eq. 3.23 is reproduced in its discrete form,

$$I(x,y) = C\sum_{k=1}^{2M} R_k T_k D_k V_k\, e^{-2\pi i(u_k x + v_k y)}\,, \tag{D.10}$$

[1] For a detailed derivation, see Thompson et al. (2001); Taylor et al. (1999)

where C is a normalization constant, R_k reflects the SNR of the data point, T_k and D_k are, as defined in Sect. 3.5, the tapering function and the density weighting function, respectively. Therefore, the variance in the map is the sum of the variances associated with each data point. If the tapering function $T_k = 1$, natural weighting scheme $D_k = 1$ is used, all data points are assumed to have the same SNR, $R_k = \Delta S^{-2}$, and the normalization constant is set to $C = 1/(2\sum_{k=1}^{M} R_k)$, the noise in the map calculated at the centre pixel is,

$$\begin{aligned} \Delta I &= \frac{\Delta S}{\sqrt{M}}\,, \\ &= \frac{1}{\eta_s}\frac{SEFD}{\sqrt{N(N-1)\Delta\nu\, t_{int}}}, \end{aligned} \tag{D.11}$$

where N is the number of antennas, t_{int} is the total integration time used to make the map, and the M is the total number of visibilities equal to the product of the number of baselines and the number of time-integrated correlator outputs, $M = [N(N-1)/2] \times [t_{int}/\tau_{corr}]$.

E Atmospheric propagation effects

The atmospheric effects on radio waves transmitted from the source can be grouped into two categories : those due to the neutral atmosphere (tropospheric) and those due the ionized layer of upper atmosphere (ionospheric). The effects discussed below are mostly focused on refraction of the incoming rays and, consequently, the geometrical path-delay that is introduced for all the antennas (scattering and absorption effects are not considered here). Even though, this excess path-length is not a physical quantity, it affects the visibilities phases in a way similar to an actual additional path length in front of only one of the antennas of a baseline.

E.1 Troposphere

Given a medium of varying refractive index n (not considering the imaginary term of the refractive index signifying absorption), the additional time taken for a ray to traverse through it in comparison with in vacuum is

$$\Delta T \;=\; \frac{1}{c}\int (n-1)\,dz\,, \tag{E.1}$$

and correspondingly, the excess geometrical path-length is

$$\Delta L \;=\; \int (n-1)\,dz\,. \tag{E.2}$$

The refractivity is typically described in parts per million as $N = 10^6(n-1)$. The phase-velocity of the radio signal is c/n.

Troposphere[1] is non-dispersive to radiation and its refractivity in moist air is given by (Thompson et al. 2001)

$$N \;=\; 77.6\,\frac{p_{\rm D}}{T} + 64.8\,\frac{p_{\rm V}}{T} + 3.776\times 10^5\,\frac{p_{\rm V}}{T^2}\,, \tag{E.3}$$

where T is the temperature (in Kelvins), p is the partial pressure (in millibars), and the subscripts D and V stand for dry and water vapour contributions to neutral atmosphere. Thus, the ray suffers a refractive displacement given by

$$\Delta z \;=\; (n-1)\tan z_0 - b\tan z_0^3\,, \tag{E.4}$$

where z_0 is the zenith angle of the received ray, $\Delta z = z - z_0$ is the angle of refraction, z is the zenith angle for vacuum and b is a constant. For dry atmosphere, $(n-1) \sim 56$ arcsec and $b \sim 0.07$ arcsec amounting to a refraction angle of $\sim 0.46\,^\circ$ at the horizon. If L_0 is the excess

[1] It is the region of the atmosphere extending from the surface of the earth up to a vertical distance of 10 to 11 km

path length in the zenith direction, then assuming the excess path in other directions to be $L_0 \sec z$, which is accurate for small zenith angles, the difference in Δz at different antennas is manifested as a differential path-delay given by

$$\Delta L \;=\; L_0\, \Delta z\, \frac{\sin z}{\cos z^2}\,. \tag{E.5}$$

For VLBI cases, $\Delta L = L_1 \sec z_1 - L_2 \sec z_2$, where $L_1 \sec z_1$ and $L_1 \sec z_2$ are the excess path lengths at the zeniths z_1 and z_2 of the two antennas, respectively. If the three dimensional temperature and water vapour pressure distributions are known, z_0 and ΔL can be precisely estimated. The excess path length, ΔL, can be translated into an excess phase that scales as ν.

The main cause of worry in the radio regime is water vapour since its refractivity at radio wavelengths is 20 times higher than at optical wavelengths. An even more important factor is the inhomogeneity in the water vapour distribution giving rise to phase fluctuations that limit the sensitivity of an interferometer as well as the radio 'seeing'.

E.2 Ionosphere

Ionosphere is a region of plasma that extends from 100 km to 1000 km above the Earth's surface and constitutes of electrons which are dislodged by ultraviolet and higher frequency X-ray photons coming mostly from the sun. The electron distribution is a strongly varying function of latitude, longitude, the time of the day and year, and sunspot cycle. The electron density can vary up to about two or more orders of magnitude at a nominal height of 200 km depending on whether it is day or night.

The refractive index of a ray of radiation of frequency ν passing through an ionized medium, with no magnetic fields, is

$$n \;=\; \sqrt{1 - \frac{\nu_{\rm p}^2}{\nu^2}}\,, \tag{E.6}$$

where $\nu_{\rm p} \propto \sqrt{N_{\rm e}}$ is the plasma frequency of the ionosphere ($\simeq 12$ MHz) and is proportional to the electron density, $N_{\rm e}$ (in m^{-3}). Frequencies that are below the plasma frequency, $\nu < \nu_{\rm p}$, are completely reflected off the ionosphere whereas those above it, $\nu > \nu_{\rm p}$, have a phase-velocity, c/n, higher than the speed of light. In presence of magnetic fields, the refractive index is

$$n \;=\; 1 - \frac{1}{2}\,\frac{\nu_{\rm p}^2}{\nu^2} \pm \frac{1}{2}\,\frac{\nu_{\rm p}^2 \nu_{\rm B}}{\nu^3}\cos\theta\,, \tag{E.7}$$

where $\nu_{\rm B}$ is the gyro-frequency [see Eq. B.7], and θ is the direction between the magnetic field and the direction of propagation.

The angle of bending due to the ionosphere layers is non-zero owing to spherical morphology of the layers, it is zero for a plane-parallel layered morphology (just like a ray of light propagating through a rectangular slab of glass emerges out displaced from the point of incidence but parallel to the direction of the incident ray). The angle of bending with respect to the zenith, z_i, is required to be known to calculate the excess path length suffered by the ray at a height, h,

$$\Delta L \propto -\frac{\sec z_i}{\nu^2}\int_0^\infty N_{\rm e}(h)\, dh\,, \tag{E.8}$$

where the negative delay in reality indicates an advancement of the phase. The integral of N_e over height is known as the total electron content (TEC) or the electron density. The phase change, therefore, scales as ν^{-1} and the phase-delay (the rate of change of phase with frequency) scales as ν^{-2}.

Bibliography

Adgie, R. L. 1974, AJ, 79, 846 17

Adler, D. S., Lo, K. Y., Wright, M. C. H., et al. 1992, ApJ, 392, 497 90

Adler, R., Bazin, M., & Schiffer, M. 1965, Introduction to general relativity (International Series in pure and applied physics, New York: McGraw-Hill, 1965) 5

Bade, N., Siebert, J., & et al., L. 1997, A&A, 317, L13 83

Barkana, R. 1997, ApJ, 489, 21 35

Biggs, A. 2005, in ASP Conf. Ser. 340: Future Directions in High Resolution Astronomy, 433 35

Biggs, A. D., Browne, I. W. A., Helbig, P., et al. 1999, MNRAS, 304, 349 17, 26, 27, 28, 30, 31

Biggs, A. D., Browne, I. W. A., Muxlow, T. W. B., & Wilkinson, P. N. 2001, MNRAS, 322, 821 33

Biggs, A. D., Wucknitz, O., Porcas, R. W., et al. 2003, MNRAS, 338, 599 23, 24, 31, 65, 73, 75, 97, 101, 103, 107, 108

Blandford, R. D. & Kochanek, C. S. 1987, ApJ, 321, 658 11

Blandford, R. D. & Konigl, A. 1979, Relativistic jets as compact radio sources 21

Brown, R. L. 1987, in Spectroscopy of Astrophysical Plasmas, 35–58 91

Browne, I. W. A., Patnaik, A. R., Walsh, D., & Wilkinson, P. N. 1993, MNRAS, 263, 32 18, 19, 20

Browne, I. W. A., Wilkinson, P. N., Jackson, N. J. F., et al. 2003, MNRAS, 341, 13 35

Browne, I. W. A., Wilkinson, P. N., Patnaik, A. R., & Wrobel, J. M. 1998, MNRAS, 293, 257 18

Bullock, J. S., Kravtsov, A. V., & Weinberg, D. H. 2000, ApJ, 539, 517 84

Campbell, R. M., Lehar, J., Corey, B. E., Shapiro, I. I., & Falco, E. E. 1995, AJ, 110, 2566 35

Carilli, C. L., Menten, K. M., Stocke, J. T., et al. 2000, Physical Review Letters, 85, 5511 90

Carilli, C. L., Rupen, M. P., & Yanny, B. 1993, ApJ, 412, L59 20

Chiba, M. 2002, ApJ, 565, 17 83, 84, 85, 87

Chwolson, O. 1924, Astronomische Nachrichten, 221, 329 3

Clark, B. G. 1980, A&A, 89, 377 49

Cohen, A. S., Hewitt, J. N., Moore, C. B., & Haarsma, D. B. 2000, ApJ, 545, 578 17, 29

Cohen, J. G. 1996, in ASP Conf. Ser. 88: Clusters, Lensing, and the Future of the Universe, 68 20

Cohen, J. G., Lawrence, C. R., & Blandford, R. D. 2003, ApJ, 583, 67 19, 20

Cohen, M. H., Jauncey, D. L., Kellermann, K. I., & Clark, B. G. 1968, Science, 162, 88 36

Colín, P., Avila-Reese, V., & Valenzuela, O. 2000, ApJ, 542, 622 84

Condon, J. J. 1997, PASP, 109, 166 64

Corbett, E. A., Browne, I. W. A., & Wilkinson, P. N. 1996, in IAU Symp. 173: Astrophysical Applications of Gravitational Lensing, 37 17, 22, 28

Cordes, J. M. & Lazio, T. J. W. 2001, ApJ, 549, 997 97, 104

Dalal, N. & Kochanek, C. S. 2002, ApJ, 572, 25 84, 85, 88

Dame, T. M., Elmegreen, B. G., Cohen, R. S., & Thaddeus, P. 1986, ApJ, 305, 892 90

Dobler, G. & Keeton, C. R. 2005, MNRAS, 1122 86, 87, 106

Dyson, F. W., Eddington, A. S., & Davidson, C. R. 1920, Mem. R. Astron. Soc., 62, 91 3

Eddington, A. S. 1920, Space, time and gravitation. an outline of the general relativity theory (Cambridge Science Classics, Cambridge: University Press, 1920) 3

Einstein, A. 1936, Science, 84, 506 3

Ellithorpe, J. D., Kochanek, C. S., & Hewitt, J. N. 1996, ApJ, 464, 556 50

Evans, N. W. & Wilkinson, M. I. 1998, MNRAS, 296, 800 11

Faber, S. M., Tremaine, S., Ajhar, E. A., et al. 1997, AJ, 114, 1771 11, 76

Falco, E. E., Impey, C. D., Kochanek, C. S., et al. 1999, ApJ, 523, 617 29, 89, 90

Fassnacht, C. D., Blandford, R. D., Cohen, J. G., et al. 1999, AJ, 117, 658 83

Felli, M. & Spencer, R. E., eds. 1989, Very long baseline interferometry: Techniques and applications 36

Friberg, P. & Hjalmarson, Å. 1990, Molecular clouds in the Milky Way (Molecular Astrophysics), 3 90

Goodman, J. 1997, New Astronomy, 2, 449 97

Grundahl, F. & Hjorth, J. 1995, MNRAS, 275, L67 24

Guirado, J. C. et al. 1999, A&A, 346, 392 97

Heiles, C., Chu, Y.-H., & Troland, T. H. 1981, ApJ, 247, L77 94

Henkel, C., Jethava, N., Kraus, A., et al. 2005, A&A, 440, 893 90, 102

Hjorth, L. 1997, in Golden lenses, Hubbles's Constant and Galaxies at high Redshift Workshop. Jodrell Bank Observatory, Cheshire, ed. P. Helbig & N. Jackson 26, 27

Högbom, J. A. 1974, A&AS, 15, 417 47

Huchra, J., Gorenstein, M., Kent, S., et al. 1985, AJ, 90, 691 83

Hummel, C. A., Schalinski, C. J., Krichbaum, T. P., et al. 1992, A&A, 257, 489 21

Jackson, N., de Bruyn, A. G., Myers, S., et al. 1995, MNRAS, 274, L25 83

Jackson, N., Nair, S., Browne, I. W. A., et al. 1998, MNRAS, 296, 483 83

Jackson, N., Xanthopoulos, E., & Browne, I. W. A. 2000, MNRAS, 311, 389 24, 26, 27, 28, 90

Jennison, R. C. 1958, MNRAS, 118, 276 42

Johnson, K. H. 1974, AJ, 79, 1006 17

Jones, D. L. et al. 1996, ApJ, 470, L23 97

Kassiola, A. & Kovner, I. 1993, ApJ, 417, 450 14

Keeton, C. R. 2003, ApJ, 584, 664 85, 106

Keeton, C. R. & Kochanek, C. S. 1997, ApJ, 487, 42 35

Kellermann, K. I., Vermeulen, R. C., Zensus, J. A., & Cohen, M. H. 1998, AJ, 115, 1295 20

Kemball, A. J., Patnaik, A. R., & Porcas, R. W. 2001, ApJ, 562, 649 31, 65

Kembhavi, A. K. & Narlikar, J. V. 1999, Quasars and active galactic nuclei : an introduction (Quasars and active galactic nuclei : an introduction /Ajit K. Kembhavi, Jayant V. Narlikar. Cambridge, U.K. : Cambridge University Press, c1999. ISBN 0521474779.) 20, 91

King, L. J., Browne, I. W. A., Muxlow, T. W. B., et al. 1997, MNRAS, 289, 450 18

Klypin, A., Kravtsov, A. V., Valenzuela, O., & Prada, F. 1999, ApJ, 522, 82 84

Kochanek, C. S. 2004, ApJ, 605, 58 85

Kochanek, C. S. & Dalal, N. 2004, ApJ, 610, 69 84, 85

Kochanek, C. S. & Narayan, R. 1992, ApJ, 401, 461 49

Kochanek, C. S., Schneider, P., & Wambsganss, J. 2004, in A review of strong gravitational lensing and its astrophysical uses. (Part 2 of Gravitational Lensing: Strong, Weak and Micro, Proceedings of the 33rd Saas-Fee Advanced Course, G. Meylan, P. Jetzer and P. North, eds. Springer-Verlag: Berlin) 9, 11, 12, 29

Koopmans, L. V. E., Biggs, A., Blandford, R. D., et al. 2003, ApJ, 595, 712 84

Koopmans, L. V. E., de Bruyn, A. G., Xanthopoulos, E., & Fassnacht, C. D. 2000, A&A, 356, 391 35

Kormann, R., Schneider, P., & Bartelmann, M. 1994, A&A, 284, 285 14

Kovner, I. 1989, ApJ, 337, 621 14

Lawrence, C. R. 1996, in IAU Symp. 173: Astrophysical Applications of Gravitational Lensing, 299 20

Lawrence, C. R., Schneider, D. P., Schmidet, M., et al. 1984, Science, 223, 46 40

Lehár, J., Falco, E. E., Kochanek, C. S., et al. 2000, ApJ, 536, 584 24, 26, 27, 90

Lo, K. Y., Ball, R., Masson, C. R., et al. 1987, ApJ, 317, L63 102

Lobanov, A. P. 1998, A&A, 330, 79 21

Magain, P., Surdej, J., Swings, J.-P., Borgeest, U., & Kayser, R. 1988, Nature, 334, 325 83

Mao, S., Jing, Y., Ostriker, J. P., & Weller, J. 2004, ApJ, 604, L5 84

Mao, S. & Schneider, P. 1998, MNRAS, 295, 587 83, 84

Marcaide, J. M., Shapiro, I. I., Corey, B. E., et al. 1985, A&A, 142, 71 21

Marlow, D. R., Myers, S. T., Rusin, D., et al. 1999a, AJ, 118, 654 83

Marlow, D. R. et al. 1999b, MNRAS, 305, 15 35, 97

Marscher, A. P. 1977, ApJ, 216, 244 103

Menten, K. M. & Reid, M. J. 1996, ApJ, 465, L99 90

Metcalf, R. B. 2002, ApJ, 580, 696 35

Mittal, R., Porcas, R., Wucknitz, O., Biggs, A., & Browne, I. 2006, A&A, 447, 515 2, 105

Moore, B., Ghigna, S., Governato, F., et al. 1999, ApJ, 524, L19 84

Mould, J. R., Huchra, J. P., Freedman, W. L., et al. 2000, ApJ, 529, 786 17

Myers, S. T., Fassnacht, C. D., Djorgovski, S. G., et al. 1995, ApJ, 447, L5+ 83

Myers, S. T., Jackson, N. J., Browne, I. W. A., et al. 2003, MNRAS, 341, 1 35

Myers, S. T., Rusin, D., Fassnacht, C. D., et al. 1999, AJ, 117, 2565 83

Narasimha, D. 2004, Bulletin of the Astronomical Society of India, 32, 257 35

Narayan, R. 1992, Phil. Trans. Roy. Soc., 341, 151 97

Narayan, R. & Bartelmann, M. 1999, in Formation of Structure in the Universe, 360 10

Navarro, J. F., Frenk, C. S., & White, S. D. M. 1996, ApJ, 462, 563 35

O'Dea, C. P., Baum, S. A., Stanghellini, C., et al. 1992, AJ, 104, 1320 18, 21, 31, 32, 94

Patnaik, A. R., Browne, I. W. A., King, L. J., et al. 1992a, LNP Vol. 406: Gravitational Lenses, 406, 140 18, 94

—. 1993, MNRAS, 261, 435 18, 21, 22, 27, 28, 31, 32

Patnaik, A. R., Browne, I. W. A., Walsh, D., Chaffee, F. H., & Foltz, C. B. 1992b, MNRAS, 259, 1P 83

Patnaik, A. R., Browne, I. W. A., Wilkinson, P. N., & Wrobel, J. M. 1992c, MNRAS, 254, 655 18

Patnaik, A. R. & Porcas, R. W. 1999, in ASP Conf. Ser. 156: Highly Redshifted Radio Lines, 247 31, 33

Patnaik, A. R., Porcas, R. W., & Browne, I. W. A. 1995, MNRAS, 274, L5 23, 24, 31, 64, 65

Pauliny-Toth, I. I. K. & Kellermann, K. I. 1972, AJ, 77, 797 17

Pearson, T. J. & Readhead, A. C. S. 1984, ARA&A, 22, 97 49

Phillips, P. M., Norbury, M. A., & Koopmans, L. V. E. e. a. 2000, MNRAS, 319, L7 83

Porcas, R. W. 2001, in 15th Working Meeting on European VLBI for Geodesy and Astrometry, 201–207 54

Rees, M. J. 1966, Nature, 211, 468 118

Refsdal, S. 1964, MNRAS, 128, 307 4

Reimers, D., Hagen, H.-J., Baade, R., Lopez, S., & Tytler, D. 2002, A&A, 382, L26 83

Rickett, B. J. 1990, ARA&A, 28, 561 97

Robson, I. 1996, Book Review: Active galactic nuclei / Wiley/Praxis, 1996, Vol. 106, 164 20

Roshi, D. A. & Anantharamaiah, K. R. 2001, ApJ, 557, 226 92

Russell, H. N. 1937, Scientific American, 84, 76 3

Rybicki, G. B. & Lightman, A. P. 1979, Radiative processes in astrophysics (New York, Wiley-Interscience, 1979. 393 p.) 96

Ryle, M. 1962, Nature, 194, 517 40

Schechter, P. L. & Wambsganss, J. 2002, ApJ, 580, 685 85, 106

Schmidt, M. 1963, Nature, 197, 1040 4

Schneider, P., Ehlers, J., & Falco, E. E. 1992, Gravitational Lenses (Gravitational Lenses, XIV, 560 pp. 112 figs.. Springer-Verlag Berlin Heidelberg New York. Also Astronomy and Astrophysics Library) 7, 9

Schwab, F. R. 1984, AJ, 89, 1076 49

Shaver, P. A. 1976, A&A, 49, 1 92

Shields, G. A. 1990, ARA&A, 28, 525 103

Solomon, P. M. & Sanders, D. B. 1980, in Giant Molecular Clouds in the Galaxy, 41–73 103

Spangler, S. R. & Cordes, J. M. 1998, ApJ, 505, 766 101

Spangler, S. R., Mutel, R. L., Benson, J. M., & Cordes, J. M. 1986, ApJ, 301, 312 101

Spergel, D. N. & Steinhardt, P. J. 2000, Physical Review Letters, 84, 3760 84

Spergel, D. N., Verde, L., Peiris, H. V., et al. 2003, ApJS, 148, 175 17, 111

Stickel, M. & Kuhr, H. 1993, A&AS, 101, 521 20

Sykes, C. M., Browne, I. W. A., Jackson, N. J., et al. 1998, MNRAS, 301, 310 83

Taylor, G. B., Carilli, C. L., & Perley, R. A., eds. 1999, Synthesis Imaging in Radio Astronomy II 36, 46, 122

Thompson, A. R., Moran, J. M., & Swenson, G. W. 2001, Interferometry and synthesis in radio astronomy (Interferometry and synthesis in radio astronomy by A. Richard Thompson, James M. Moran, and George W. Swenson, Jr. 2nd ed. New York : Wiley, c2001.xxiii, 692 p. : ill. ; 25 cm. "A Wiley-Interscience publication." Includes bibliographical references and indexes. ISBN : 0471254924) 36, 122, 125

Thompson, R. 1999, in ASP Conf. Ser. 180: Synthesis Imaging in Radio Astronomy II, ed. G. B. Taylor, C. L. Carilli, & R. A. Perley, 11 37

Treu, T., Koopmans, L. V. E., Bolton, A. S., Burles, S., & Moustakas, L. A. 2006, ApJ 4

Turner, E. L., Hewitt, J. N., Brody, J. P., et al. 1989, BAAS, 21, 718 83

Twiss, R. Q., Carter, A. W. L., & Little, A. G. 1960, The Observatory, 80, 153 42

Unwin, S. C., Cohen, M. H., Hodges, M. W., Zensus, J. A., & Biretta, J. A. 1989, ApJ, 340, 117 21

Walker, C. & Chatterjee, S. 1999, VLBA Scientific Memo, 23 56

Walker, M. A. 1998, MNRAS, 294, 307 100

Walsh, D., Carswell, R. F., & Weymann, R. J. 1979, Nature, 279, 381 4

Weinberg, S. 1972, Gravitation and cosmology: Principles and applications of the general theory of relativity (New York: Wiley, —c1972) 5

Weymann, R. J., Latham, D., Roger, J., et al. 1980, Nature, 285, 641 83

Wiklind, T. & Combes, F. 1995, A&A, 299, 382 20, 24

Wilkinson, P. N., Browne, I. W. A., Patnaik, A. R., Wrobel, J. M., & Sorathia, B. 1998, MNRAS, 300, 790 18

Winn, J. N., Morgan, N. D., Hewitt, J. N., et al. 2002, AJ, 123, 10 9

Winn, J. N., Rusin, D., & Kochanek, C. S. 2003, ApJ, 587, 80 35

Winn, J. N. et al. 2004, AJ, 128, 2696 97

Wisotzki, L., Christlieb, N., Liu, M. C., et al. 1999, A&A, 348, L41 83

Wisotzki, L., Schechter, P. L., Bradt, H. V., Heinmüller, J., & Reimers, D. 2002, A&A, 395, 17 83

Witt, H. J., Mao, S., & Keeton, C. R. 2000, ApJ, 544, 98 26

Wood, D. O. S. & Churchwell, E. 1989, ApJS, 69, 831 92

Wucknitz, O. 2002, Ph.D. Thesis 48, 74

—. 2004, MNRAS, 349, 1 50, 106

Wucknitz, O., Biggs, A. D., & Browne, I. W. A. 2004, MNRAS, 349, 14 26, 27, 28, 29, 35, 72, 106

York, T., Jackson, N., Browne, I. W. A., Wucknitz, O., & Skelton, J. E. 2005, MNRAS, 357, 124 24, 25, 26, 27, 28, 90

Zensus, J. A. & Porcas, R. W. 1985, High resolution observations of optically weak flat spectrum radio sources (Active galactic nuclei (A86-36901 16-90). Manchester, England and Dover, NH, Manchester University Press, 1985, p. 54-57.), 54–57 18

Zwicky, F. 1937a, Phys. Rev. Lett., 51, 290 4

—. 1937b, Phys. Rev. Lett., 51, 679 4

Remark: The numbers after the references indicate the page numbers where the citation occurs.

Acknowledgments

Firstly, I would like to thank the Max-Planck-Gesellschaft for giving me an opportunity to accomplish my doctoral work in an encouraging and work-conducive environment. The International Max Planck Research School (IMPRS) for Radio and Infrared astronomy at the Universities of Bonn and Cologne supported me financially, without which this work would not have been possible.

I am very grateful to my mentor, Richard Porcas. His expertise on various astronomical fields helped me enhance my scientific skills. I thank him sincerely for taking out as much time for me as I required or rather demanded, without which it would have been extremely difficult for me alone to make any sensible interpretations about the data.

I would also like to thank my secondary advisor, Peter Schneider, for his timely discussions and suggestions. I appreciate contributions from my collaborators Olaf Wucknitz, Andy Biggs and Ian Browne. I thank Olaf especially, for providing scientific overviews at times when they were needed, and showing infinite patience while having (email) discussions with me. The lens model from the LensClean algorithm, which was used throughout this project, was kindly provided by Olaf. Apart from that, the work described in chapter 5 was done in collaboration with him. I also thank him for giving useful comments on various parts of this manuscript. I am grateful to Martin Kilbinger for scientific feedbacks at several occasions and particularly for the timely notification of an insistent error in the analysis. I thank Alan Roy whole-heartedly for allowing me to barge into his office any time I needed scientific advice. His suggestions and comments on the text helped improve both its appearance as well as my writing skills. Discussions with Karl Menten and Christian Henkel were very helpful and encouraging, and I thank them for giving me their time. Efforts by Richard and John McKean are sincerely appreciated in carefully going through this manuscript and improving both the scientific content and presentation. I would also like to express my gratitude to Prof. Peter Schneider, Dr. Walter Huchtmeier, Prof. Norbert Wermes and Dr. Axel Nothnagel for their willingness to participate as members of my PhD. examination board.

There are many people whom I'd like to thank for their support and encouragement both at and outside of work. Enno Middelberg, Walter Alef, Arno Witzel, Anton Zensus, Eduardo Ros, Thomas Krichbaum, Alan Roy, David Graham, Antonios Polatidis, Tigran Arshakian and Andrei Lobanov to name a few from the VLBI group. My officemate, Krisztina, is irreplaceable! We gave each other company while writing our respective theses until the dead of the night. It's been a pleasure knowing and sharing the office with her. I am thankful to the IMPRS coordinators, Frau Lahr-Nilles and Frau Breuer, for taking care of the nitty-gritties of the administrative processes. I am grateful to the cleaning staff for kindly providing me an additional dustbin and relieving themselves from picking up crumpled paper from the floor everyday, and the canteen staff for providing me hot and vegetarian lunches.

These three years of my graduation would not have been half as productive, fun, memorable and successful without the support and love from Martin. Thanks buddy! Wolfgang Kilbinger, Dorothee Kilbinger, Mariam, Cenabi, Airat, Tony, Vlady, Giri, other members of my

family in Germany, I owe three wonderful years to each of you. Mama, papa and di, none of this would have happened without your love and guidance. Ma and pa, I can't thank you enough for having taken care of Caesor all these years while I was away. Caesor (June 4, 1996 – April 9, 2006), you were a wonderful and loving family-member, and the most adorable creation that came into existence. Your unconditional love, amongst all other things, would be missed forever.

Lastly but not the least, I would also like to express my appreciation for the VLBA and Effelsberg operational staff, and the VLBA correlator staff for the their help in obtaining the data. The National Radio Astronomy Observatory is a facility of the National Science Foundation operated under cooperative agreement by Associated Universities, Inc. The Effelsberg radio telescope is operated by the Max-Planck-Institut für Radioastronomie (MPIfR).

Mukul, following your orders, instead of thanking you I will quote these lines from Floyd's "Astronomy Domine" in your name.

"Lime and limpid green a second scene a fight between the blue you once knew
Floating down the sound resounds around the icy waters underground
Jupiter and Saturn
Oberon, Miranda, Titania,
Neptune titan stars can frighten
Blinding signs flat flicka flicka flicka blam pow
Stairway, scale down, dare whose lair
Lime and limpid green, the sound surrounds the icy waters underground
Lime and limpid green, the sound surrounds the icy waters underground".